九州大学学術情報リポジトリ
Kyushu University Institutional Repository

DESIGN AND FABRICATION OF AN ULTRA-THIN ACTUATOR BASED ON MEMS PROCESS FOR SINGLE OPTICAL FIBER SCANNER

孙, 滨

https://doi.org/10.15017/1543933

出版情報：九州大学, 2015, 博士（工学）, 課程博士
バージョン：
権利関係：全文ファイル公表済

DESIGN AND FABRICATION OF AN ULTRA-THIN ACTUATOR BASED ON MEMS PROCESS FOR SINGLE OPTICAL FIBER SCANNER

TABLE OF CONTENT

ABSTRACT.....1

1. INTRODUCTION 5
1.1 Introductions to conventional flexible endoscope..... 5
1.1.1 Optical fiber bundle for medical endoscope..... 6
1.1.2 Image sensor (CCD or CMOS) for medical endoscope 8
1.2 Alternative scanning approaches to medical endoscope 10
1.3 A novel scanning approach to medical endoscope 13
1.3.1 PZT actuator 14
1.3.2 Electromagnetic actuator 15
1.3.3 Micro motor..... 16
1.4 Scanning pattern for single optical fiber endoscope 17
1.5 Calibrating single optical fiber endoscope 18
1.6 Optical modalities 21
1.6.1 Optical tomography coherence (OTC) for endoscope..... 21
1.6.2 Confocal microscopy for endoscope 22
1.7 Research Goal and Tasks..... 24
1.8 Dissertation Overview..... 25
2. ELECTROMAGNETIC-ACTUATED FIBER SCANNER BASED ON 3D LITHOGRAPHY PROCESS 27
2.1 General design of fiber scanner..... 27
2.2 Component design..... 29
2.2.1 Optical fiber with magnet..... 29
2.2.2 The tilted Microcoil..... 31
3. THEROY AND MAGNEIRC ANALYSIS..... 33
3.1 Magnetic field analysis 33
3.2 Magnetization analysis..... 34
3.3 Magnetic force analysis..... 35
3.4 Summary 41
4. OFF-AXIS MAGNETIC FIELD ANALYSIS 43
4.1 Theory analysis 43
4.2 Numerical Analysis 50
4.2.1 Numerical Analysis of one loop 50
4.2.2 Numerical Analysis of two loops 52
4.3 Summary 55
5. MECHANICAL ANALYSIS 57
5.1 Structure with one lumped mass 57
5.2 Structure with two lumped masses..... 64
5.2.1 Theory of two degrees freedom system..... 65
5.2.2 Numerical Analysis of two degrees freedom system 74

5.3 Summary 83
6. FABRICATION PROCESS 85
6.1 Sputtering process 89
6.2 Spray coating process 90
6.3 3D lithography process 95
6.3.1 Introduction to 3D lithography system 95
6.3.2 Mask design and program 100
6.4 Etching process 106
6.5 Electroplating process 108
6.6 Summary 110
7. ELECTROMAGNETIC-ACTUATED FIBER SCANNER BASED ON 3D PRINTING PROCESS 111
7.1 Fundamental structure 112
7.2 Manufacturing method 112
7.3 Manufacturing result 113
7.4 Measurement result 114
7.5 Summary 117
8. CONCLUSIONS AND FUTURE WORK 119
8.1 Conclusions 119
8.2 Future work 120
REFERENCE 123

ABSTRACT

The design, fabrication and measurement of a novel ultra-thin fiber scanner are proposed in this research, the fiber scanner consists of an optical fiber, a soft-magnetic magnet CobaltNickle, two tilted microcoils, a lens and jig. The single optical fiber is actuated by tilted microcoil actuator fabricated on the surface of 1mm polyimide pipe by MEMS process.

In this research, the design of the fiber scanner mainly includes two aspects: electromagnetic-actuation performance and mechanical structure. And the scanning angle and displacement of fiber tip is the criteria for judging the progress of design research. The innovative design of the fiber scanner can be categorized into three parts: (1) development of a soft-magnetic magnet CoNi, which provides Low coercive field strengths, meaning that magnetization direction can be altered by low external magnetic field, realizing scanning under low power; (2) Two degrees of freedom vibration system, adding a lumped mass at fiber tip, which could realize large scanning angle at second-order resonant frequency; (3) development of a novel three-dimensional (3D) lithography system, which offers a low cost and effective way to fabricate tilted microcoil with decreased pitch, further increasing driving force.

At the beginning, the crucial parameters of microcoil such as tilt-angle, pitch, turns have been optimized using ANSOFT Maxwell, the larger magnetic force is obtained at the pitch of 80 μm, tilt-angle of $60^{o}$and turns of 20. Next, external

magnetic field of tilted microcoil has been analyzed with varying coil radius, tilt-angles, pitch and turns respectively, the strongest magnetic field is generated by the smaller coil radius, the larger tilt-angle, and the smaller pitch. Finally, they are decided as tilt-angle for 60°, pitch for 80 μm and coil radius for 0.5 mm according to our fabrication ability.

Like all the structures, this fiber scanner has its resonant frequency and performs a large scanning angle at it. The frequency and mode shapes of this fiber scanner have been simulated. The displacement and scanning angle of fiber tip are obtained with different structures. The largest scanning angle is obtained for 0.28º at first-order vibration. Obviously, the scanning angle is not large enough. So in order to enhance scanning angle, an improved design of fiber scanner has been developed. A larger scanning angle can be obtained for 4.0º at two-degree freedom vibration.

The key fabrication process has been introduced, including sputtering process, 3D lithography process, spraying coating process and mask-less electroplating process. The photoresist pattern of microcoil with tilt-angle of 45º can be patterned with 10±0.2 μm coil width, 78.5±0.5μm coil pitch and 20 turns. And the photoresist pattern microcoil with tilt-angle 60º also can be successfully patterned with 10±0.2μm coil width, 81.5±0.5 μm coil pitch and 20 turns. Cu coil line is formed by mask-less electroplating process .And the Cu coil line grows along Au coil line vertically and expands both sides. Finally, Cu coil line width increases to 40 μm and thickness grows to 15 μm based on 10 μm Au coil line.

An assembled fiber scanner is measured using high speed camera, and fiber tip

displacement has not been obtained due to the flaws of this electroplated sample. Thus, a novel hybrid process is proposed for manufacturing an ultra-thin tiny tilted coil with decreased pitch, large tilt-angle, and good electrical characteristics, providing a large driving force.

A 2.0 mm diameter tiny tilted coil is achieved, and line pitch, tilt-angle, resistance, and turns of it are 75 μm, 60º, 20 Ohm, and 100 respectively. The scanning motion of assembled scanner was measured by high speed camera. At the beginning, the tilted coil was applied with 1V AC driving voltage, 60.5μm and 85.7μm displacement of fiber tip were obtained at first-order vibration during entire magnet inside and half magnet outside location respectively. And displacement was increased with rising driving voltage, and maximum 125.3μm displacement can be achieved at large driving power. Thus, the hybrid process shows a promising application for fabricating this actuator, and this fiber scanner can be used as a probe for micro biomedical endoscope.

1. INTRODUCTION

1.1 Introductions to conventional flexible endoscope

Image acquisition of lesion and damage of internal organs and ducts human body can be commonly classified into two categories (1) Structure-based medical image acquisition, for instance, x-ray computed tomography (CT)[1,2], which is a technique that utilizes x-ray to generate tomographic image of interest area of the scanned tissue and lesion, allowing to inspect inside human body without cutting tissue, on the other hand, magnetic resonance imaging (MRI)[3,4], which is a typically medical imaging system employed in radiology to inspect the anatomy and physiology of body in both health and disease, being used widely in hospital for inspection tissue and lesion. But they both image at low spatiotemporal resolution (millimeters, seconds); and (2) Surface-based medical imaging, medical endoscopic technology, which images at high spatiotemporal resolution (micrometers, milliseconds). Because the medical imaging is captured using endoscopy by visualizing the surface of lesion of internal organs human body directly, illumination system and detection system are both inserted directly into body through a tortuous duct to a region of lesions. Thus, medical endoscopic technologies detecting pathological changes of tissue and guiding intervention are significantly approved by patients and clinician. The accessibility of internal organs is obviously decided by the diameter and flexibility of medical endoscope. For many situations, a miniature diameter and flexible endoscope is necessarily needed for reducing tissue trauma and medication (sedation)

to avoid pain experienced by the subject [5].

Conventional flexible endoscopes are approximately as thick as a human finger and designed for obtaining high quality medical imaging of lesion, being primarily used for inspecting large internal organs such as stomach, small intestine, and duodenum and so on. The endoscope has a flexible shaft, typically with a remote-controlled tip. In a narrower sense, it refers to pure optical-fiber endoscope. Sometimes the term “fiberscope” is also used to distinguish it from video scopes having an integrated micro-camera. They are also offering a larger field of view (FOV) on the surface of lesion region and detecting the tissues in a certain depth, being able to be used for navigating the scope within the body, inspecting tissue, diagnosing disease, and guiding surgical interventions. There are two kinds of conventional endoscopes, optical fiber bundle endoscope and image sensor endoscope.

1.1.1 Optical fiber bundle for medical endoscope

A fiber optic bundle is defined as any fiber optic assembly that contains more than one fiber optic in a single cladding, which is used as a bendable tube for transmitting the light between proximal end and distal ends in the cladding [6] for endoscope applications [7-10]. Each fiber acts as a light pipe, transmitting the light from that part of the image along the fiber. If the arrangement of the fibers in the bundle is kept constant then the transmitted light forms a mosaic image of the light which struck the end of the bundle, as shown in Fig.1-1. One pixel could be obtained

by one optical fiber.

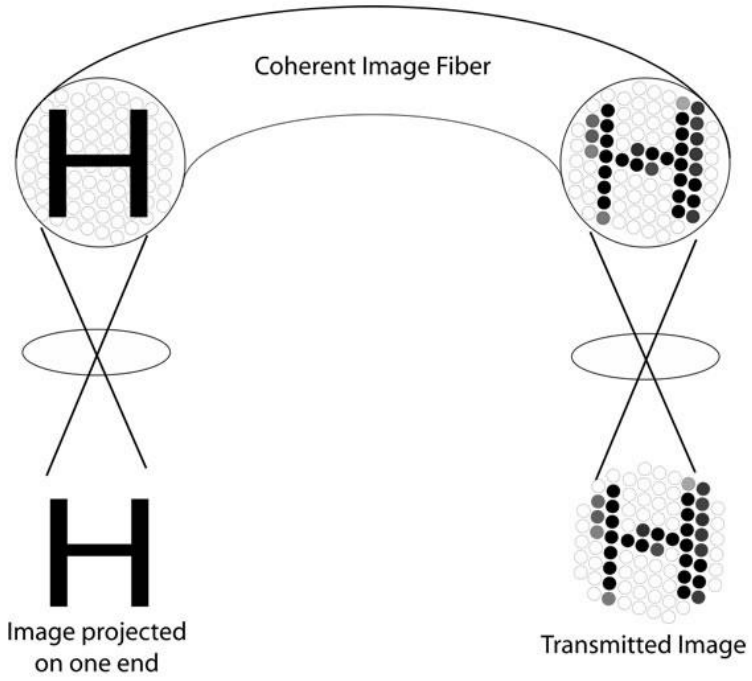

Fig.1-1 Optical fiber bundles

To inspect small organs, vessels, ducts inside human body, ultra-thin endoscope has been proposed by shrinking the entire diameter, however, ultra-thin fiber optic bundle endoscope less than 3mm could not perform a high quality image, typically, the minimum center to center interval core spacing of image units (optical fiber) is 3um, as shown in Fig.1-2 .If it produce high quality image with 1024 lines, more than 3mm overall diameter endoscope is demanded. Some makers provided a smaller size fiber optic bundle which is fit for ultra-thin endoscopic application [11], but the glass of it is suited for illumination in the visible to infrared range [12], not for wide field fluorescence imaging using UV excitation [13], obtaining higher resolution imaging at the cost of FOV. The unique benefic for fiber optic bundle is

offered as passive part, and there are some shortcomings for it, a bundle of optical fibers are fused in a single cladding as a semi-rigid endoscope, if one of them is fracture during bending, it will lead to create a dead pixel in the display. Unintended perforation will be caused by semi-rigid endoscope during a medical procedure [14].

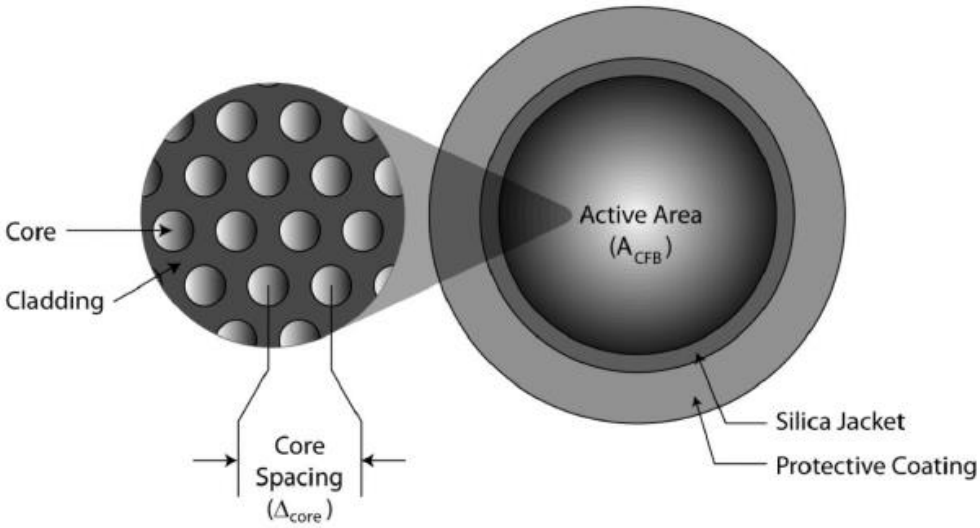

Fig.1-2 Coherent fiber bundle (CFB) cross sectional view

1.1.2 Image sensor (CCD or CMOS) for medical endoscope

Most medical endoscopes employed Charge-coupled Device (CCD) or Complementary Metal Oxide Semiconductor (CMOS) image sensor to capture lesions imaging. The image sensor is mounted on the distal end of shaft, and the white light illumination is transmitted through the fiber optic bundle [15], image sensor should be fabrication with many light-sensitive elements(as pixels) which can be used to form a imaging of the region of interest, A photon of light which falls within the element defined by one of the pixels will be converted into one (or more)

electrons and the number of electrons collected will be directly proportional to the intensity of the scene at each pixel. Every pixel in the video display is associated with an imaging element as shown in Fig.1-3, so it is difficult to be fabricated within smaller size without reducing image quality. For example, Kamiuchi H et al [16] proposed a 3-D endoscope using a single 1/10-inch CCD camera and pneumatic vibration mechanism; it is developed with overall diameter of 5mm, Andrew Catanzaro et al [17] has demonstrated a 4-mm diameter CCD video endoscopes for esophagoscopy in sedated and unsedated patients, Liqiang Wang et al [18] has developed a 2.5 mm miniaturized CMOS imaging module with real-time DSP technology for endoscope , for all the image sensor endoscopes, the vital limitation is the overall diameter.

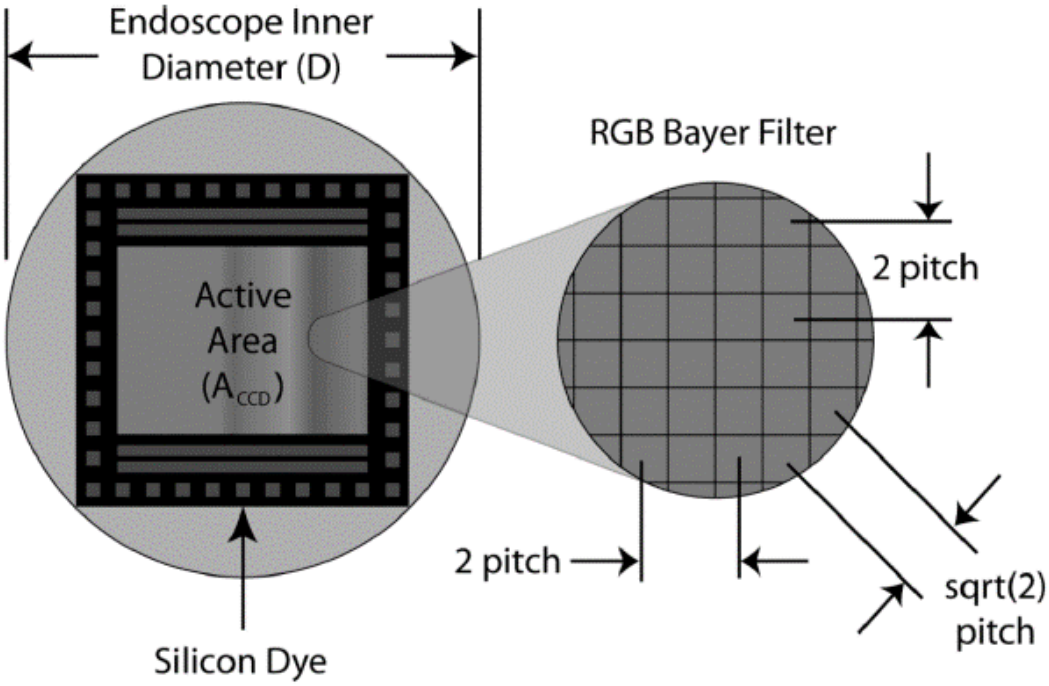

Fig.1-3 CCD image sensor with elements

1.2 Alternative scanning approaches to medical endoscope

A novel micro probe has been employed for medical endoscope, which is mounted on the end of endoscope, realizing a high resolution imaging, the scanning behavior and characteristic of these probes are achieved by driving micromirror oscillate, and the confocal image could be obtained. These micromirrors are fabricated by Microelectromechanical systems (MEMS) process [19-24]. The micromirrors could be used for light deflection and control. And the micromirrors commonly exist in diversified forms and could be actuated by variable driving mechanisms including electrostatic [25-28], thermal [29-33], magnetic effects [34-39], and piezoelectric actuation [40-44]. Typically, electrostatic driving mechanism is extensively utilized in the various applications, but it is not suitable for some aspect of the applications such as medical endoscopes used for in-vivo inspection, which has stringent constraint of voltage and temperature, usually electrostatic driving mechanism demands driving power up to 100V to obtain an adequate scanning angle [45]. The comb-drive mirrors have been mostly developed, although it is a versatile and simple design, a low force be generated, and high biasing voltage is demanded for this driving mechanism. Besides, instability of electrostatic driving is often of frequency occurrence because of pulling in voltage. Electro-thermal driven micromirrors have not complex MEMS fabrication process, showing a better optical scanning behavior than other mechanisms, for instance, Lei Wu et al proposed a electr-othermal micromirror with dual-reflective surfaces for endoscope application which can achieve a circumferential optical scanning using

dual-reflective mirror with ±45 °[46]. Jingling Sun et al developed a low voltage MEMS micromirror actuated by thermal bimorph, and the micromirror scans ± 30° optical angles at 5.5V voltage, the package enlarged the outer diameter up to 5.8mm [47]. However, electro-thermal driving has a vital shortcoming for working life due to that the near-perfect linear elastic properties of silicon will be lost. Another main limitation is large power consumption and scanning behavior depends on ambient temperature. For the piezoelectric driving mechanism, the piezoelectric material has the highest energy density as compared to the other silicon based actuators, primarily due to their large dielectric strengths. For example, F.Filhol, et al proposed that a resonant micromirror excited by a thin film piezoelectric actuator for fast optical beam scanning, 78 ° scanning angle was achieved with less than 1Vpp input power at resonance frequency of 10.9Hz in vacuum condition [48]. J.-H. Park et al., developed a high-speed metal-based optical micro scanner using stainless-steel substrate and piezoelectric thick films prepared by aerosol deposition method, scanning of 41° was obtained with 60Vpp at 28kHz [49]. Yasuda, et al illustrated that a piezoelectric 2D optical micro scanners with PZT thick films, the scanner demonstrate large optical scan angle 23 degrees (4.3 kHz for X-scan) by 52 degrees (90.3 Hz for Y-scan) at low driving voltages of typical 10–20 V AC with a 5 V dc offset[50]. Takayuki Naono et al developed a piezoelectric actuated MEMS optical scanner for endoscope application, showing maximum optical scan angles of 146° at 90 Hz, 148° at 124 Hz, 162° at 180 Hz, and 152° at 394 Hz at resonance in atmospheric pressure at driving voltage of 1.3Vpp [51]. The major disadvantage of

piezoelectric drive mechanism is complex fabrication process at high cost, sometime it is driven by high voltage to reach a large scanning angle. For magnetic actuation, sometimes magnetic driving mechanism is preferred by some researchers due to large scanning angle obtained at low power consumption, there are two types for magnetic driving, being driving by Lorentz force or magnetostatic force, Lorentz force is generated by being applied with external magnetic field, and coils should be pattern on the surface of moving parts of micomirror based on the complex MEMS process, electromagnetic actuation, although being capable of providing a large scanning angle, a bulky magnet core or magnet plate is required for generating magnetostatic force, further inevitably increases the overall size. For example, Niklas Weber, et al reported a tubular scanning endoscopic probe with an extremely compact hard magnetic micromirror which is mounted at 45 degree on a micro motor for realizing a circumference scan meanwhile the micromirror is driven by planar coil for linear scan, finally, a 3D tubular ring may be scanned, but the size of package is more than 2.7 mm [52]. Whereas these driving mechanisms depend on high temperature or high voltages for actuation and are not suitable for vivo inspection which has stringent constraint of voltages and temperature, further most of them are fabricated on the one side of brittle silicon wafer, which cannot be implanted into narrow organs because of their fragile structure and large volume, in conclusion, advantages and disadvantages of each actuation mechanism presented in Table.1-1

Table.1-1 Advantages and disadvantages of each actuation mechanism

Actuation	Advantages	Disadvantage
Magnetic	Low actuation voltage Relatively large angular deflection with lower driving power	Difficult to assemble permanent magnets and coils with CMOS technology Challenge in minimizing the size of device
Piezoelectric	High speed Low power consumption	Short actuation range High driving voltage
Thermal	Ease of fabrication (require only one composite beam) for bulk production	High power consumption Slow response time Fatigue due to thermal cycle
Electrostatic	Low power consumption Fast speed Ease of integration and testing with electric control circuity	Nonlinear characteristic Limited by the pull-in effect High actuation voltage Fabrication complexity

1.3 A novel scanning approach to medical endoscope

With the development of medical and clinic requirement, ultra-thin (size of package less than 3mm) medical endoscopes have been needed in the past decades. It is essential to shrink overall diameter (less than 3mm) of medical endoscope, a bundles of optical fiber or a pixel-array camera demands one optical fiber or element for each pixel within the visualized image. When their overall diameter is diminished less than 3mm, either field of view is confined or resolution of image acquisition is reduced [53], as a consequence, an alternative way is to produce the optical scanning

with a single optical fiber by micro actuator, thus compromising the interdependence between reducing image quality and shrinking overall diameter. Typically the single optical fiber scanner mainly consists of a 125um single optical fiber, a micro actuator and lens. Micro actuator can be divided into several categories such as PZT actuator [54.55], electromagnetic actuator [56], and micro motor [57]. Lens includes lens system [58] and GRIN lens [59]. Like all the structures, these scanners have their resonant frequency, when the frequency of supplied power is equal to the resonant frequency, they will vibrate at the largest amplitude. They can vibrate to scan laser beam at certain pattern on to image plane, Amplitude-modulated control can be introduced into producing 2D resonant scanning, in general, the scanning pattern exist at three forms like raster scanning, spiral scanning, and propeller scanning.

1.3.1 PZT actuator

To realize wide field of view and high-resolution of endoscopic diagnose from an ultra-thin fiber scanner which can lead laser inspection and therapeutic tools to narrow internal organs of the human body that were previously inaccessible to minimally-invasive medical procedures, such as the blood vessels, pancreatic and bile ducts, Ultra-thin PZT tube actuators are developed by some group, for instance, Cameron M. Lee, et al. [60] proposed a 1.6mm diameter mechanically resonant fiber scanner. This scanner comprises of a single optical fiber that is cantilevered from the tip of a tubular piezoelectric actuator, held by a mounting collar, the cantilevered free end of this optical fiber can be vibrated near its mechanical resonance, 20 optical

return fibers, which are used for collecting scatting light off the image plane, low NA endoscope lens assembly that is used for calibrating the fiber scanner for high image quality, which can obtain FOV of 75° and less than 20 um resolution at image zooming. Mon Thiri Myaing et al illustrated a 2.4 mm fiber-optic scanning two-photon fluorescence endoscope, which is also actuated by a tube PZT actuator, but the cantilevered optical fiber is double-clad fiber differed from conventional use of single optical fiber, although a better real-time imaging has been demonstrated, 70 V voltage power was supplied to obtain adequate deflection [61]. Yicong Wu et al developed a miniature two-photon fluorescence endomicrosopy actuated by PZT tube with compound lens and multi-fiber collector, which can miniature the chromatic aberration and capture a high-resolution image due high collection efficiency [62]. Eric J. Seibel1 et al developed a highly flexible, 1-mm fiber scanner endoscope for wide-field, using a small diameter piezoelectric tube actuator, the optical fiber cantilever can produce 33° mechanical scanning angle at second mode resonance by etching overall diameter of it from 125μm to 12μm [63]. Reducing diameter produces a large mechanical scanning angle and great flexibility while decrease hardness and service life, further smaller piezoelectric tube is difficult to fabricate.

1.3.2 Electromagnetic actuator

Although PZT actuator can perform a larger FOV, greater mechanical scanning angle, and tuning frequency by different length of cantilevered optical fiber, showing a great potential for medical endoscopic application, they are still underutilized for

minimally-invasive medical imaging, diagnosis and surgery because of their fragility and high cost, further PTZ material is not good for the health. As 3D fabrication technology has been extensively developed recently, patterning is not limited to flat surface of substrate, functional pattern is capable of being fabricated on the outer or inner curved surface of cylindrical substrate [64]. Tadao Mastunaga et al from Tohoku University developed a non-planar photo-fabrication technique, which can be employed to fabrication complex pattern on cylindrical capillary, two tilt driving coil were fabrication on a 1.08 mm polyimide capillary as an electromagnet actuator, and a single optical fiber with permanent magnet can be actuated to realize a spiral scan. Coil actuator with 45º tilt-angle and 200μm coil pitch was successfully obtained, showing 18.7μm amplitude and less than 1 degree mechanical scanning angle, the reason of that is low driving force [56].

1.3.3 Micro motor

Apart from the PZT actuator and electromagnetic actuator, micro motor also are preferred for ultra-thin endoscopic application, in general, the diameter of micro motor is less than 2.5mm, always being integrated with a prism or tilted mirror for endoscopic application. For example, Peter H. Tran et al developed a novel endoscopic optical coherence tomography probe, where a prism mounted on a micro motor can deflect light to create circumferential scanning way at distal end. Furthermore high rotation speed can be achieved, rotated scan with linear scan provide a 3D high-resolution imaging [65], Babak Assadsangabi illustrated a micro

rotary moto where a permanent magnet rotor is levitated by ferrofuid used as an extremely simple bearing material, the levitated rotor is electromagnetically driven by two photofabricated meander type coil patterned around the outer walls of catheter that enable 90º step angular rotation. A 1 mm prism mirror is connected to the motor and rotated to realize circumferential scan. Niklas Weber, etc. study on tubular scanning endoscopic probe with an extremely compact hard magnetic micromirror which is mounted at 45 degree on a micro motor for realizing a circumference scan meanwhile the micromirror is driven by planar coil for linear scan, finally, a 3D tubular ring may be scanned, but size of package is more than 2mm [53].

1.4 Scanning pattern for single optical fiber scanner

Scanning pattern for single optical fiber endoscope can be mainly categorized into three types which are mentioned above, here will be introduced in detail. Scanning patterns can be built by certain modulating the input driving signal, a typical raster scanning pattern can be created by quick horizontal scanning using a mechanically resonating cantilevered fiber combining with slow vertical scanning using a galvo-mirror, as shown in Fig.1-4(a). The shortcoming of utilizing galvo-mirror is its larger volume and mass. Further nonaxisymmetrical scanned geometry can also be created. If the mirror is removed, it would result in significant weight, size and power savings. A tube-shape actuator is very useful for building 2D resonating scanning pattern. It can drive optical fiber moving horizontally and

vertically, and the movement of the tubular actuator is small, typically, sinusoidal driving signal is applied to the actuator, the fiber will vibrate at both directions at certain scan period. Lissajous patterns can be created by modulating two sinusoidal driving signals. By setting the frequency ratio of two signals, various closed pattern can be created stably. If the frequency ratio of two signals is 1:1 with 90 phase shift, a circle scan can be created. The amplitudes of a circular scan are modulated in a triangle pattern while the phases are kept constant. A spiral scanning can be performed, as show in Fig.1-4 (b). A propeller scan can be generated with tubular actuator, as seen in Fig.1-4(c). A 1:1 Lissajous pattern creates a 45 tilted line when the horizontal and vertical sinusoidal driving signals are of identical frequency, amplitude and in-phase. To produce a space filling scan, 45 tilted lines can be rotated in a continuous by modulating the horizontal and vertical amplitudes.

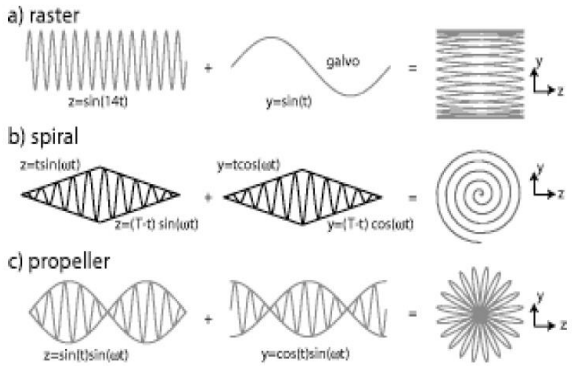

Fig.1-4 Three scanning patterns

1.5 Calibrating single optical fiber scanner

Typically there are three types of a single optical fiber for delivering or collecting

light. (1) Single mode fiber has a very small core diameter of 8 um; single mode fiber has only a single spatial mode of light. There are two layers with different refractive index. They are inner core and outer cladding respectively, transmitting light by total internal reflection. The single mode fiber is well suited for the scanning-based imaging modalities; it can be used for limiting near diffraction in the sample plane for high resolution imaging. Some endoscopes use it as confocal pinhole, involve with relatively large scanning system at the distal end. Giniunas et al. built and tested a scanning confocal microscope using a single-mode optical fiber for illumination and collection. To reduce off-axis aberration, single mode fiber is always lensed with a long GRIN lens [66]. For example, Niklas Weber et el developed 3D confocal micro-scanner with a laterally scanning fiber driven by a piezo tube, a tunable liquid filled lens and a GRIN lens, all mounted onto a Si micro-bench with fluidic structures for actuating the tunable lens[67]. (2) Double-clad fiber (DCF) is a class of optical fiber with a structure consisting of three layers of optical material instead of the usual two. The inner-most layer is called the core. It is surrounded by the inner cladding, which is surrounded by the outer cladding. The three layers are made of materials with different refractive indices. This kind of fibers is capable of supporting single mode propagation by the core and multi-mode by the inner cladding. It can achieve both excited pulse delivery and collection of fluorescence light. In spectrally encoded imaging, double-clad fiber was used to reduce speckle noise [68]. Rivera et al. presented a compact and flexible endoscope where a miniaturized resonant/nonresonant fiber raster scanner is

employed. The scanner was assembled by mounting a DCF and multi-element GRIN lens assembly [69]. (3) A single multimode fiber has large diameter with large core diameter, multimode fibers with parallel information transport have more than one spatial mode of transmitting light. It is also considered an ideal optical unit for endoscopic imaging due to the possibility of direct image transmission via multiple spatial modes. For instance, Youngwoon Choi et al illustrated a wide-field endoscopic imaging by using a single multimode optical fiber [70]. (3) Objective Lens, the objective lens is the optical element that gathers light from the object being observed and focuses the light rays to produce a real image. For endoscope application, objective lens need provide high optical resolution and great collection efficiency. For example, a GRIN microlens probe is used for mammalian brain inspection, 2.5um optical resolution has been demonstrated [71]. Eric J. Seibel developed a PZT actuated 1-mm catheterscope with objective lens assembly, generating 500-line images at maximum fields of view of 100 degrees and spatial resolutions of <20 microns with image zooming [72]. Onur Ferhanoglu et al propose a PZT actuated high speed ultrafast laser microsurgery with aspheric lens with 0.3 NA, realizing lateral and axial resolutions of 1.16 μm and 11.46μm, respectively [73].Li Huo et al illustrated a PZT actuated forward-viewing resonant fiber-optic scanning endoscope with GRIN lens, working with a 40-kHz swept-source OCT (SS-OCT) system has been demonstrated for 3D OCT imaging of biological tissues [74]. Yicong Wu et al developed a PZT actuated Scanning fiber-optic nonlinear endomicroscopy with miniature aspherical compound lens, improving the optical

performance of a fiber-optic two-photon fluorescence (TPF)/ second-harmonic generation (SHG) endomicroscope [63]

1.6 Optical modalities

1.6.1 Optical tomography coherence (OTC) for endoscope

Optical tomography coherence (OTC), a kind of non-invasive optical imaging modality, recently has been introduced into endoscope, this optical system enable to provide 2D or 3D high resolution in vivo and in situ images, create the image of multilayer structures of internal tissue with high penetration depth. At the beginning, OCT technology is created by Huang et al. [75] and has been improve to time domain system Swanson et al [76] and Drexler et al. [77], recently has been evolved into Fourier domain system developed by Fercher et al. [78], Häusler and Lindner [79], and Yun et al. [80]. So OCT has been widely accepted by some practical application, especially in ophthalmology and other biomedical applications. The fundamental structure of OCT system is shown in Fig.1-5. The principle of OCT is white light or low coherence interferometry, the optical setup typically consists of an interferometer with a low coherence, broad bandwidth light source. Light is split into and recombined from reference and sample arm respectively. Over the past decades, OTC has been extensively developed for endoscope application [81-85].

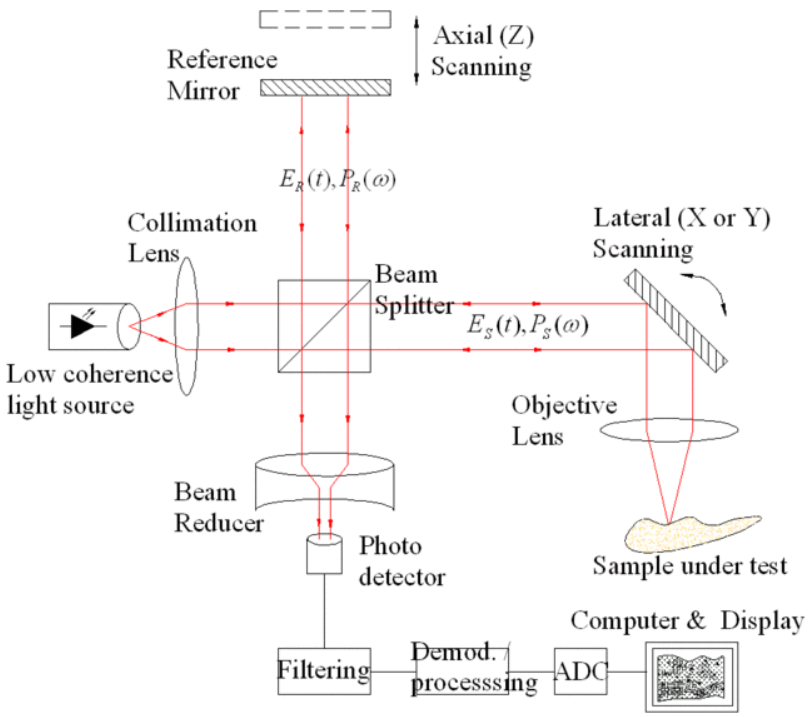

Fig.1-5 Fundamental configuration of OCT system (referred from WIKIPEDIA)

1.6.2 Confocal microscopy for endoscope

Confocal laser scanning microscopy (CLSM or LSCM) is optical system for visualizing a high resolution image of sample with selected depth. The major characteristic of confocal microscopy is its capacity to obtain in-focus images from a selective depth, a process known as optical sectioning. The images of samples are captured point by point and recombined with computer, allowing a high-resolution 2D or 3D image of sample. This technique is originally used for microscope and the structure of optical system is presented in Fig.1-6, in practical, a point light source is provided by employing a laser light going through a pinhole. Point light is directed to the sample pass through beam splitter and objective lens. The point source scans or moves horizontally on the sample by integrated scanner, the light reflected by

sample in focal passes through the image pinhole, forming a point image on the detector PMT(photon multiply tube). Scanning a sample at certain depth form a 2D optical section at selected depth, if confocal images obtained at different depth are accumulated, a 3D optical image will be formed successfully. Recently, confocal microscopy technique has been frequently involved with single optical fiber scanner endoscope, as a non-invasive optical biopsy technique, instead of conventional biopsy, is capable of providing 2D and 3D high resolution image [86-88].

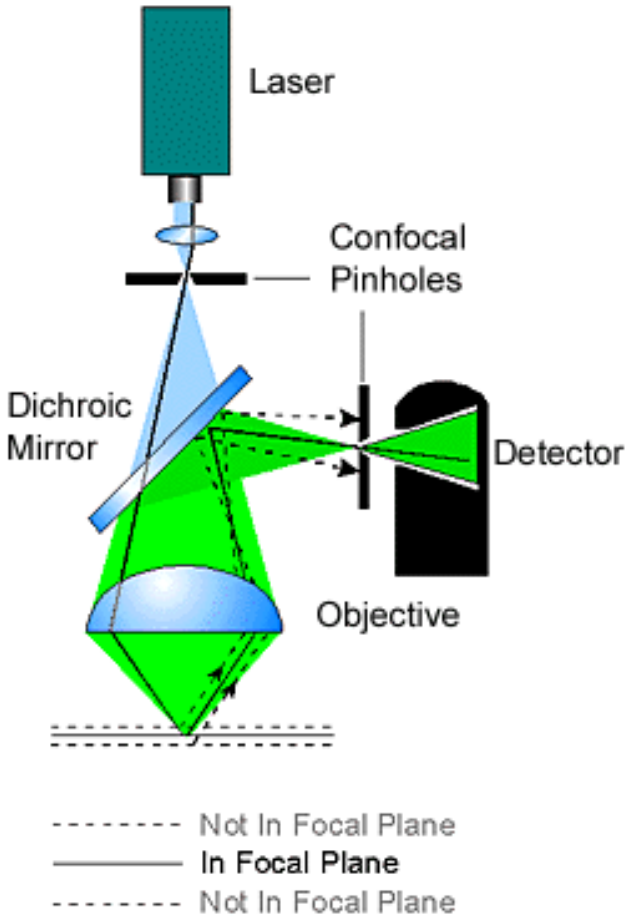

Fig.1-6 Fundamental configuration of confocal system

1.7 Research Goal and Tasks

Our goal is to produce an ultra-thin electromagnetic-actuated fiber scanner for flexible endoscope (diameter<2mm), single optical fiber is actuated by two ultra-thin tubular tilted-coil-shape actuators, realizing a spiral pattern. The tilted microcoils could be fabricated on the surface of a 1mm polyimide pipe based on 3D MEMS process including 3D lithography technology and 3D printing technology, like all MEMS structures, this fiber scanner has its resonant frequency and performs a larger displacement of fiber tip at it. In order to increase scanning angle, a two degrees of freedom fiber scanner is introduced into this research, if a lumped mass is attached to the fiber tip, a larger scanning angle should be realized at second-order resonant model without larger displacement of fiber tip. In conclusion, the specific design goals are listed as followings:

(1). An ultra-thin fiber scanner should be designed for realizing spiral scan for medical endoscope application;.

(2) Optimal parameters of actuator should be designated for providing larger driving magnetic field and force.

(3) Optical mechanical structure would be designed for offering large scanning displacement and angle of fiber tip.

(4) A novel 3D fabrication method would be developed for fabricating tilted microcoils actuator on the surface of pipe substrate.

1.8 Dissertation Overview

There are six chapters comprised in the dissertation. The first chapter introduces the background and goal of this project, including the conventional and new biomedical imaging technologies for endoscope application, some corresponding miniature endoscopes currently have been developed, and the proposed research objectives and tasks.

In Chapter 2, a novel design of ultra-thin fiber scanner based on MEMS is firstly presented after comprehensive literatures are reviewed. The general design and details have been claimed, including parameters of components, material, principle of operation and method.

Chapter 3 presents theory and numeric analysis of designed fiber scanner. The principle of operation has been introduced from theory, and magnetic field and magnetic force have been simulated. Considering the particularity of tilted microcoil, off-axis magnetic field also has been analyzed with different parameters of tilted microcoil. The structure of fiber scanner and related vibration theory are elaborated in this chapter, resonant frequency and scanning angle have been simulated with varying structure of fiber scanners.

In Chapter 4, an improved structure of fiber scanner has been demonstrated. A lumped mass is added on the fiber tip to realize two degree freedom vibration system. Mode shape, natural frequency and scanning angle are demonstrated with different mass ratio.

Chapter 5 presents fabrication process comprised of sputtering, spray coating, 3D

lithography process, etching and electroplating. Each process has been introduced at details. Finally, the shortcomings of MEMS-based tilted microcoil have been shown.

In the Chapter 6, a novel hybrid process for fabricating tilted microcoil is demonstrated, and the process integrated with 3D printing technology and homemade shows an efficient and low cost way.

Finally, the entire research efforts and a list of accomplishments will be summarized in Chapter 7, together with suggestions for future work and potential research opportunities of the project.

2. ELECTROMAGNETIC-ACTUATED FIBER SCANNER BASED ON 3D LITHOGRAPHY PROCESS

2.1 General design of fiber scanner

A scanning-based, ultra-thin medical endoscope has become an invaluable tool in biomedical filed, enabling rapid, high-resolution, high-collection efficiency scanning behavior for inspection of narrow internal organs such as blood vessels, artery, lactiferous ducts and so on. To overcome the limitation or tradeoff between scanning effect and miniaturized size, cylindrical micro actuator assembled with a single optical fiber has been addressed by some groups, obviously, PZT actuator is the mainstream, which could be fabricated down to 400um diameter, providing a wide FOV and high scanning frequency, but there are still a few disadvantages following as: (1) high cost and (2) large driving voltage.

As is well-known, the major characteristic of the electromagnetic actuation is low power consumption compared with piezoelectric actuation. So an electromagnetic actuator has been proposed here. The schematic of the whole fiber scanner is illustrated in Fig.2-1. This optical fiber scanner consists of a 1mm diameter polyimide pipe, two tilted micro coils (X-axis driving coil and Y-axis driving coil), an optic fiber, a cylindrical magnet, a lens and stationary fixture. When the sinusoidal signal is offered to X-axis driving coil, this coil will drive magnet moving periodically along X-axis direction, if the same signal with 90° phase shift is

supplied to Y-axis driving coil, the fiber tip will perform a circular scan, as Lssajous pattern. Here it is needed to highlight that distortion and lag are not taken into consideration. By modulating two the sinusoidal driving signal with a smooth envelop, that can result in a spiral scanning pattern as shown in Fig.2-2, where the scanner radius varies linearly in time. As all scanners, this scanner has its resonant frequency, the frequency of driving signal is equal to the natural resonant frequency of the scanner, and it will perform large scanning displacement and angle of fiber tip.

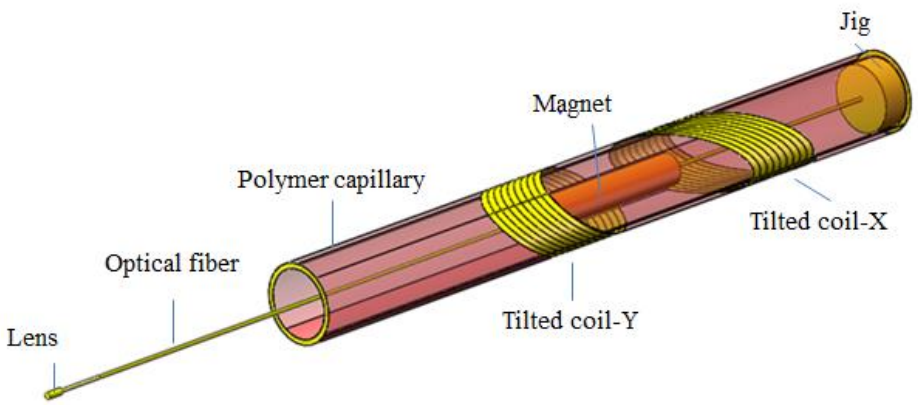

Fig.2-1 Schematic of the proposed fiber scanner

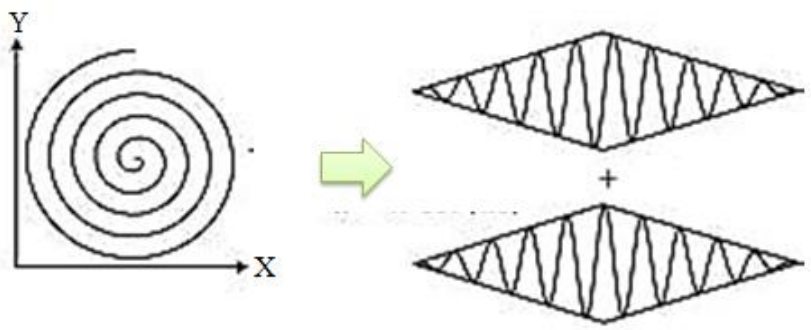

Fig.2-2 Spiral scanning

2.2 Component design

After finishing the integrated design, major component design should be taken into consideration.

2.2.1 Optical fiber with magnet

In this research, an optical fiber with magnet can be regarded as one component, because it is fabricated by directly electroplating soft magnetic material CobaltNickel (CoNi) on the surface of the optical fiber, as shown in Fig.2-3. As mentioned above, optical fiber could be classified into two categories: (1) Single mode optical fiber and (2) Multi-mode optical fiber, here, a single multi-mode fiber is used as an ideal optical element for endoscopic imaging due to the possibility of direct image transmission via multiple spatial modes. It is easy to collimate light path. So a single multi-mode optical fiber is selected for delivering and collecting light. There are two layers with different refractive index. They are inner core and outer cladding respectively, transmitting light by total internal reflection, being well suited for the scanning-based imaging modalities, it can be used for limiting near diffraction in the sample plane for high resolution imaging, the length of the optical fiber can be 9mm-14mm, optical fiber length is critical parameter for fiber scanner, because the natural frequency of the cantilevered optical fiber is depend on the length of optical fiber and mass of magnet, scan speed is decided by the resonant frequency, in practical, the value means the number of scanning line per second on the sample, it is also used for determining the time resolution of an optical system,

high frequency is on behalf of high time resolution, in instance, at 400*Hz*, scan a 512 lines demand 1.28 seconds, accordingly 1000*Hz* is 2.5 times faster than 400*Hz*.

Typically, the technical magnet used for electromagnetic actuation is ferromagnetic, performing significantly great magnetic permeability μ_m and according to $B = \mu_m B_0 = \mu_m \mu_o (H + M)$, that causes an obvious increasing of the magnetic flux density *B*, *H* is applied external magnetic field, and *M* is the internal magnetization, ferromagnetic material can be categorized into soft and hard magnetic materials, with different hysteresis loop, here we use soft magnetic material CoNi, as shown in Fig.2-4.

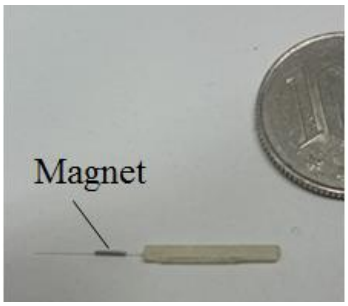

Fig.2-3 Single optical fiber and magnet

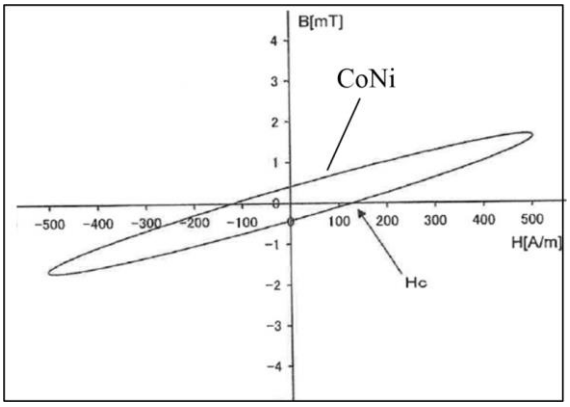

Fig.2-4 B-H curve of CoNi

Low coercive field strengths H_{soft} is presented, means that magnetization direction can be altered by low external magnetic field, so it is very suitable for scanning application. So the material CoNi is chosen as material of magnet, and the material property, dimensions of magnet is presented in Table.2-1,

Tab.2-1 Material property and dimensions of magnet

Magnet. Length (mm)	Magnet. Outer diameter (mm)	Magnet Inner diameter (mm)	Coercive field strengths (A/m)	Magnetic saturation (A/m)
3	0.6	0.125	503.1	124.7

2.2.2 The tilted Microcoil

The tilted microcoil would be fabricated on the surface of a polyimide pipe based on the 3D lithography MEMS process, which will be introduced in detail in the later chapter. A custom-made polyimide with the outer diameter of 1mm and the inner diameter of 0.9mm is provided by the SCHOTT MORITEX Corporation. It is selected by two important characteristics, first of all, it is a good heat-resisting insulator, and another important characteristic of it is thin-wall feature which provides a large internal space. The property of the polyimide pipe is shown in the table.2-2.

Table.2-2 The property of the polyimide capillary

Polyimide pipe O.D (mm)	Polyimide pipe I.D (mm)	Heat resistance (°C)	Dielectric constant	Coefficient of thermal expansion
1	0.9	400	3.4	4.0×10-5/°C

As the substrate and the fabrication process is decided, the parameters of the designed tilted microcoil should be considered, they are coil pitch, tilt-angle, turns, and the thickness of coil line respectively, as shown in Fig.2-5

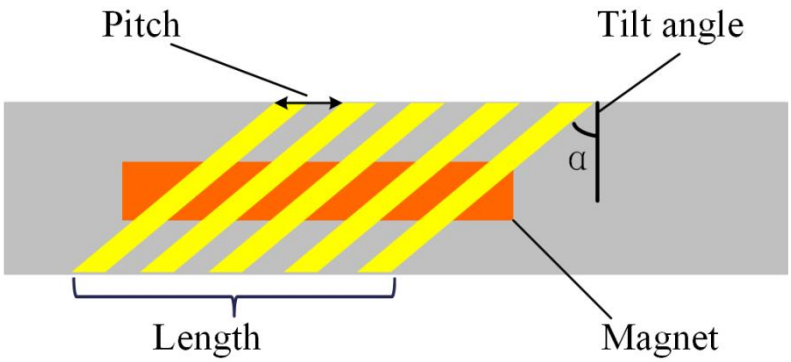

Fig.2-5 The parameters of tilted microcoil

3. THEROY AND MAGNEIRC ANALYSIS

An electromagnetic-actuated single optical fiber scanner has been designed for ultra-thin medical endoscope application, as an ultra-thin electromagnetic actuator, the main geometric parameters of the tilted coil and material characteristic of magnet should be designed in detail, electromagnetic property and driving force should be taken into consideration compulsorily. Beyond that vibration performance is also essential for mechanically resonant fiber scanner. This chapter will discuss these aspects respectively from theory and numeric analysis, including magnetic field analysis, magnetic force calculation, resonant frequency and deflection analysis and creative design of motion of two degree vibration system.

3.1 Magnetic field analysis

To analyze the magnetic characteristic of tilted microcoil, the commercial software ANSYS Maxwell was used. A straight tubular model is used as a close winding coil model in this software, so an inclined plane tubular model is built as a tilted coil. In this work, a 45 º and 60 º inclined coil have been modeled and simulated, and the material of the models are copper, being supplied with 50mA DC power. Simulation results of magnitude and direction of magnetic field and cloud chart of magnetic field distribution generated by 45º and 60º tilted micro coils are shown in Fig.3-1. A tilted internal magnetic field is generated by a tilted microcoil, and the direction is vertical to inclined plane of tilt coil. It indicates that maximum

internal magnetic field gradually decreases to both end.

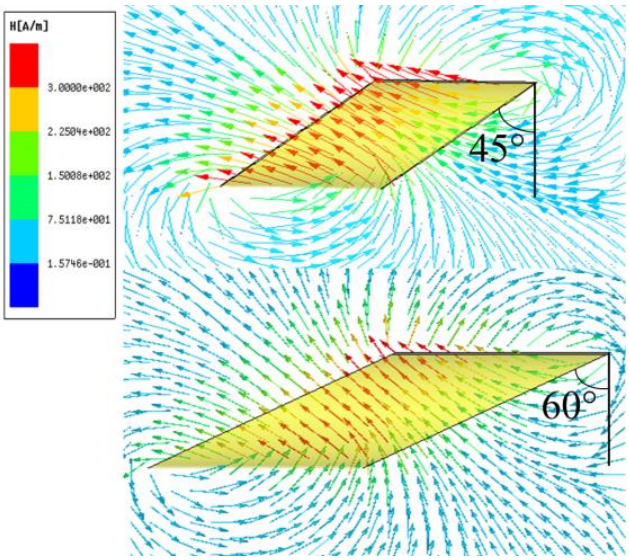

Fig.3-1 Magnetic field generated by 45 º and 60 º inclined coil respectively

3.2 Magnetization analysis

Ferrimagnets retain their magnetization in the absence of a field, and the domains are randomly oriented in an unmagnetized material, which provide that the net magnetic moment is zero as shown in Fig.3-2(a), when placed in an external magnetic field, then magnetic moment of domains can be align along the direction of magnetic field as illustrated in Fig.3-2(b).

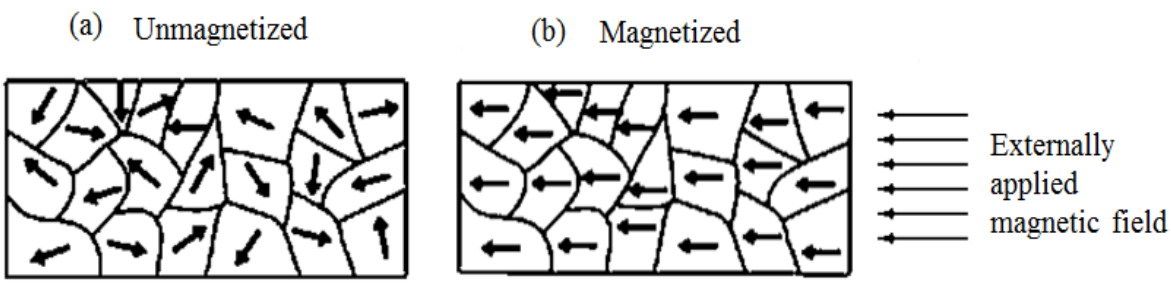

Fig.3-2 (a) Unmagnetized and (b) magnetized (domains aligned)

3.3 Magnetic force analysis

A magnet placed in a magnetic field will experience a torque, the magnet will be aligned itself along the magnetic field lines by the torque and will experience oscillation with the alternative magnetic field.

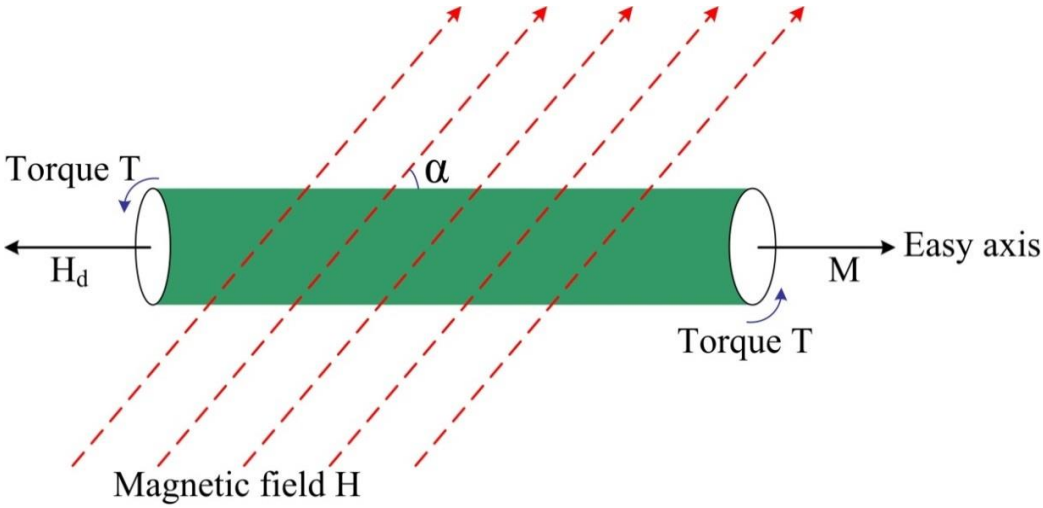

Fig. 3-3 Schematic of torque T calculation

In this work, a CoNi cylinder is placed inside a tilted microcoil applied with AC power. A tilted alternative magnetic field will be produced by the tilted microcoil. The CoNi cylinder will be magnetized and vibrate periodically by the alternative torque as shown in Fig.3-3. A torque T proportional to F is generated on the magnet can be expressed as:

$$T = V \times \left| \vec{M} \times \vec{H} \right| = VMH \sin\alpha \propto F \tag{3.1}$$

Where V is the volume of CoNi cylinder, H is the magnetic field generated by the tilted microcoil. M is the magnetization vector, in a simple permanent magnet

analysis, M is assumed as the fixed value, in soft magnetic material like CoNi, M varies as a function of the applied magnetic field. And α is the angle between the magnetic field lines and the magnetization vector. According to the Judy and Muller [89], when such a magnet is placed in the magnetic field, it can be magnetized by the component of magnetic field H_a along the easy axis and be expressed as:

$$H_a = H\cos\alpha \tag{3.2}$$

M increases and the magnetic poles are formed at the both ends of magnet. These poles generate a filed called the demagnetizing field H_b, which opposed the direction of H_a; M is varied as a function of the applied magnetic field H as:

$$M \approx \min\left(\frac{\mu_0\left(H_c + H\cos\alpha\right)}{N_D}, M_s\right) \tag{3.3}$$

Where μ_0 the permeability of vacuum, H_c is the coercive field of magnetic material, M_s is the saturation magnetization. N_D , is the shape anisotropy coefficient of the magnet in the direction of magnetization. And the shape anisotropy coefficient N_D can be expressed as:

$$N_D = 1 - \frac{\left(l/d\right)}{\sqrt{\left[1+\left(l/d^2\right)\right]}} \tag{3.4}$$

Where l and d are the length and the diameter of the magnet respectively. In this research, the length and the diameter of the magnet are defined as constants. They are 3mm and 600um respectively. We assumed that the magnet is magnetized

to saturation, M is equal to M_s. So there are internal magnetic field H of coil and angle α being variables seen from equation 3.1, the magnetic field are affected by the parameters of the microcoil such as coil pitch, turns and so on, angle α is represented for tilt-angle of the tilted microcoil according geometrical relationship. To optimize these parameters, magnetic force was simulated numerically by commercial software ANSYS Maxwell, providing a convenient method and precise results. Coil pitch is a decisive factor for the magnetic field intensity: the smaller coil pitch, the larger magnetic field intensity. Nonetheless, the coil pitch is restricted by the fabrication process, so it is designated as 80 μm according to our fabrication ability.

All the simulation model consists of two parts: tilted microcoil model and magnet model. The tilted microcoil models were built in different parameters, which would need to be optimized. And they are tilt-angles, turns, and relative positions respectively. The material of the tilted microcoil models are copper, being applied with 50mA AC power. A 3mm length and 600μm diameter magnet was established, being made of soft magnetic material CoNi that shows low coercive field strengths.

It is apparent from the Fig.3-4, the thickness and turns of tilted microcoil model are 5um and 20 accordingly, the magnetic force revealed a gradual rising, as the tilt-angle increases. It is consistent with theory of torque calculation in which torque can increase with increased angle α. As can be seen from the simulation results, the tilt-angle is larger, the magnetic force is greater. However, the tilt-angle is very limited by our fabrication ability, a large tilt-angle (larger than 60º) is difficult to

fabricate on account of the insufficient running accuracy of stage and underexposure. Thereby, to obtain a large magnetic force, a 60º tilt-angle was chosen for fabrication.

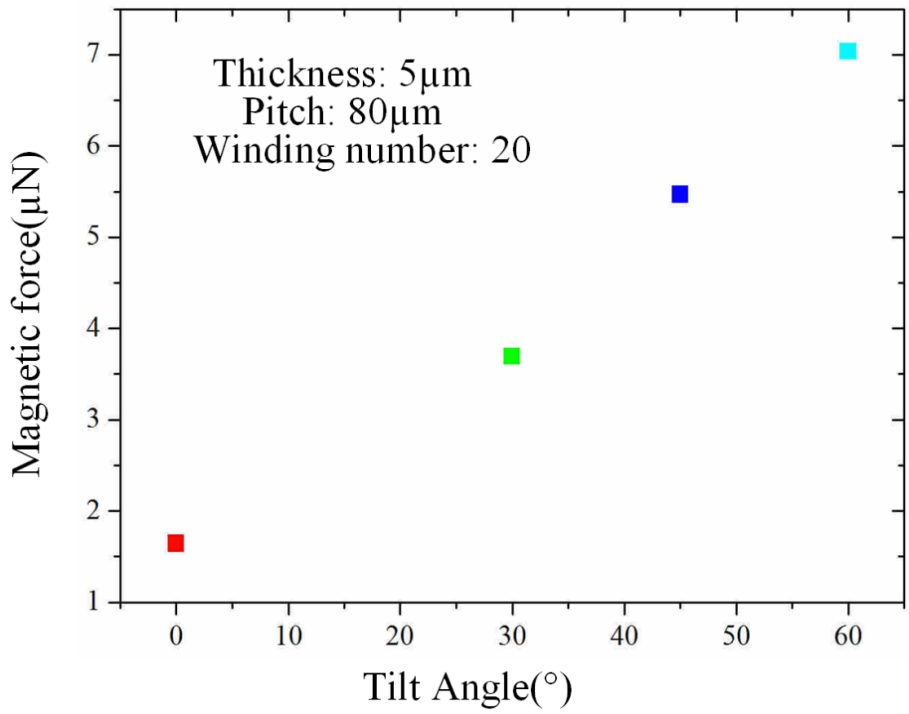

Fig.3-4 Simulated magnetic force with different tilt-angles

The tilt-angle was decided by the simulation result and the fabrication ability, subsequently, the magnetic force has been simulated with different relative positions between tilted microcoil and magnet. The relative positions can be divided into five items, they are more left, left, middle, right, more right respectively, as shown in the bottom of Fig.3-5, the more left and the more right indicate that the two third of volume of magnet is located outside tilted microcoil, the left and the right position means that half of the volume is kept outside tilted microcoil, They are marked from A to E accordingly, in the simulation result, the maximum force is obtained at location of B or F where half of magnet is placed outside tilted microcoil. It also was

simulated with two different thicknesses of coil line 5 μm and 15 μm respectively. And the results have been gained in same curvilinear trend with various values.

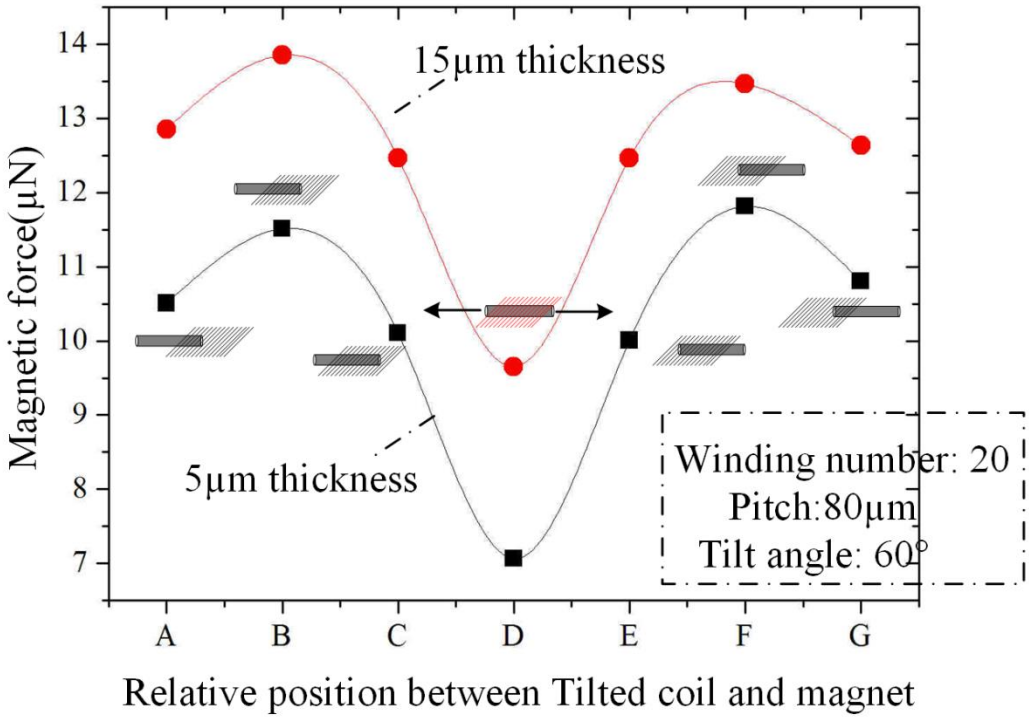

Fig.3-5 Simulated magnetic force with varying relative positions between tilted microcoil and magnet

Magnetic force was simulated with increasing turns (ranging from 10 to 40) with the tilt-angles of 30º, 40º and 60º respectively, presented in Fig.3-6. The magnetic force induced by turns of 10 is quite small, because that magnet is magnetized inadequately, a large magnetic force was obtained by 60º tilt-angle microcoil with 20 turns, and when the turns is equal to or more than 20, the line remains level, it indicates that when the half of the magnet is placed in a enough long tilted microcoil such as 20 turns tilted microcoil, it will be magnetized to saturation by the tilt

magnetic field, the almost identical magnetic forces are produced by 20, 30, 40 turns, being independent of turns.

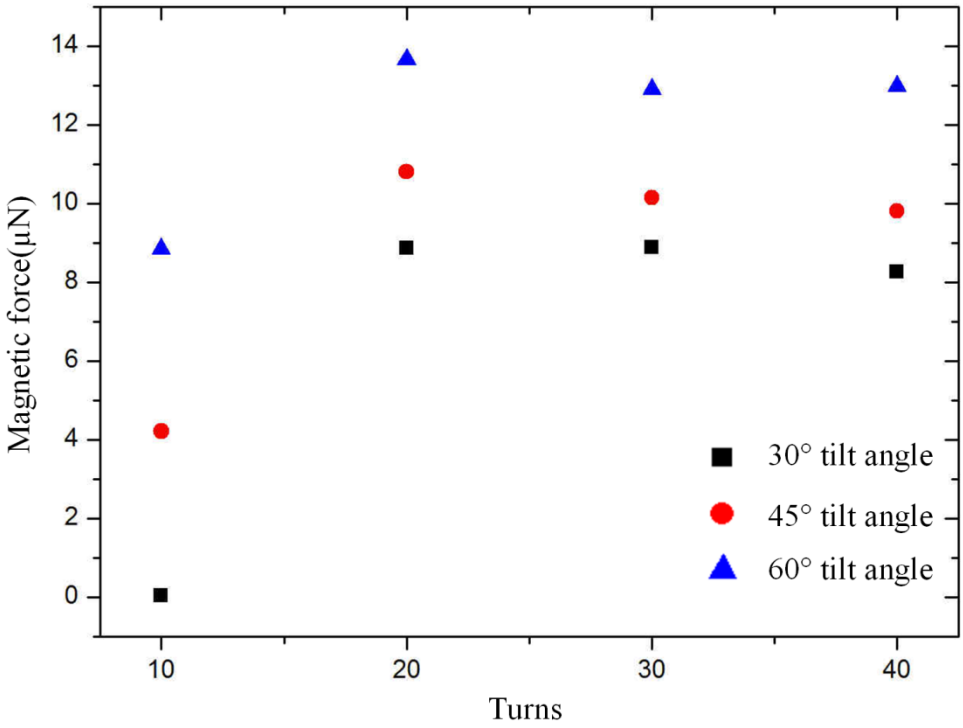

Fig.3-6 Simulated magnetic force with increasing winding number (from 10 to 40) under tilt-angles of 30º, 45º and 60º respectively.

These results indicate that when the tilt-angle is variable with the other parameters as constant, 60º tilt-angle microcoil performs a larger magnetic force on the magnet; when the relative positions between tilt microcoil and magnet is different, the magnetic force changes continuously and is the largest one at B or F position; when the magnet is placed at B position and driven by 10, 20, 30, 40 turns microcoils respectively, there is a larger magnetic force existed at microcoil of 20 turns with all tilt-angles.

3.4 Summary

The chapter presents fundamental theory of magnetic field analysis, magnetization analysis and magnetic force driving. The principle of operation of actuator has been claimed. To explore magnet field of tilted microcoil, the magnitude and direction of magnetic field of tilted microcoil have been simulated with using Maxwell for two different tilt-angles 45º and 60º. The strongest tilt magnetic field exists in the center for both models.

To optimize design parameters of tilted microcoil, magnetic force generated on the magnet by a tilted microcoil has been simulated with different parameter of tilted microcoil. They are tilt-angle, thickness of coil line, relative position between magnet and tilted microcoil respectively, the pitch is applied as 80μm according to inspecting fabrication ability.

These results indicate that when the tilt-angle is variable with the other parameter as constant, 60º tilt-angle microcoil performs a larger magnetic force on the magnet; when the relative position between tilt microcoil and magnet is different, the magnetic force changes continuously and is the largest one at B or F position; when the magnet is placed at B position with 10, 20, 30, 40 turns respectively, there is a larger magnetic force existed at microcoil of 20turns with all tilt-angles.

As a result, 20 turns, tilt-angle of 60º, 80μm coil pitch and 15μm thickness coil line are selected as design parameters for fabrication in the future work.

4. OFF-AXIS MAGNETIC FIELD ANALYSIS

From the aforementioned simulation results, different magnetic forces were demonstrated with varying relative positions between tilted microcoil and magnet, and they are classified into three types (1) the whole magnet inside tilted microcoil; (2) the half magnet inside tilted microcoil; (3) much less than half magnet inside tilted microcoil; the large magnetic force was obtained at the half magnet inside tilted coil, so the magnetic force is not only affect by the internal magnetic field, but also by the external magnetic field, so the external magnetic field generated by tilted microcoil should be taken into consideration.

4.1 Theory analysis

Firstly, we calculated the magnetic field generated by one loop of tilted microcoil, in this research, the magnetic field of p point will be will be analyzed using off-axis magnetic field model, as shown in Fig.4-1.

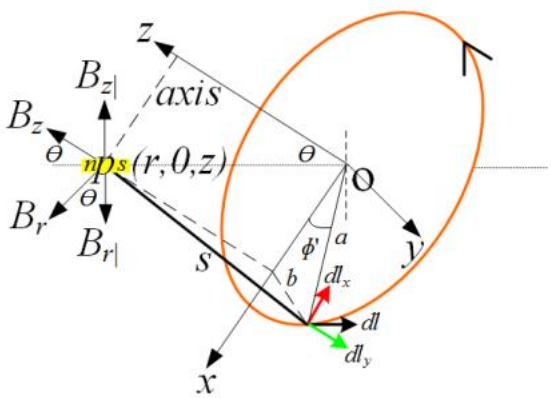

Fig.4-1 Calculation model of off-axis magnetic field of tilted coil loop

The magnetic field at *p* point can be calculated by off-axis magnetic field method, one coil loop is applied with current *I* along anticlockwise, *Z* is the axis of the loop, *Y* axis is perpendicular to the paper out, *X* axis is decided by right-hand rule. Radius of the loop is *a*, *p(r, 0, z)* point can be expressed by cylindrical coordinates, *r* is the distance from *p* to *Z* axis, *z* is the height between *p* and *X* axis, angular coordinate ϕ of *p* point is *0*, *dl* is micro segment of the loop, it can be divided into the vertical and the horizontal component (dl_x, dl_y), *b* is the vertical distance from *dl* to *X* axis, ϕ' is the angle between *X* axis and *(O, dl)*. θ is the angle between *Z* axis and the horizontal, and it is also equal to tilt-angle α.

Magnetic flux density *B* can be induced by

$$B = \nabla \times A \tag{4.1}$$

Magnetic vector potential *A* generated by *dl* can be expressed as:

$$\vec{A} = \frac{\mu_0 I}{4\pi} \int \frac{\overrightarrow{dl}}{s} \tag{4.2}$$

Where μ_0 is the permeability of vacuum, the applied current *I*, and *s* is the distance between *p* point and *dl*. According to the cosine law, *b* can be expressed as:

$$b^2 = r^2 + a^2 - 2ra\cos\phi' \tag{4.3}$$

According to the Pythagorean theorem，

$$s^2 = b^2 + z^2 \tag{4.4}$$

Let us substitute equation (4.4) into equation (4.3),

$$s^2 = r^2 + z^2 + a^2 - 2ra\cos\phi' \tag{4.5}$$

The segment of the loop can be written as:

$$\overrightarrow{dl} = ad\phi'\hat{e}_{\phi'}, \;\; \hat{e}_{\phi'} = -i\sin\phi' + j\cos\phi' \tag{4.6}$$

Let us substitute equation (4.5) and equation (4.6) into equation (4.2), Magnetic vector potential A can be expressed as:

$$\underset{\phi=0}{\overrightarrow{A}} = \frac{\mu_0 I}{4\pi}\int_0^{2\pi} \frac{a\left(-i\sin\phi' + j\cos\phi'\right)d\phi'}{\sqrt{r^2 + z^2 + a^2 - 2ra\cos\phi'}} = \underset{\phi=0}{\overrightarrow{A_i}}i + \underset{\phi=0}{\overrightarrow{A_j}}j \tag{4.7}$$

Firstly, we calculate $\underset{\phi=0}{\overrightarrow{A_i}}i$, let

$$f\left(\phi'\right) = \sqrt{r^2 + z^2 + a^2 - 2ra\cos\phi'} \tag{4.8}$$

Taking the derivative of $f\left(\phi'\right)$ with respect to ϕ', we will get

$$\frac{df}{d\phi'} = \frac{ra\sin\phi'}{\sqrt{r^2 + z^2 + a^2 - 2ra\cos\phi'}} \tag{4.9}$$

As seen from equation (4.7), we will get

$$\underset{\phi=0}{\overrightarrow{A_i}} = -\frac{\mu_0 I}{4\pi r}\int_0^{2\pi} \frac{ra\sin\phi' d\phi'}{\sqrt{r^2 + z^2 + a^2 - 2ra\cos\phi'}} \tag{4.10}$$

Let equation (4.9) substitute into equation (4.10), we will get

$$\overrightarrow{A_i}_{\phi=0} = -\frac{\mu_0 I}{4\pi r}\int_0^{2\pi}\frac{df}{d\phi'}d\phi' \tag{4.11}$$

Integrating of ϕ' , we will obtain

$$\overrightarrow{A_i}_{\phi=0} = -\frac{\mu_0 I}{4\pi r}\left[\sqrt{r^2+z^2+a^2-2ra\cos\phi'}\right]_0^{2\pi},\ \overrightarrow{A_i}_{\phi=0} = 0 \tag{4.12}$$

Next we will calculate $\overrightarrow{A_j}_{\phi=0}$

$$\overrightarrow{A_j}_{\phi=0} = \frac{\mu_0 I}{4\pi}\int_0^{2\pi}\frac{a\cos\phi\ d\phi}{\sqrt{r^2+z^2+a^2-2ra\cos\phi'}} \tag{4.13}$$

Let

$$\phi' = \pi - 2\theta' \tag{4.14}$$

Taking the derivative of ϕ' with respect to θ'

$$\frac{d\phi'}{d\theta'} = -2,\ d\phi' = -2d\theta' \tag{4.15}$$

And we will get

$$\cos\phi' = 2\sin^2\theta' - 1 \tag{4.16}$$

And we substitute equation (4.15) and equation (4.16) into equation (4.13), we will get

$$\overrightarrow{A_j}_{\phi=0} = \frac{\mu_0 Ia}{2\pi}\int_{-\frac{\pi}{2}}^{\frac{\pi}{2}} \frac{(1-2\sin^2\theta')\,d\theta'}{\sqrt{r^2+z^2+a^2+2ra-4ra\sin^2\theta'}} \tag{4.17}$$

As the integral is even function, equation (4.17) can be written as

$$\overrightarrow{A_j}_{\phi=0} = \frac{\mu_0 Ia}{\pi\sqrt{z^2+(a+r)^2}}\int_0^{\frac{\pi}{2}} \frac{(2\sin^2\theta'-1)\,d\theta'}{\sqrt{1-(4ra\sin^2\theta')(z^2+(a+r)^2)^{-1}}} \tag{4.18}$$

Let

$$k^2 = \frac{4ra}{z^2+\left(a+r\right)^2} \tag{4.19}$$

Substituting k^2 into equation (4.18), we will get

$$\overrightarrow{A_j}_{\phi=0} = \frac{\mu_0 Ik}{2\pi}\sqrt{\frac{a}{r}}\int_0^{\frac{\pi}{2}} \frac{(2\sin^2\theta'-1)\,d\theta'}{\sqrt{1-k^2\sin^2\theta'}} \tag{4.20}$$

Let

$$\lambda = \frac{\mu_0 Ik}{2\pi}\sqrt{\frac{a}{r}} \tag{4.21}$$

By substitution, equation (4.20) can be written as

$$\overrightarrow{A_j}_{\phi=0} = \lambda \int_0^{\frac{\pi}{2}} \frac{(2\sin^2\theta' - 1)d\theta'}{\sqrt{1-k^2\sin^2\theta'}} \tag{4.22}$$

We will get

$$\overrightarrow{A_j}_{\phi=0} = \frac{2\lambda}{k^2}\int_0^{\frac{\pi}{2}}\left(\frac{1}{\sqrt{1-k^2\sin^2\theta'}} - \sqrt{1-k^2\sin^2\theta'}\right)d\theta' - \lambda\int_0^{\frac{\pi}{2}}\frac{d\theta'}{\sqrt{1-k^2\sin^2\theta'}} \tag{4.23}$$

Let $E_1(k)$ & $E_2(k)$ complete elliptic integrals of the first & second kinds respectively, we will get

$$\overrightarrow{A_j}_{\phi=0} = \frac{2\lambda}{k^2}(E_1(k) - E_2(k)) - \lambda E_1(k) \tag{4.24}$$

Substituting λ into equation (4.24), we will get

$$\overrightarrow{A_j}_{\phi=0} = \frac{\mu_0 I}{k\pi}\sqrt{\frac{a}{r}}E_1(k) - \frac{\mu_0 I}{k\pi}\sqrt{\frac{a}{r}}E_2(k) - \frac{\mu_0 Ik}{2\pi}\sqrt{\frac{a}{r}}E_1(k) \tag{4.25}$$

So equation (4.25) can be expressed as

$$\overrightarrow{A}_{\phi=0} = \left(\frac{\mu_0 I}{k\pi}\sqrt{\frac{a}{r}}E_1(k) - \frac{\mu_0 I}{k\pi}\sqrt{\frac{a}{r}}E_2(k) - \frac{\mu_0 Ik}{2\pi}\sqrt{\frac{a}{r}}E_1(k)\right)j \tag{4.26}$$

When $\phi = 0$, $\hat{e}_\phi = j$, equation (4.26) can be written as

$$\overrightarrow{A}_{\phi=0} = \left(\frac{\mu_0 I}{k\pi}\sqrt{\frac{a}{r}}E_1(k) - \frac{\mu_0 I}{k\pi}\sqrt{\frac{a}{r}}E_2(k) - \frac{\mu_0 I}{2\pi}\sqrt{\frac{k}{r}}aE_1(k)\right)\hat{e}_\phi \tag{4.27}$$

Due to the axial symmetry of the problem, this solution is valid for all values ϕ,

when $\frac{\mu_0 I\sqrt{a}}{2\pi}$ is put forward, we will get

$$\underset{\phi=0}{\overrightarrow{A}} = \frac{\mu_0 I\sqrt{a}}{2\pi}(2k^{-1}r^{-1/2}E_1(k) - 2k^{-1}r^{-1/2}E_2(k) - kr^{-1/2}E_1(k))\hat{e}_\phi \tag{4.28}$$

In cylindrical coordinates, B can be written as

$$B = \nabla \times A = \frac{1}{r}\begin{pmatrix} \hat{e}_r & r\hat{e}_\phi & \hat{e}_z \\ \frac{\partial}{\partial r} & \frac{\partial}{\partial \phi} & \frac{\partial}{\partial z} \\ A_r & rA_\phi & A_z \end{pmatrix} \tag{4.29}$$

As A_r and A_z are equal to 0, we will get

$$B = \frac{1}{r}\frac{\partial(rA_\phi)}{\partial r}\hat{e}_z - \frac{1}{r}(\frac{\partial(rA_\phi)}{\partial z})\hat{e}_r = B_z\hat{e}_z + B_r\hat{e}_r \tag{4.30}$$

The following relations are need to calculate B_z and B_r

$$\frac{dE_1(k)}{dk} = \frac{E_2(k)}{k(1-k^2)} - \frac{E_1(k)}{k} \tag{4.31a}$$

$$\frac{dE_2(k)}{dk} = \frac{E_2(k) - E_1(k)}{k} \tag{4.31b}$$

$$\frac{\partial k(z,r)}{\partial z} = \frac{-zk^3}{4ra} \tag{4.31c}$$

$$\frac{\partial k(z,r)}{\partial r} = \frac{k^3 (z^2 + r^2 - a^2)}{8 r^2 a} \tag{4.31d}$$

B_z and B_r can be rewritten as:

$$B_z = \frac{\mu_0 I}{2\pi\sqrt{z^2 + (a+r)^2}} \left(\frac{a^2 - z^2 - r^2}{z^2 + (r-a)^2} E_2(k) + E_1(k) \right) \tag{4.32a}$$

$$B_r = \frac{\mu_0 z I}{2\pi r\sqrt{z^2 + (a+r)^2}} \left(\frac{a^2 + z^2 + r^2}{z^2 + (r-a)^2} E_2(k) - E_1(k) \right) \tag{4.32b}$$

4.2 Numerical Analysis

4.2.1 Numerical Analysis of one loop

Actually, the magnet is actuated by vertical component of tilted magnetic field, so magnitude of the vertical components at *p* should be discussed. A software maximum is employed for calculating magnetic field due to the complexity of equations. Maxima is a full-featured CAS (computer algebra system) that specializes in symbolic operations but it also offers numerical capabilities such as arbitrary-precision arithmetic: integers and rational numbers which can grow to sizes limited only by machine memory, and floating point numbers whose precision can be set arbitrarily large.

Next, the magnetic field mentioned this chapter means the vertical component of tilted magnetic field at *P*. To clarify the change of magnetic field, magnetic field has been calculated by Maxima with varying parameters of one loop such as radius,

tilt-angle and supplied current, firstly, we assume that the distance between *P* and the center of tilted loop *O* is 1.5mm, *z* and *r* can be calculated for $1.5\cos\theta$ and $1.5\sin\theta$ respectively, where θ is the angle between *Z* axis and horizontal direction, α is the tilt-angle of loop and is equal to θ, so when the tilt-angles of loop are 30°, 45° and 60° respectively, we can obtain θ for 30°, 45° and 60°. And the magnetic field was calculated with varying radius of loop ranges from 0.5mm to 1.5mm at three different tilt-angles, as shown in Fig.4-2.

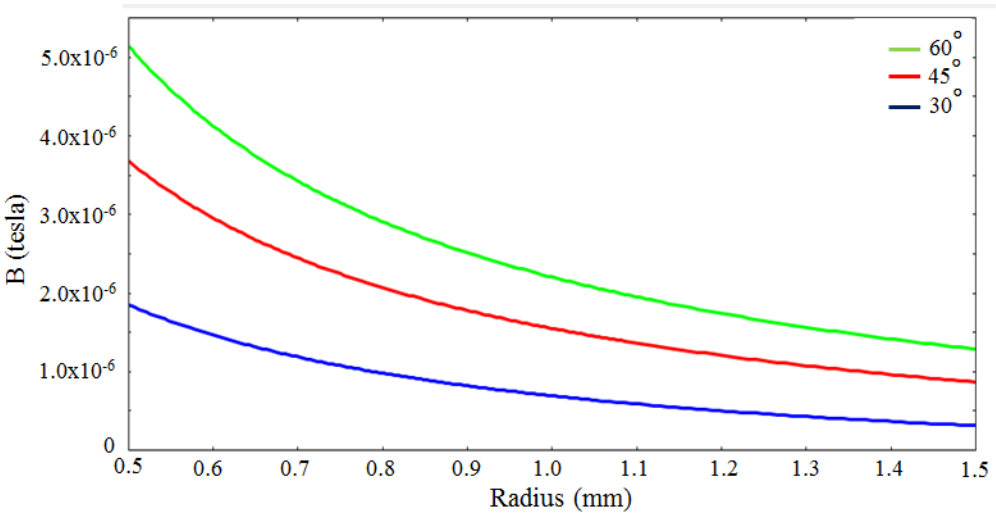

Fig.4-2 Calculated magnetic field with different radius of loop from 0.5mm to 1.5mm at tilt-angle of 30°, 45° and 60° respectively.

The magnetic field was also calculated with different radius and distances of *OP*. the tilt-angle is designated as 60° and the distance *OP* is decided from 1.5mm to 0, The calculated result is shown Fig.4-3.

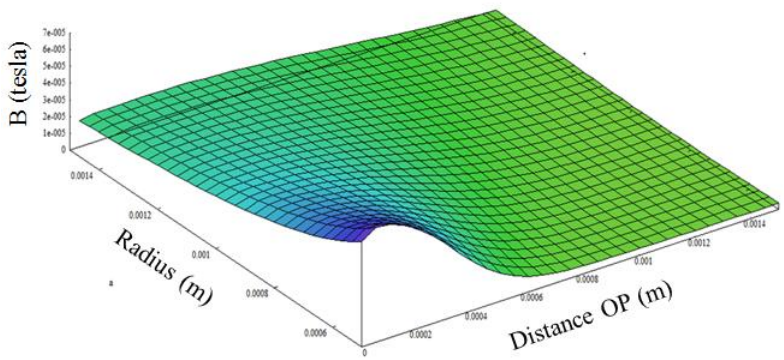

Fig.4-3 Calculated magnetic field with different radius and distance *OP*.

There is a peak value at three dimensional net diagram, the value of magnetic field increases dramatically, especially for the smaller radius, there are sharp upward before the distance *Op* 0.8mm, and a gentle upward trend is demonstrated after it. It indicates that the magnetic field intensity is gradually decreasing *Op*.

4.2.2 Numerical Analysis of two loops

What have been discussed above are all about a coil loop, and the parameters involved with radius, tilt-angle and distance *OP*, however, coil pitch and coil turns also should be discussed, thus, we assumed that two tilted loops were seen as two turns tilted coil, as shown in Fig.4-4.

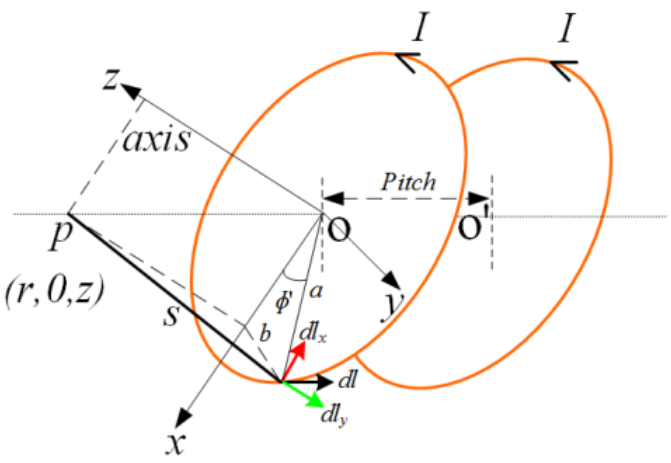

Fig.4-4 Calculation model of off-axis magnetic field of two and more tilted coil loops

As we can see from the calculation model, the most of the parameters are as the same as the one loop model but pitch, as decisive parameter, which is decided by fabrication ability, it can be designed from 80 μm to 400 μm. And the two tilted loops were supplied with same current *I* for 50 mA, coil pitch is defined for the distance between center O and center O′, the magnetic field can be obtained by superposition value generated by the first and the second loop.

The magnetic field was calculated with different pitch ranges from 50μm to 400μm, as shown in Fig.4-5. The radius is 1mm, and tilt-angle is 60°. It indicates that magnetic field decrease with increasing pitch. There is drastic down trend with growing pitch. It is proved that the coil pitch is decisive parameter for designed coil.

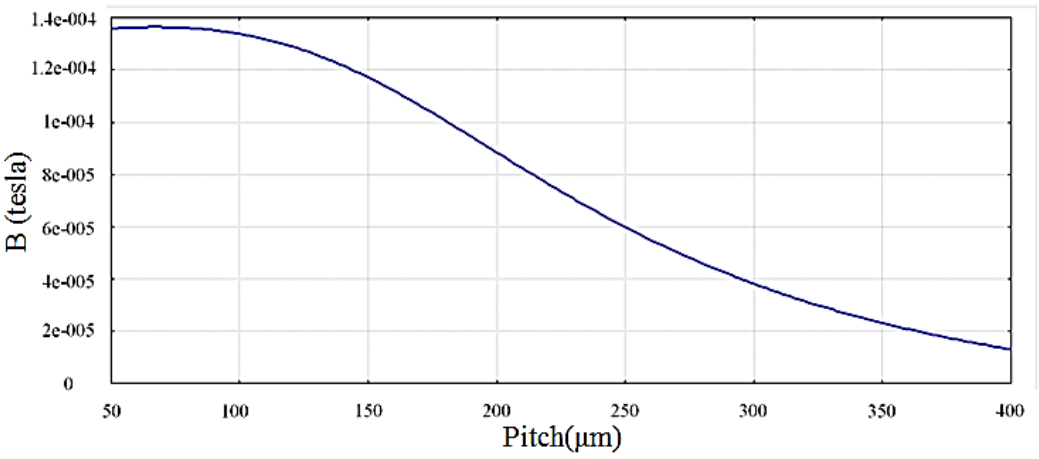

Fig.4-5 Calculated magnetic field by different pitch at tilt-angle of 60°

The magnetic field was also calculated by different turns, as shown in Fig.4-6.

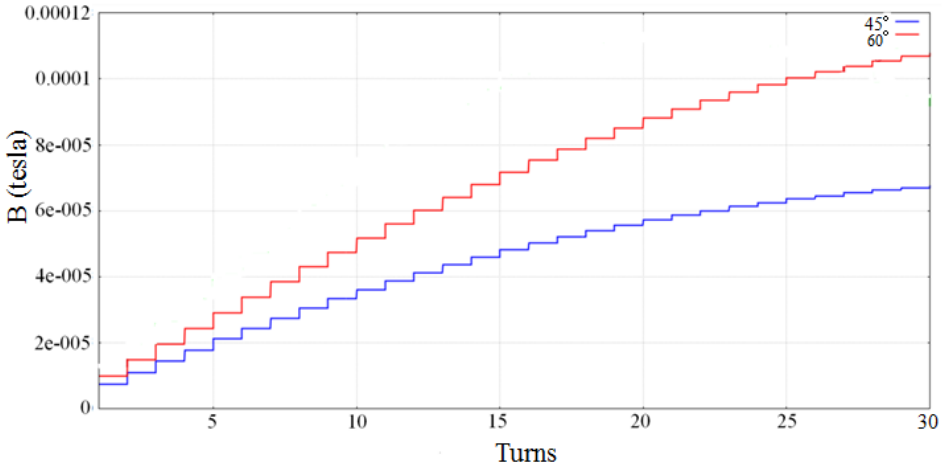

Fig.4-6 Calculated magnetic field by different turns for tilt-angle of 60° and 45°

As we can see from the calculated results, external magnetic field of tilted coil can be affected by many factors such as radius, tilt-angle, supplied current, pitch and turns. This phenomenon is also occurring at simulated result of magnetic force mentioned above, among these factors, tilt-angle, pitch and turns are confined by fabrication method, in this research, the designed parameter of coil has been decided

through simulated and calculated result. The largest magnetic force on magnet and external magnetic field were gained at reduced pitch, but the designed pitch was designated for 80μm due to the limitation of fabrication ability. Tilt-angle was decided for 60°, and turns can be chosen for 20 or 30. The radius of tilted coil was designed as 0.5mm, on the one hand, larger external magnetic field can be generated by it, and on the other hand, it can make a contribution to shrink the overall size of fiber scanner. In conclusions, the radius, the tilt-angle, and pitch are designed for 0.5mm, 60° and 80μm respectively.

4.3 Summary

The analysis of off-axis magnetic field of tilted coil has been discussed in this chapter. Firstly, a charged tilted loop has been calculated based on the deduced equation of off-axis magnetic field, the magnet field was obtained with increasing radius for 30° 45° 60° tilt-angle respectively, it was also calculated with different distance *Op*, it indicates that the magnetic field is decreasing with increasing radius.

Secondly, in order to study on effect of pitch and turns, more than one charged tilted loop has been discussed. The centers of two tilted loop are O and O′, pitch is the distance between these two centers. The magnetic field has been calculated with varying pitch and turns. It is proved that large magnetic field is generated with decreased pitch and increased turns. However, turns is increased more than 20, a slight upward is demonstrated, which is consistent with results from Fig.3-6

5. MECHANICAL ANALYSIS

5.1 Structure with one lumped mass

The fiber scanner has its own resonance frequency and it performs larger amplitude under resonance frequency actuation. To find the resonant frequency of the fiber scanner, modal analysis has been conducted by employing commercial ANSYS finite element analysis (FEA) software. And it was chosen because complex geometry can be offered easily and be provided efficient analysis of static and dynamic behavior. Some important modeling assumptions include axial symmetry of the scanning fibers, homogeneous and isotropic material properties of the fiber and linear dynamic behavior of the scanning fiber system, the resonant frequency and fiber tip displacement can be simulated, and the equation of motion for the simulated model can be expressed as:

$$\boldsymbol{M}\frac{\partial \boldsymbol{x}}{\partial t^2}+\boldsymbol{C}\frac{\partial \boldsymbol{x}}{\partial t}+\boldsymbol{Ku}=\boldsymbol{F} \tag{5.1}$$

In this vibration equation, where M is the structural mass matrix , C is the damping matrix, K is the stiffness matrix, and F is applied loading, in this work, the resonant frequency and fiber tip displacement has been simulated without considering damping. The vibration equation can be rewritten as: Table.5-1 shows the geometrical parameters and specifications of the fiber scanner modal.

$$\boldsymbol{M}\frac{\partial \boldsymbol{x}}{\partial t^2}+\boldsymbol{Ku}=\boldsymbol{F} \tag{5.2}$$

Table.5-1 Geometric parameters and material property of fiber scanner modal.

Component	Geometric parameters and material property	Value
Optical fiber	Elastic Modulus E_f	1.72 GPa
	Poisson ratio R_f	0.17
	Density ρ_f	2200 Kg/m^2
	Length F_1, F_2, F_3	$F_1+F_2+F_3$=13mm
	Diameter D_f	125μm
Magnet	Elastic Modulus E_m	210 GPa
	Poisson ratio R_m	0.31
	Density ρ_m	8500 Kg/m^2
	Length M_1	M_1= F_2=2mm
	Diameter D_m	600μm
Lens	Elastic Modulus E_l	1.72 GPa
	Poisson ratio R_l	0.17
	Density ρ_l	2200 Kg/m^2
	Length L_1	1mm
	Diameter D_l	0.5mm

ANSYS was employed to construct FE model, The ANSYS program has a large library of element types. Some of the characteristics of the element types, and their groupings, ANSYS models may be either two-dimensional or three-dimensional depending upon the element types used. In this work, a three-dimensional fiber scanner model was built according to the geometric parameters and material property of every component, SOLID 45 element type was chosen, and the SWEEP method was used to mesh the model as shown in Fig.5-1 (a).

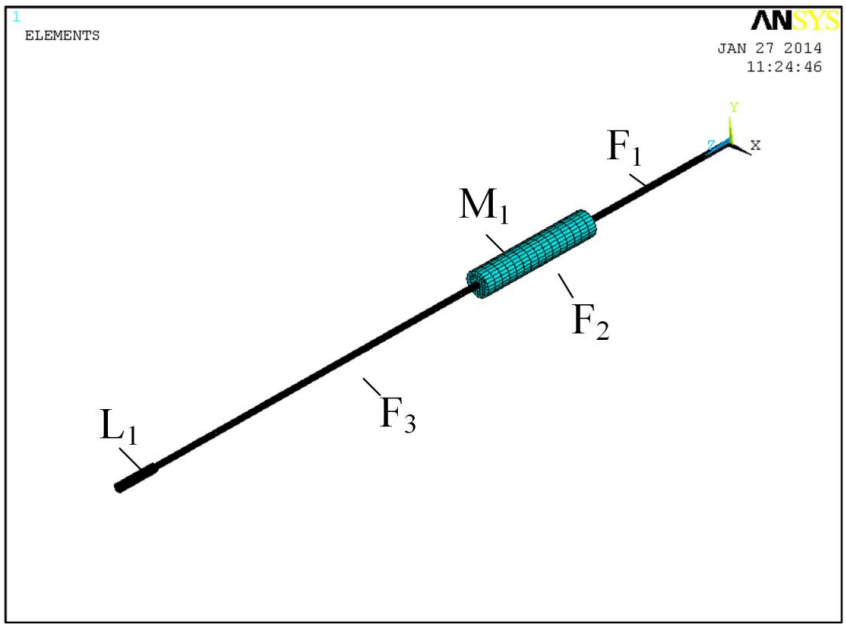

Fig.5-1 FEA models of fiber scanner

A very fine mesh is employed inevitably for obtaining results with high accuracy at high-order mode shapes and frequency, a linear isotropic material properties are endowed for elements during harmonic and transient analysis. The first two order resonant model shape and resonant frequency of the fiber scanner have been simulated and shown in Fig.5. In this model, F_1, F2, F_3 are 3mm, 2mm, 8mm respectively, displacement of fiber tip and resonant frequency will be simulated with varying F_1. Due to F_1+F_2+F_3 is constant 13mm and the length of F_2 is equal to 2mm the length of magnet, so F_3 is varying with different F_1.

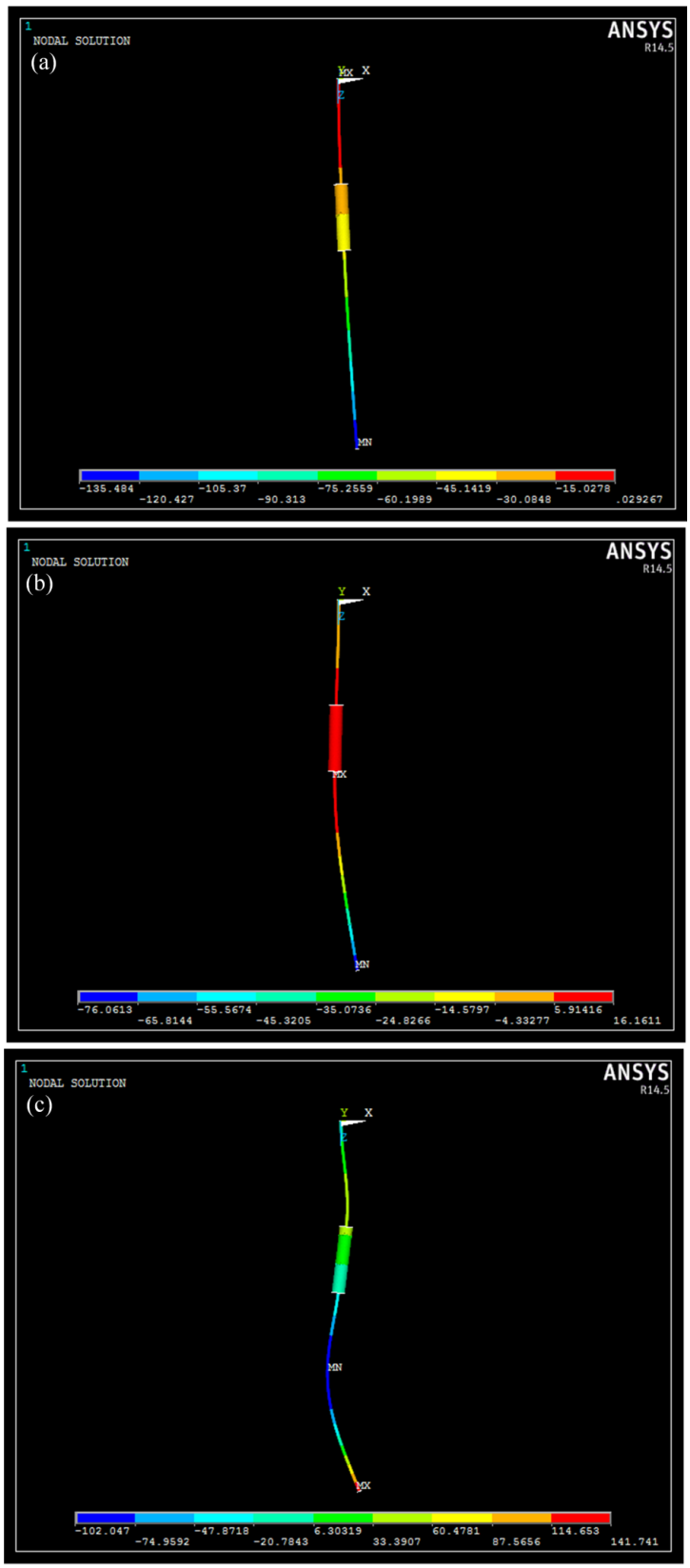

Fig.5-2 Presented structure deformation of the first three resonance models.

The first two order resonant frequency of fiber scanner models were simulated with different length of F_1, as shown in Fig.5-3.

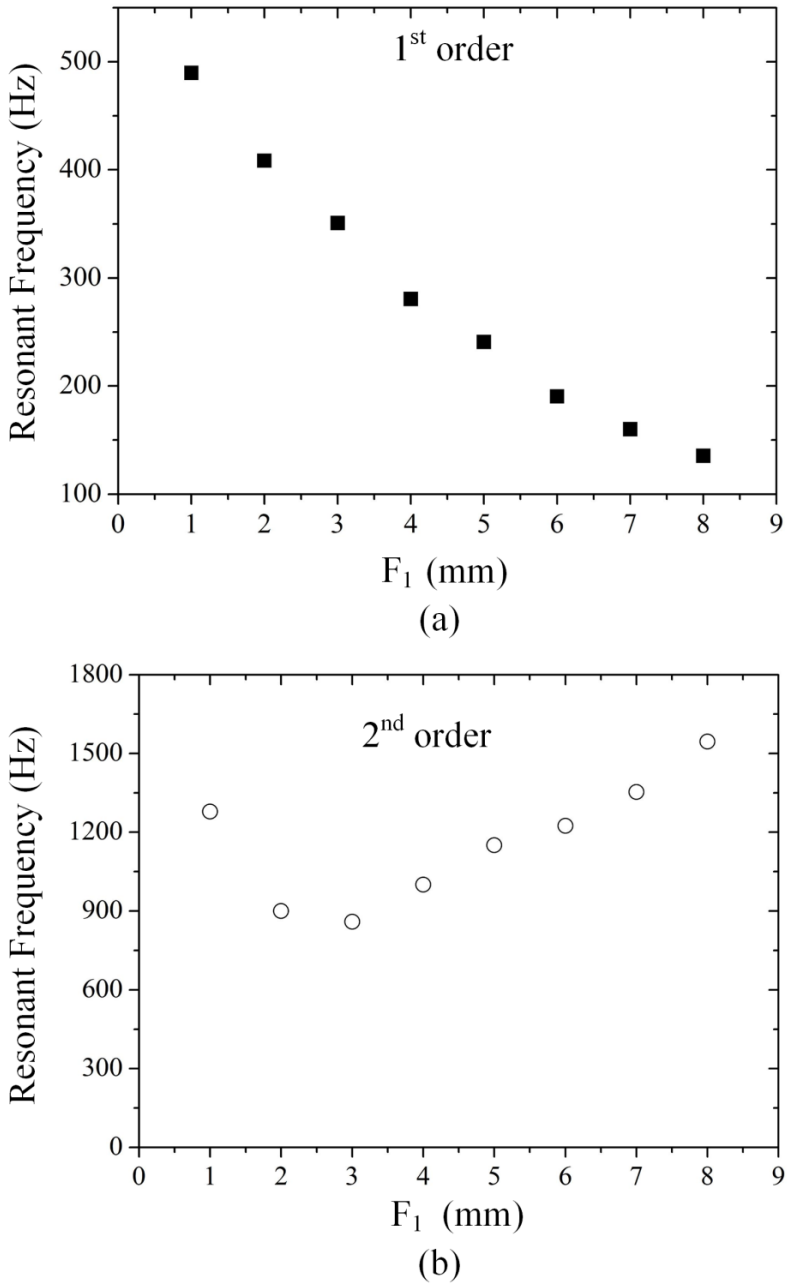

Fig.5-3 Simulated resonant frequency of fiber scanner with increasing F_1 at the first two order vibration: (a) the first-order vibration and (b) the second-order vibration.

It indicated that the first-order resonant frequency of fiber scanner gradually

decreases with increasing length of F_1, and it shows that the second-order resonant frequency decreases firstly, and then increase during the growth of the length of F_1. The displacement of fiber tip was simulated with ascending length of F_1 under driving force 10μN, as shown in Fig.5-4.

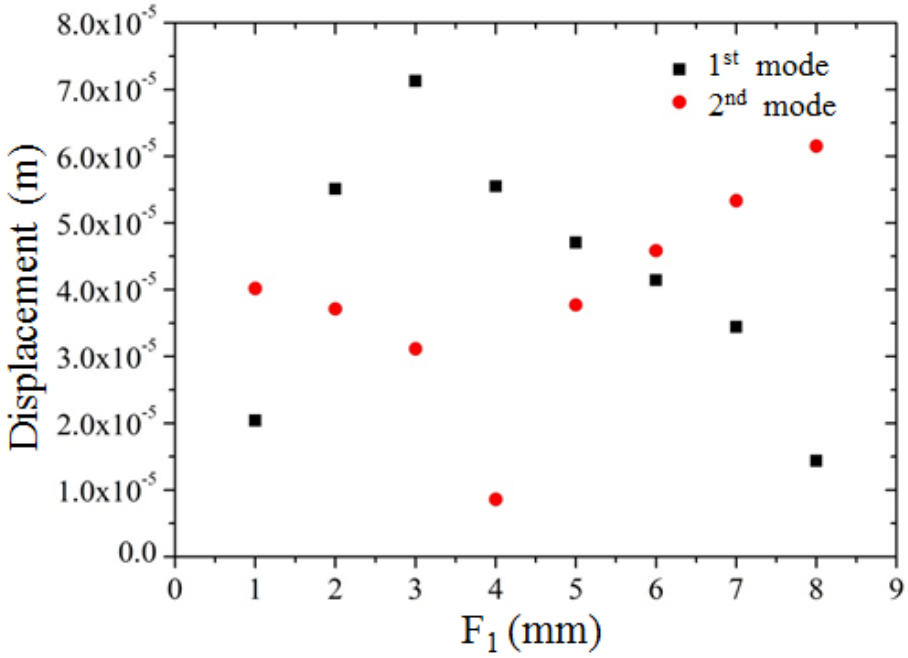

Fig.5-4 Simulated displacement of fiber tip with increasing F_1 at the first two order vibration under driving force of 10μN

It is proved that the largest displacement of fiber tip was demonstrated at F_1 for 3mm at first-order vibration mode, there are one top peak for the first-order vibration mode and low ebb for the second-order vibration mode. For fiber scanner application, scanning angle is main parameter for evaluating scanning function, and scanning angle cannot be obtained directly by simulation, but it can be calculated by simulation results, for example, we can gain displacement of output of every point

along fiber scanner, as shown in Fig.5-5. The scanning angle can be calculated using arc tangent function at linear part.

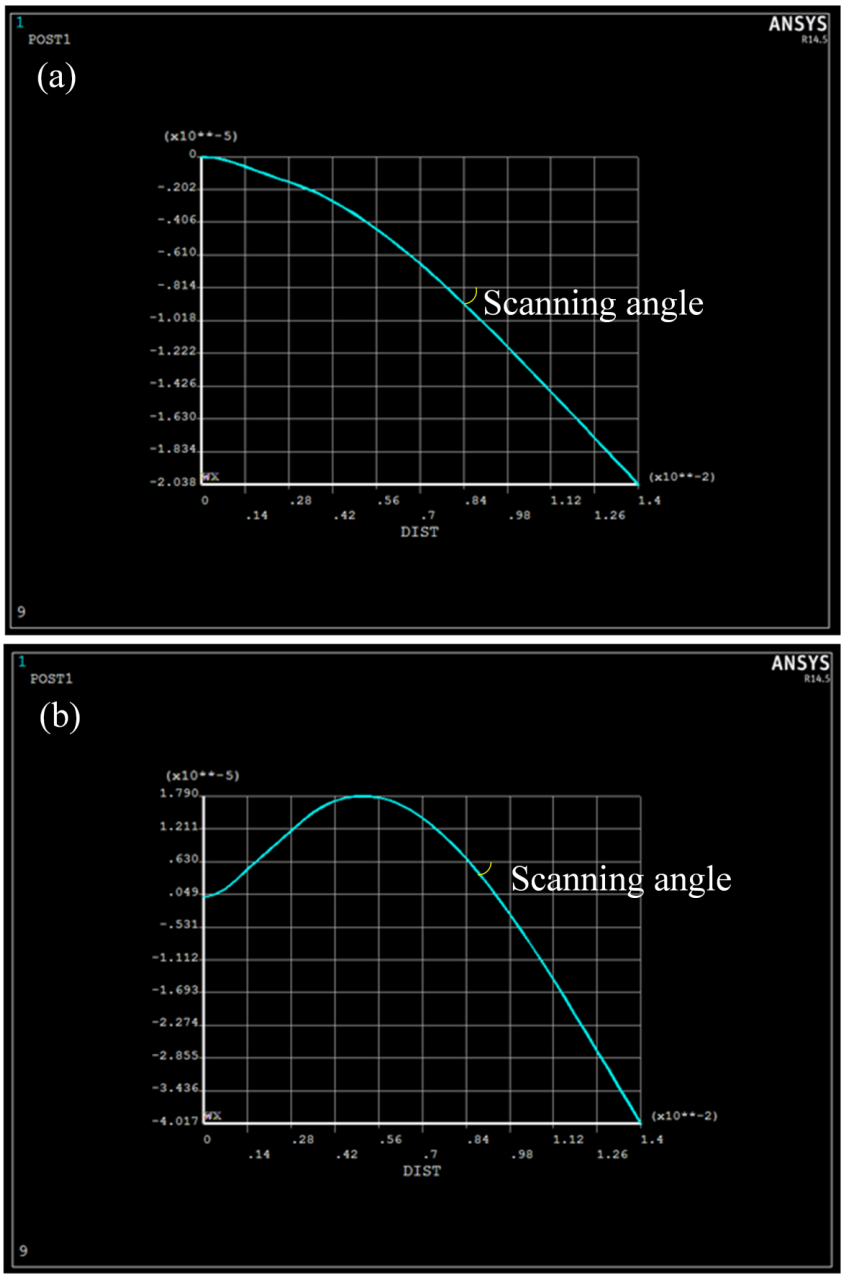

Fig.5-5 Simulated displacement of every point along fiber scanner at the first two order vibration (a) first-order vibration and (b) second-order vibration

Scanning angles were calculated with different F_1 at the first two order

vibration, as shown in Fig.5-6.

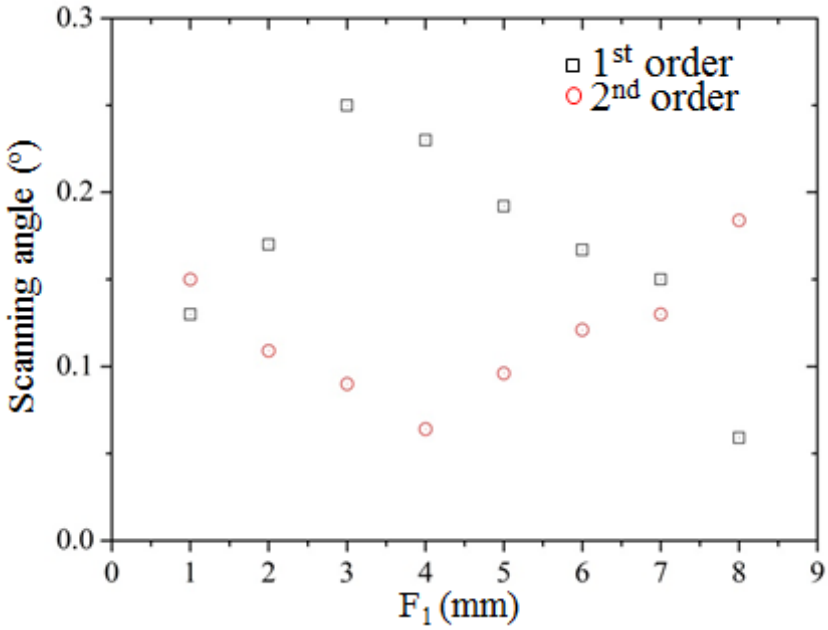

Fig.5-6 Calculated scanning angle with increasing F_1 at the first two order vibration.

It indicates that when F_1 is equal to 1mm or 8mm, scanning angle of second-order vibration is larger than the one of first-order vibration, obviously, in general, scanning angle of first-order vibration is larger than the one of second-order vibration. And the largest scanning angle was demonstrated at F_1 of 3mm under first-order vibration.

5.2 Structure with two lumped masses

Mechanical system with one or two degrees of freedom is a common issue in engineering, above mentioned designed fiber scanner can be seen as mechanical system with one degree of freedom, one optical fiber with magnet can be considered into beam-mass system, but it provides a small scanning angle. So the mechanical system should be improved, two degrees of freedom vibration system is proposed for

the fiber scanner, beam-two mass system. The advanced fiber scanner is shown in Fig.5-7. Comparing with original designed fiber scanner, only one lumped mass is added at fiber tip. It is made of nickel. This fiber scanner can be seen as two degrees of freedom vibration system. It also can be expressed for a cantilever beam with two masses.

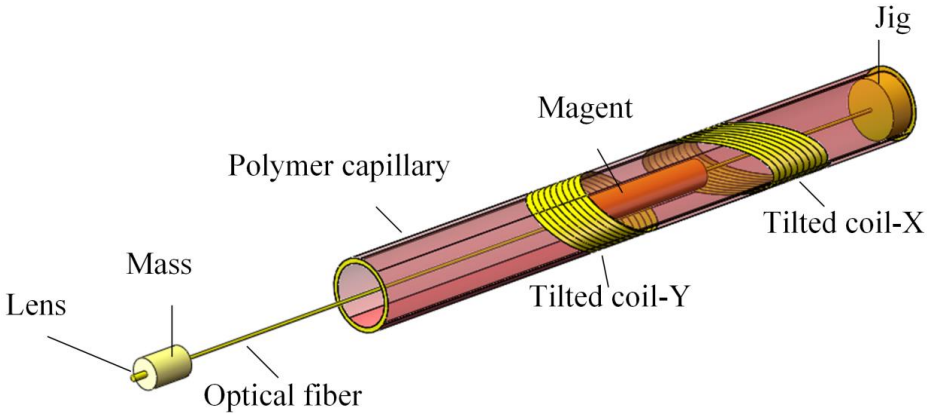

Fig.5-7 Improved fiber scanner with lumped mass at fiber tip

5.2.1 Theory of two degrees freedom system

The advanced designed fiber scanner can be expressed as model of cantilever with two masses as shown in Fig.5-8 (a). It can be deduced into two degrees of freedom vibration model as shown in Fig.5-8 (b), which consists of two bodies with mass m-1 and m-2, they are both fixed to a solid frame with a spring of spring constant *k* and a damper with damping coefficient *c*.

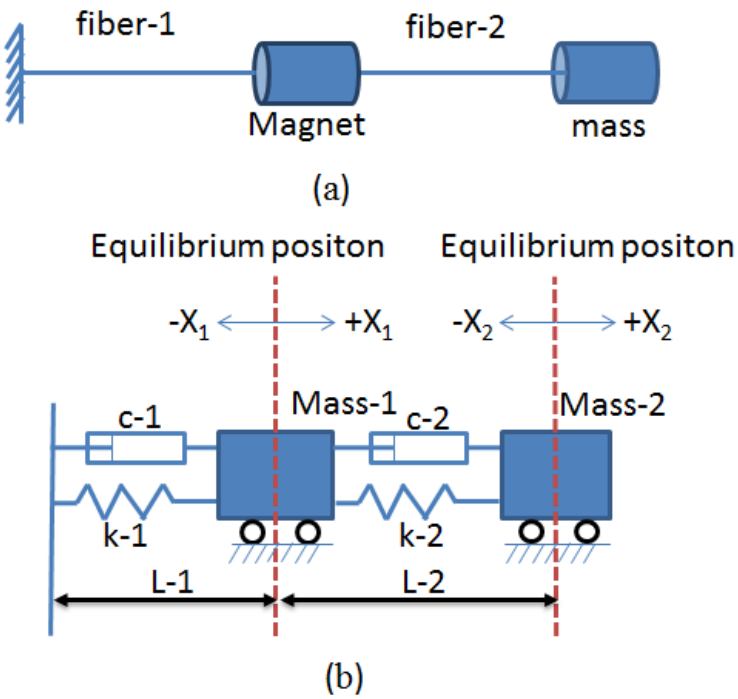

Fig.5-8 Two degrees of freedom system (a) designed fiber scanner model (b) vibration model

We will begin with the free vibration, and we will determine the natural frequency and mode shape of vibration. Using Newton's second law, we can write the equation of motion of vibration of each mass as follows:

$$m_1\ddot{x}_1 = c_2(\dot{x}_2 - \dot{x}_1) + k_2(x_2 - x_1) - k_1x_1 - c_1\dot{x}_1 \tag{5.3a}$$

$$m_2\ddot{x}_2 = -c_2(\dot{x}_2 - \dot{x}_1) - k_2(x_2 - x_1) \tag{5.3b}$$

Where m is the mass, c is the damping coefficient, k is spring constant, $\dot{x}$ is velocity of mass, $\ddot{x}$ is accelerated velocity of mass. Using matrix notation, we can rewrite it as follows:

$$\begin{bmatrix} m_1 & 0 \\ 0 & m_2 \end{bmatrix}\begin{bmatrix} \ddot{x}_1 \\ \ddot{x}_2 \end{bmatrix}+\begin{bmatrix} c_1+c_2 & -c_2 \\ -c_2 & c_2 \end{bmatrix}\begin{bmatrix} \dot{x}_1 \\ \dot{x}_2 \end{bmatrix}+\begin{bmatrix} k_1+k_2 & -k_2 \\ -k_2 & k_2 \end{bmatrix}\begin{bmatrix} x_1 \\ x_2 \end{bmatrix}=\begin{bmatrix} 0 \\ 0 \end{bmatrix} \tag{5.4}$$

Thus we have two coupled, second order ordinary differential equations of motion with constant coefficients. They are mass matrix, damping matrix, stiffness matrix. It can be simplified, when without regard to damping force. It can be expressed as:

$$\begin{bmatrix} m_1 & 0 \\ 0 & m_2 \end{bmatrix}\begin{bmatrix} \ddot{x}_1 \\ \ddot{x}_2 \end{bmatrix}+\begin{bmatrix} k_1+k_2 & -k_2 \\ -k_2 & k_2 \end{bmatrix}\begin{bmatrix} x_1 \\ x_2 \end{bmatrix}=\begin{bmatrix} 0 \\ 0 \end{bmatrix} \tag{5.5}$$

Considering the harmonic vibration, we let the solution as follows:

$$x_1(t)=x_1 \sin\omega t\,,\quad x_2(t)=x_2 \sin\omega t \tag{5.6}$$

Substituting (5.6) in equation (5.5), we get

$$-\omega^2\begin{bmatrix} m_1 & 0 \\ 0 & m_2 \end{bmatrix}\begin{bmatrix} x_1 \\ x_2 \end{bmatrix}+\begin{bmatrix} k_1+k_2 & -k_2 \\ -k_2 & k_2 \end{bmatrix}\begin{bmatrix} x_1 \\ x_2 \end{bmatrix}=\begin{bmatrix} 0 \\ 0 \end{bmatrix} \tag{5.7}$$

Re-write (5.7) as:

$$-\omega^2[m][x]+[k][x]=[0] \tag{5.8}$$

Where the ω is angular frequency rad/s, it also referred as angular speed, radial frequency and so on. $\omega=2\pi f$, f is the ordinary frequency Hz. For this model, stiffness matrix is unknown, and it is decided by spring constant of segment of fiber,

here it is easier to develop a flexibility matrix, and inverting flexibility matrix we get the stiffness matrix.

$$[k]=[a]^{-1} \tag{5.9}$$

The flexibility method, also called the method of consistent deformations or the method of superposition. Flexibility matrix can be obtained by this method. We assume flexibility matrix

$$[a]=\begin{bmatrix} a_{11} & a_{12} \\ a_{21} & a_{22} \end{bmatrix} \tag{5.10}$$

a_{ij} is the deflection at 'i' due to unit load at 'j' as shown in Fig.7-3

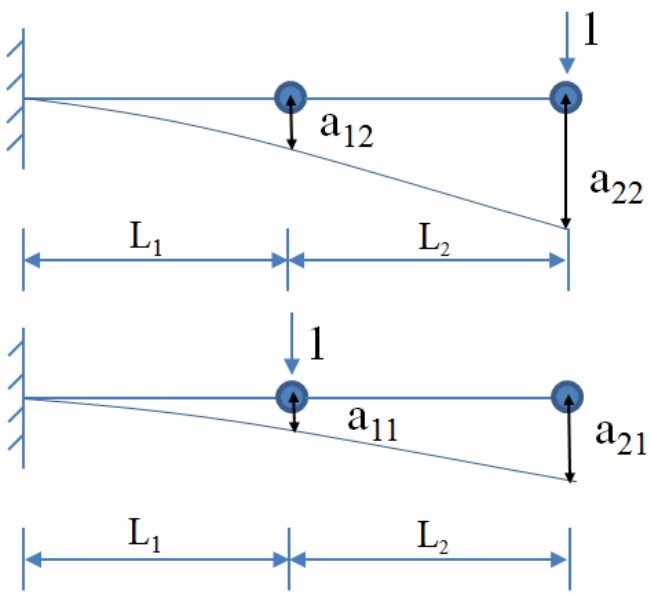

Fig.7-3 Flexibility coefficients

The flexibility coefficient can be calculated by

$$y = \frac{Fx^2}{6EI}(3a - x) \qquad (0 \le x \le a) \tag{5.11a}$$

$$y = \frac{Fa^2}{6EI}(3x - a) \qquad (a \le x \le L_f = L_1 + L_2) \tag{5.11b}$$

Where F is unit loading 1, a is distance between fixed end and loading point, x is deflection position distance, E is elasticity modulus and I is inertia moment. As we see from the flexibility method, L_1 and L_2 are critical parameters for calculation of flexibility coefficient, thus the location of magnet should be designed as shown in Fig.7-4. There are three models for discussion.

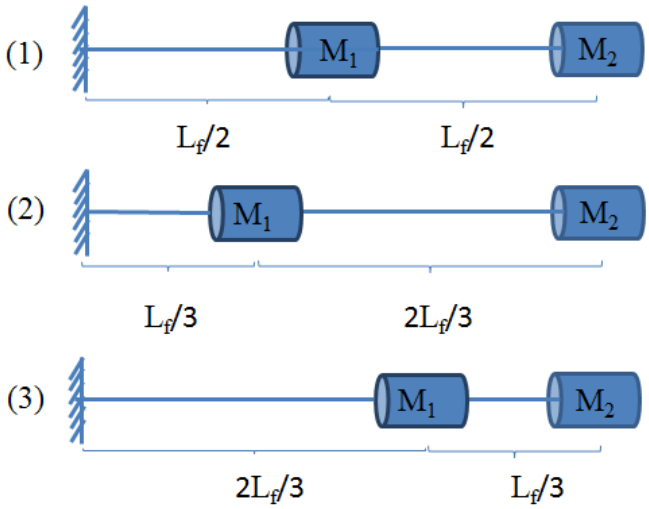

Fig.7-4 Three models with different location of magnet

At the beginning, we took the first model as calculation model, so when $L_1 = L_2 = L = L_f / 2$. the flexibility coefficient may be calculated as:

$$a_{11} = \frac{L^3}{3EI}; \quad a_{12} = a_{21} = \frac{L^3}{3EI} + \frac{L^3}{2EI} = \frac{5L^3}{6EI}; \quad a_{22} = \frac{8L^3}{3EI} \tag{5.12}$$

Hence the flexibility matrix is

$$[a]=\frac{L^3}{6EI}\begin{bmatrix}2 & 5\\ 5 & 16\end{bmatrix} \tag{5.13}$$

Equation (5.8) can be rewritten as:

$$\frac{1}{\omega^2}[x]=[k]^{-1}[m][x]=[a][m][x] \tag{5.14}$$

Let matrix $[\mathrm{a}]$ substitute into equation (5.14), we will get

$$\frac{1}{\omega^2}[x]=\frac{L^3}{6EI}\begin{bmatrix}2 & 5\\ 5 & 18\end{bmatrix}\begin{bmatrix}m_1 & 0\\ 0 & m_2\end{bmatrix}[x] \tag{5.15}$$

Here, two conditions are taken into consideration: (1) $m_1 = m_2 = m$ and (2) $m = m_1 \rangle m_2 = m/2$

Firstly, we will discuss the first condition $m_1 = m_2 = m$, let us substitute it into equation (5.15), we will get

$$\frac{1}{\omega^2}[x]=\frac{L^3 m}{6EI}\begin{bmatrix}2 & 5\\ 5 & 18\end{bmatrix}\begin{bmatrix}1 & 0\\ 0 & 1\end{bmatrix}[x] \tag{5.16}$$

Assume

$$\lambda=\frac{6EI}{L^3 m\omega^2} \tag{5.17}$$

We get

$$\begin{Vmatrix} 2-\lambda & 5 \\ 5 & 16-\lambda \end{Vmatrix} = 0 \tag{5.18}$$

The characteristic equation is

$$\lambda^2 - 18\lambda + 7 = 0 \tag{5.19}$$

Solving the above quadratic equation

$$\lambda_1 = 17.6023, \quad \lambda_2 = 0.3977 \tag{5.20}$$

We will get

$$\lambda_1 = 17.6023, \quad \omega_1 = 0.584\sqrt{\frac{EI}{mL^3}} \tag{5.21}$$

When *m* is equal to 0.005g, Substituting this in the matrix equation (5.20), we get fundamental mode shape as

$$x_1 = 1, \quad x_2 = 3.12 \tag{5.22}$$

Corresponding to second-order vibration

$$\lambda_2 = 0.3977, \quad \omega_2 = 3.88\sqrt{\frac{EI}{mL^3}} \tag{5.23}$$

We get second-order mode shape as

$$x_1 = 1, \quad x_2 = -3.08 \tag{5.24}$$

When $m = m_1 \rangle m_2 = m/2$, we will get

$$\lambda_1 = 19.27, \quad \omega_1 = 0.558\sqrt{\frac{EI}{mL^3}} \tag{5.25a}$$

$$\lambda_2 = 0.7265, \quad \omega_2 = 2.873\sqrt{\frac{EI}{mL^3}} \tag{5.25b}$$

The first two order mode shape can be calculated for

First-order: $x_1 = 1, \quad x_2 = 3.085$ (5.26a)

Second-order: $x_1 = 1, \quad x_2 = -0.654$ (5.26b)

The resonant frequency and mode shape of above-mentioned two structures are shown in Fig.7-5.

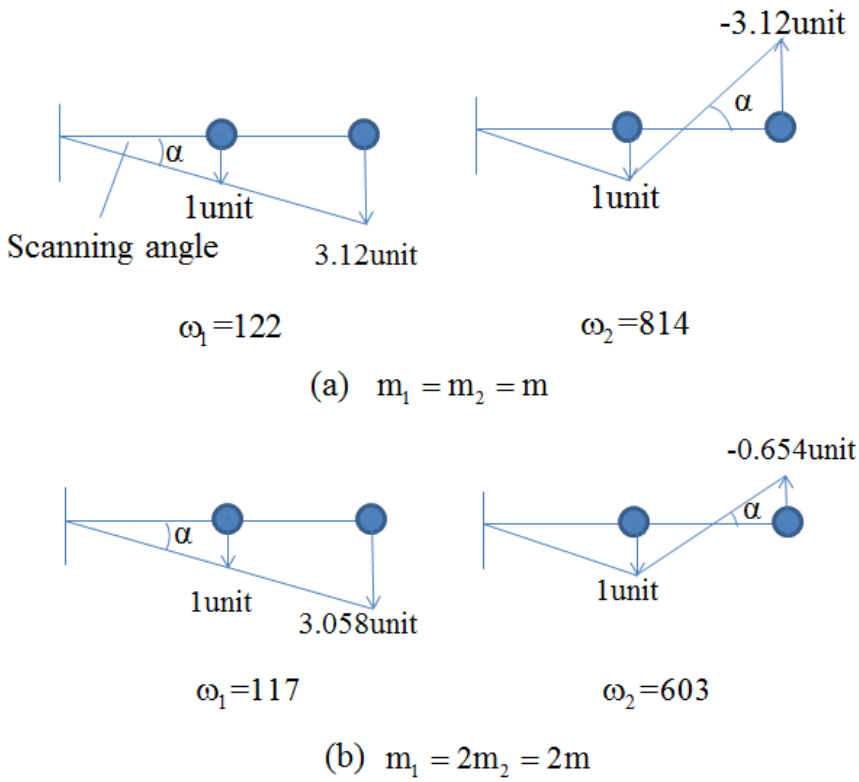

Fig.7-5 Mode shapes and the first two resonant frequency: (a) $m_1=m_2=m$, (b) $m_1=2m_2=2m$

It indicates that when the lumped mass is equal to the mass of magnet, the identical fiber tip displacement for the first two resonant modal are demonstrated, but large scanning angle is shown at the second-order resonant mode. When the lumped mass is the half to the mass of magnet, large fiber tip displacement and scanning angle both are obtained at the first-order resonant mode.

After analyzing the natural vibration of two degrees of freedom for fiber scanner, forced vibration of fiber scanner should be taken into consideration, and exciting force is produced on the magnet or mass one as shown in Fig.7-6. As previous analysis, the exciting force accords with distribution of sine function.

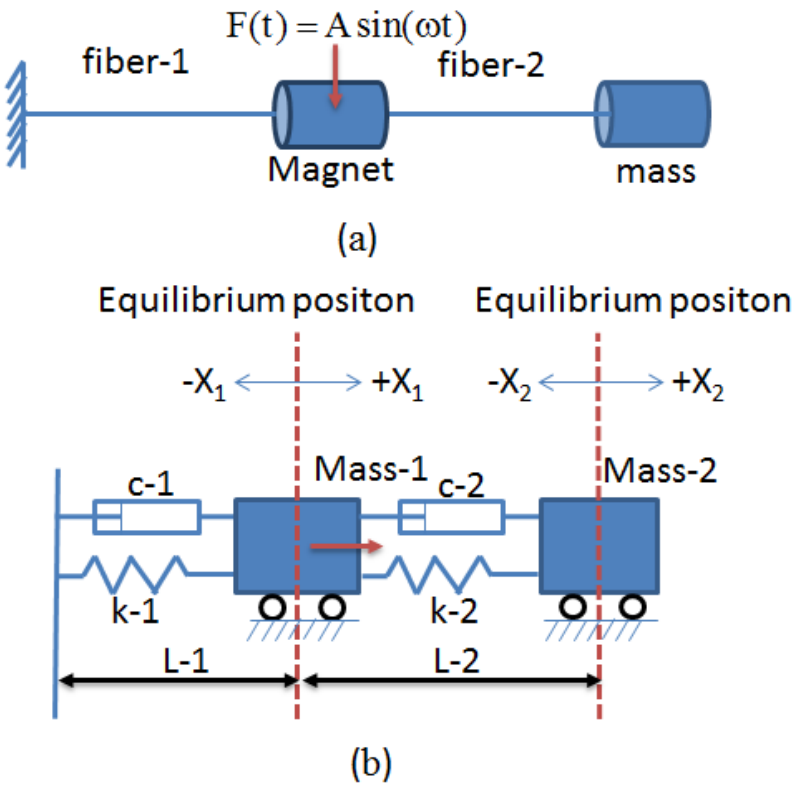

Fig.7-6 Forced vibration of two degrees of freedom system (a) designed fiber scanner model and (b) vibration model

Using matrix notation, we can write equation of forced vibration as following:

$$\begin{bmatrix} m_1 & 0 \\ 0 & m_2 \end{bmatrix}\begin{bmatrix} \ddot{x}_1 \\ \ddot{x}_2 \end{bmatrix}+\begin{bmatrix} c_1+c_2 & -c_2 \\ -c_2 & c_2 \end{bmatrix}\begin{bmatrix} \dot{x}_1 \\ \dot{x}_2 \end{bmatrix}+\begin{bmatrix} k_1+k_2 & -k_2 \\ -k_2 & k_2 \end{bmatrix}\begin{bmatrix} x_1 \\ x_2 \end{bmatrix}=\begin{bmatrix} f(t) \\ 0 \end{bmatrix} \tag{5.27}$$

5.2.2 Numerical Analysis of two degrees freedom system

The displacement of m_1 and m_2 can be calculated according to the equation of the forced vibration. The Matlab/Simulink was employed for calculation due to the complexity of the equation. In Simulink, it is very straightforward to represent and then simulate a mathematical model representing a physical system. Models are

represented graphically in Simulink as block diagrams. Wide arrays of blocks are available to the user in provided libraries for representing various phenomena and models in a range of formats. One of the primary advantages of employing Simulink (and simulation in general) for the analysis of dynamic systems is that it allows us to quickly analyze the response of complicated systems that may be prohibitively difficult to analyze analytically. Simulink is able to numerically approximate the solutions to mathematical models which are difficult to calculate by hand. The equation can be expressed by block diagrams as shown in Fig.7-7

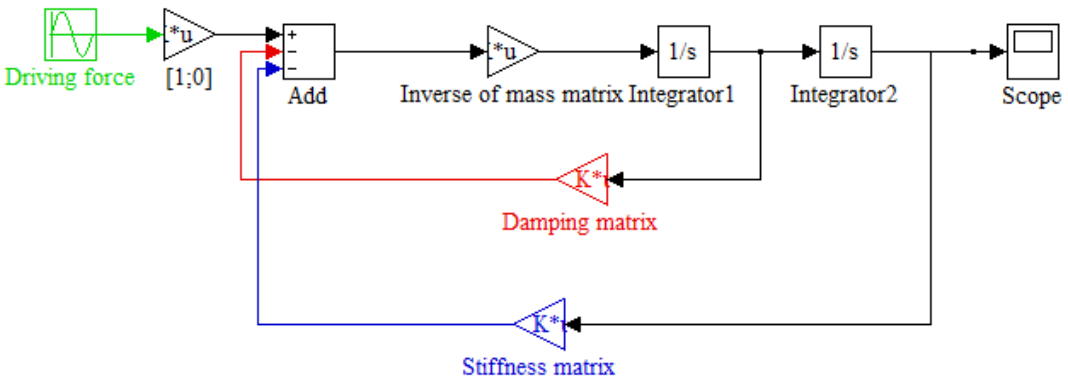

Fig.7-7 Block diagram of fiber scanner with two degrees of freedom in Simulink

In this block diagram, amplitude of driving force is provide as 10μN, and the frequency of driving force can be designated as variable. The function of add block realizes the addition and subtraction, driving force matrix minus damp force matrix and spring force matrix, and will be multiplied by the inverse of mass matrix, next carrying out two integrations, the displacement of m_1 and m_2 will be obtained and shown in the scope. Firstly, we took $m_1=m_2=m$ model as example and calculated displacement of m_1 and m_2 at different driving frequency as follows: (a) $\omega_{11}=10$;

(b) $\omega_{12}=200$; (c) $\omega_{13}=100$; (d) $\omega_{14}=120$, the result of forced vibration without damping force is shown in Fig.7-8. The red line and blue line are displacement of m_1 and m_2 respectively.

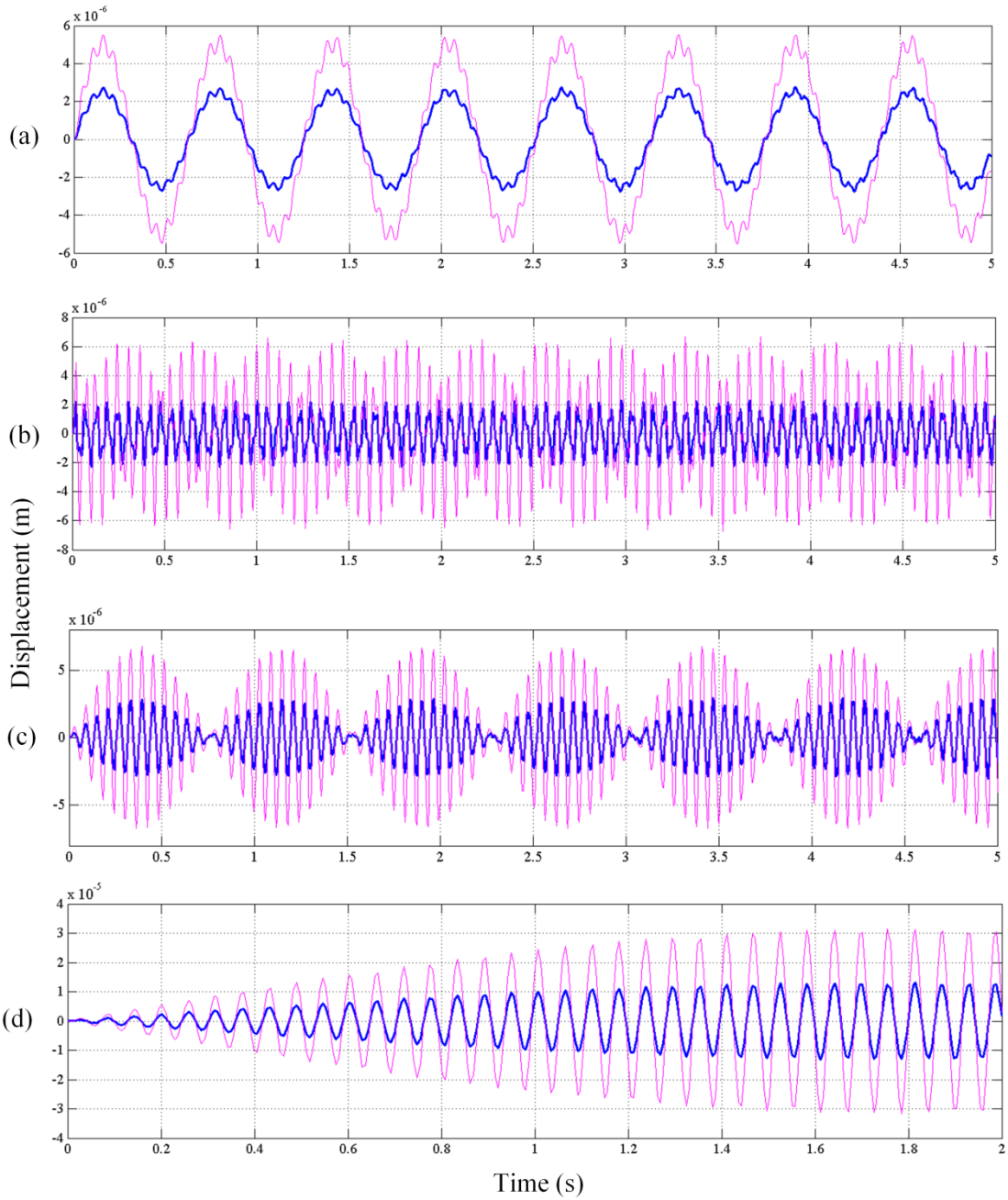

Fig.7-8 The result of forced vibration with different exciting frequency ω (a) $\omega_{11}=10$; (b) $\omega_{12}=200$; (c) $\omega_{13}=100$; (d) $\omega_{14}=122$.

The first-order natural frequency ω_{01} has been calculated for 122. It indicates

that when the exciting frequency is far less or more than natural frequency, transient vibration shows superposition of free vibration and steady-state vibration, and small displacement of two mass is demonstrated. When the exciting frequency is very close to the natural frequency, the beats vibration is obtained with small displacement of two mass, when the exciting frequency is equal to natural frequency, the large displacement of both mass is demonstrated. The second-order vibration also can be calculated as shown in Fig.7-9.

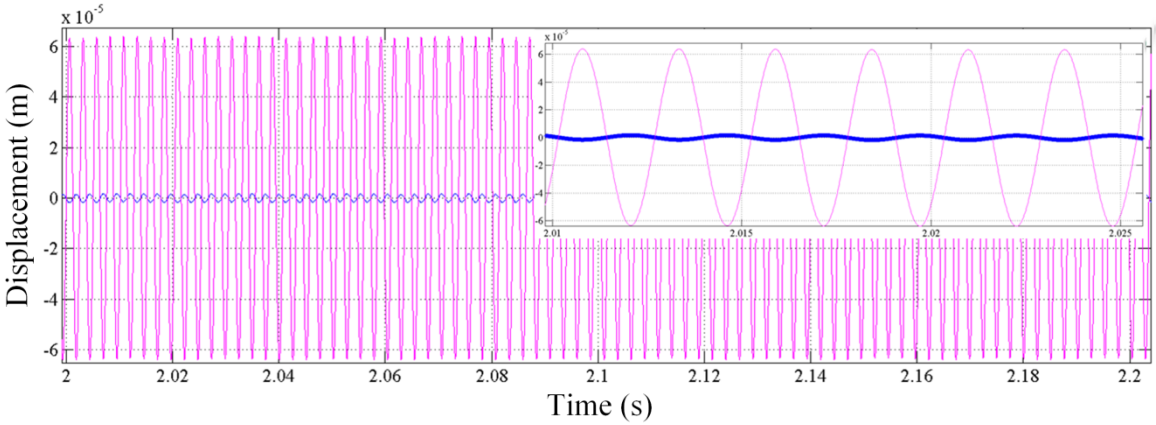

Fig.7-9 The result of forced vibration with second-order exciting frequency

The red line and blue line are displacement of m_1 and m_2 respectively, according to the mode shape of second-order resonant vibration, the direction of displacement for two mass are opposite, and the result of forced vibration with second-order exciting frequency is consistent with it. When the motion of m_1 rises, m_2 will go down at opposite direction. It is proved that the displacement of m_1 and m_2 at first two order forced vibration can be calculated using Simulink, and the first two resonant frequency can be determined by this method, finally the scanning angle can be calculated by displacement.

To research the effect of lumped mass for two degrees of freedom vibration,

displacement of m_1 and m_2 should be calculated with different mass ratio (m_1/ m_2), and scanning angle can be calculated by the displacement of m_1 and m_2, firstly, we assumed that the mass of magnet is constant as 0.005g, and m_1/ m_2 is decided for 1, 2, 5, and 100 respectively. The resonant frequency and scanning angle has been obtained and shown in Fig.7-10 and Fig.7-11 respectively.

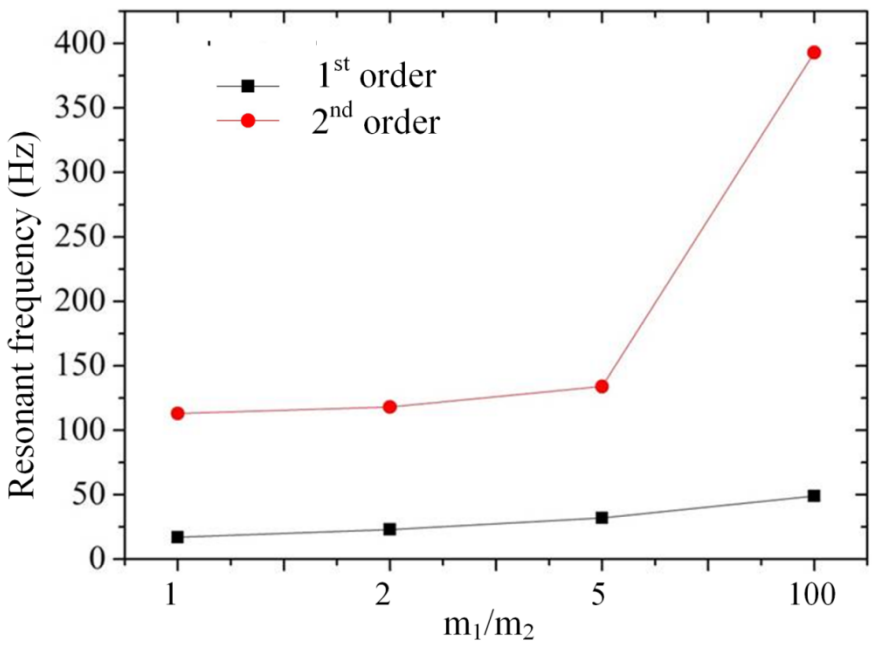

Fig.7-10 The calculated resonant frequency with different mass ratio at first two order vibration (The 1st model)

From the graph, we can see that there are two rising lines for resonant frequency, for the first-order vibration, it shows a slow rising trend with different mass ratio, a gradual upward trend is demonstrated before mass ratio of 5 at second-order vibration, it suddenly grows between mass ratio of 5 and 100, It indicates that the resonant frequency is increasing with decreasing lumped mass, especially, a dramatic growth for second-order vibration.

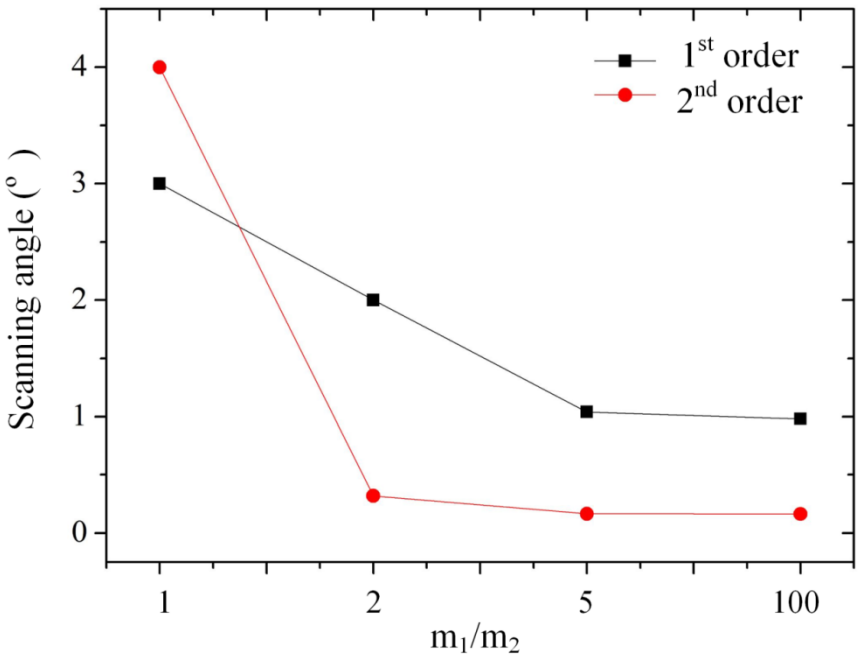

Fig.7-11 The calculated scanning angle with different mass ratio at first two order vibration (The 1st model)

The line graph shows the relationship between scanning angle and mass ratio. Form the graph it can be seen that an opposite trend is demonstrated compared with result of resonant frequency, and two large scanning angles were obtained at mass ration of 1 for first-order and second-order respectively. The trend dramatically goes down from 1 to 2 of mass ratio, and the largest scanning angle 4.02° was gained at 1 mass ratio for the second-order vibration.

The location of magnet is the middle of fiber called the first model as above mentioned, the first model of fiber scanner has been calculated and discussed, and next, the second model and third model should be calculated and discussed.

Firstly the stiffness matrix of the second and third model can be given by flexibility method as follows:

The stiffness matrix of the second model is

$$[a]_2 = \begin{bmatrix} \frac{L^3}{3EI} & \frac{4L^3}{3EI} \\ \frac{4L^3}{3EI} & \frac{9L^3}{EI} \end{bmatrix} \tag{5.28}$$

The stiffness matrix of the third model is

$$[a]_3 = \begin{bmatrix} \frac{L^3}{3EI} & \frac{4L^3}{3EI} \\ \frac{4L^3}{3EI} & \frac{9L^3}{EI} \end{bmatrix} \tag{5.29}$$

Where *E* and *I* are same as the first model and *L* is *1/3* of the L_f. And then the resonant frequency and scanning angle of the second and third model can be calculated using Simulink. The calculated results for the second model are shown in Fig.7-12 and Fig.7-13

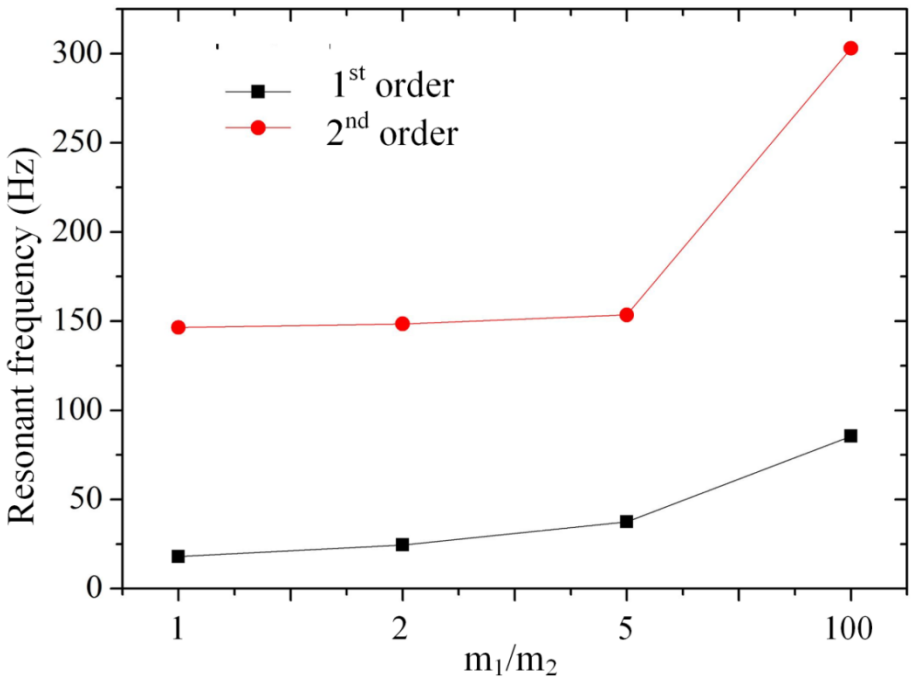

Fig.7-12 The calculated resonant frequency with different mass ratio at first two

order vibration (The 2nd model)

The line graph shows the relationship between resonant frequency and mass ratio. we can see that there are two rising lines for resonant frequency, for the first-order vibration, it shows a slow growing trend with different mass ratio, a gradual upward trend is demonstrated before mass ratio of 5 at second-order vibration, it suddenly grows between mass ratio of 5 and 100, It indicates that the resonant frequency is increasing with decreasing lumped mass, especially, a dramatic growth for second-order vibration, which is same trend as the first model.

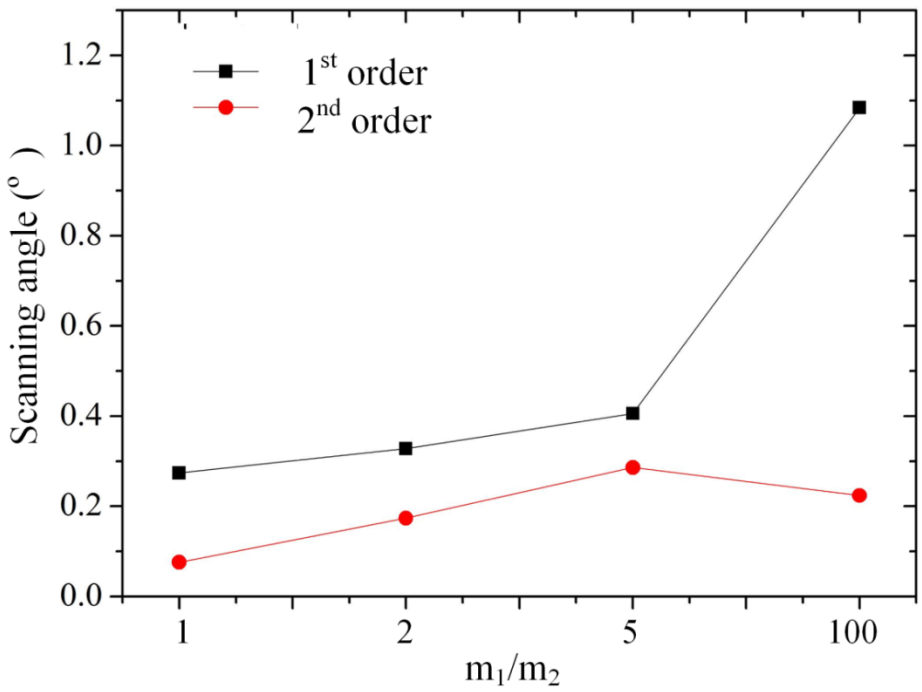

Fig.7-13 The calculated scanning angle with different mass ratio at first two order vibration (The 2nd model)

For this chart, it indicates that the larger scanning angle could be obtained at first-order vibration for all mass ratios. For the first-order vibration, at the beginning, the value of resonant frequency slightly increases, suddenly grows up due to the big

span for mass ratio. On the other hand, there is also a slow growth before mass ratio of 5, and a down trend is demonstrated with mass ration from 5 to 100. The largest scanning angle is 1.08° which is represented with mass ratio 100 at first-order vibration.

The identical changing trends of calculated results of resonant frequency are shown for the first and second model, but the changing trends of calculated results of scanning angle is completely different. Next, we should calculate the resonant frequency and scanning angle of the third fiber scanner model, the calculated results are shown in Fig.7-14 and Fig.7-15. It indicated that the calculated results of resonant frequency keep the same changing trend,

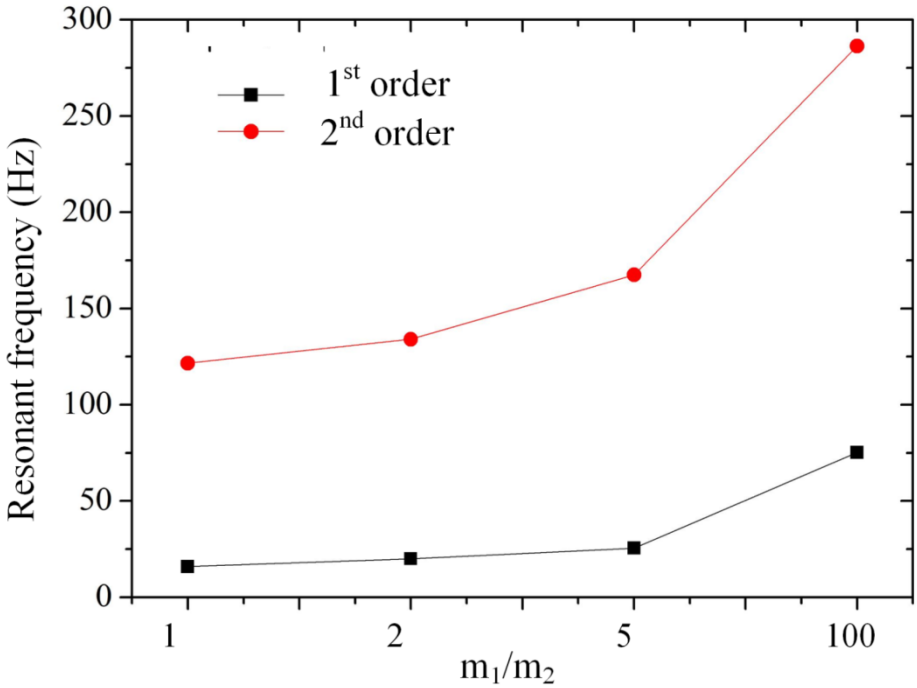

Fig.7-14 The calculated resonant frequency with different mass ratio at first two order vibration (The 3rd model)

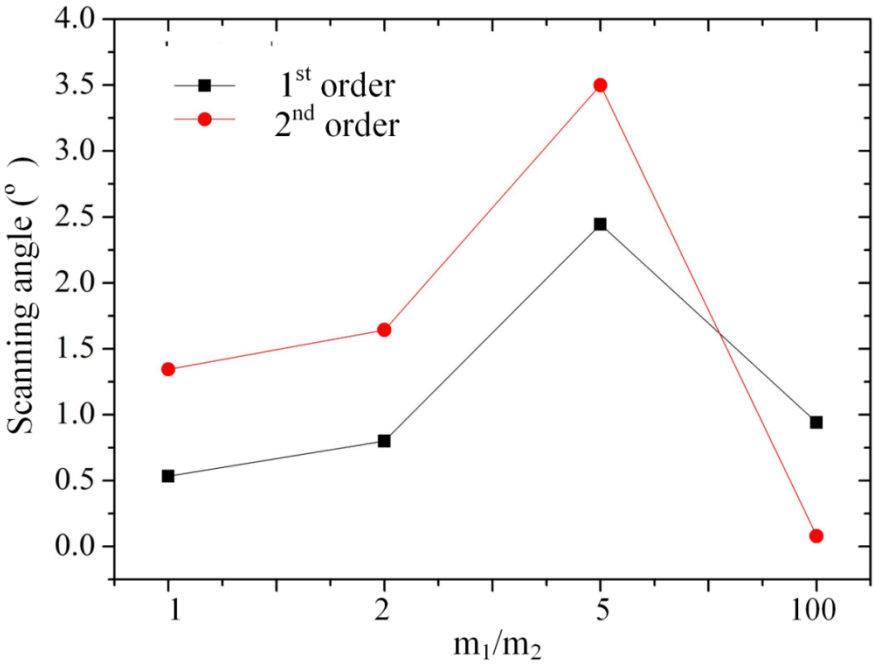

Fig.7-15 The calculated scanning angle with different mass ratio at first two order vibration (The 3rd model)

As we can see from this chart, there are two value peaks at mass ratio 5 for the first-order and second-order vibration. And the larger scanning angles at second-order vibration are demonstrated at mass ratio 1, 2 and 5. The largest scanning angle is 3.5°which is represented with mass ratio 5 at second-order vibration.

5.3 Summary

In this chapter, The designed fiber scanner was simulated on mechanical structure, the resonant frequency, displacement of fiber tip and scanning angle of designed fiber scanning were simulated using ANSYS with different F_1, The largest displacement and scanning angle both were obtained at F_1 for 3mm at first-order vibration, but the scanning angle is very small for 0.28°, the value is not enough for

fiber scanner application, so in order to enhance scanning angle, an improved design of fiber scanner should be proposed.

The improved designed fiber scanner was demonstrated as two degrees of freedom vibration, three fiber scanner models were decided according the location of magnet for calculation. The resonant frequency and displacement of m_1 and m_2 were calculated using Simulink, firstly, the feasibility of Simulink has been proved, next the resonant frequency and scanning angle were calculated for three fiber scanner model respectively.

The calculated results indicated that the resonant frequency of the first two order vibration for the three fiber scanner models show the same changing trend, but the changing trends of scanning angle are completely different. For the first model, large scanning angles are mostly demonstrated at first-order vibration, but when the mass ratio is 1, the scanning angle of second-order vibration is larger than one of first-order vibration, and it is also the largest scanning angle for 4.0°. For the second model, the scanning angles of first-order vibration are larger than second-order vibration for all mass ratio, the largest scanning angle is shown at mass ratio 100 for 1.08°. For the third model, large scanning angles are shown at second-order vibration. The largest scanning angles is 3.5° at mass ratio 5. Thus, the first fiber scanner model actuated at second-order resonant mode with mass ratio 1 is promising design for endoscope application.

6. FABRICATION PROCESS

Tilted microcoil would be fabricated on the surface of 1 mm diameter cylindrical polyimide pipe according to the requirements of design, and MEMS process is chosen, including sputtering, spray coating, lithography, etching etc. The fabrication process is very different from the traditional MEMS process, because that the substrate is polyimide pipe. For the sputtering process, three times of sputtering forms two uniform coatings, and a custom-made spray coating system is developed for coating resist on the polyimide pipe, the most critical process is the lithography process, a programmed 3D lithography system is proposed in this research. All process will be discussed in detail at next part. Finally, the electroplating process is employed for coating Cu coil line on coil-shape seed layer.

The fabrication process of a tilted microcoil was shown in Fig.6-1. A polyimide pipe was used as substrate with the 1 mm outer diameter and the 0.9 mm inner diameter. In the fabrication process, a polyimide pipe was sputtered with 120 nm Cr coating and 30 nm Au coating accordingly. In order to increase the binding force between the Cr and Au coating, the thermal treatment process was employed at 200℃ for 20 min after the sputtering. After that photoresist was coated onto the surface of the sputtered polyimide pipe using spray coating system which has been developed recently for preparing thin uniform photoresist coating on a cylindrical substrate. There was surface treatment process using a UV ozone treatment unit before spray coating. Next the spray coating process would be proceeding. The two

ends of the polyimide pipe would be fixed by two clips mounted on the two motors which can be driven synchronously at a certain speed of rotation using control panel. A heater nozzle is mounted next to the spray nozzle to realize real-time heating treatment, which is necessarily employed for obtaining a smooth surface without pinholes. Without the real-time heating treatment, there are some pinholes on the prepared coating, wavelike surface morphology are also visible. The distance between the spray nozzle and the substrate, rotation speed of the substrate, scan speed of the spray nozzle; spray cycles and other major parameter of the spray coating process can be independently controlled and programmed. In this work, the distance between the spray nozzle and substrate is 56 mm. it has been proved that the photoresist coating performs a better surface with few pinholes and particles at this distance. Shipley S1830 positive photoresist (Shipley Co.LLC) was employed as the spray coating photoresist. The solvent was AZ5200 thinner, (AZ electronic materials), which consists of propylene glycol monomethyl ether acetate (PGMEA).i.e. a common solvent for the direct spray coating process. In this work, 4 μm thickness of photoresist coating was sprayed on the circumferential surface of the pipe. After spray coating process, firstly, the photoresist-coated polyimide pipe was loaded on the exposure equipment, then it was fixed tightly by two clamps mounted on the two synchronously driven rotation stage, next, remaining level was adjusted for rotational stability, afterwards, previous compiled control program was loaded into computer, finally, the photoresist-coated polyimide pipe was exposed by UV light with the shutter open. A tilted microcoil pattern of the photoresist was

realized by controlling the rotation speed of substrate and linear movement speed of mask. After exposure and development of the phototresist, Cr and Au coating were etched by wet etching. According to the thickness of coating and etch rates, firstly, the sample was immersed into the Au etching liquor for 25 seconds, and then put it into the Cr etching liquor for 1min, after that the photoresist was removed by the acetone. At the last, the copper was electroplated on the Au seed layer of the coil pattern by mask-less electroplating process. The electroplating resolution which is developed by our lab and Meltex Inc., Japan has been employed, in which novel additive chemicals were used to mask-less electroplating process.

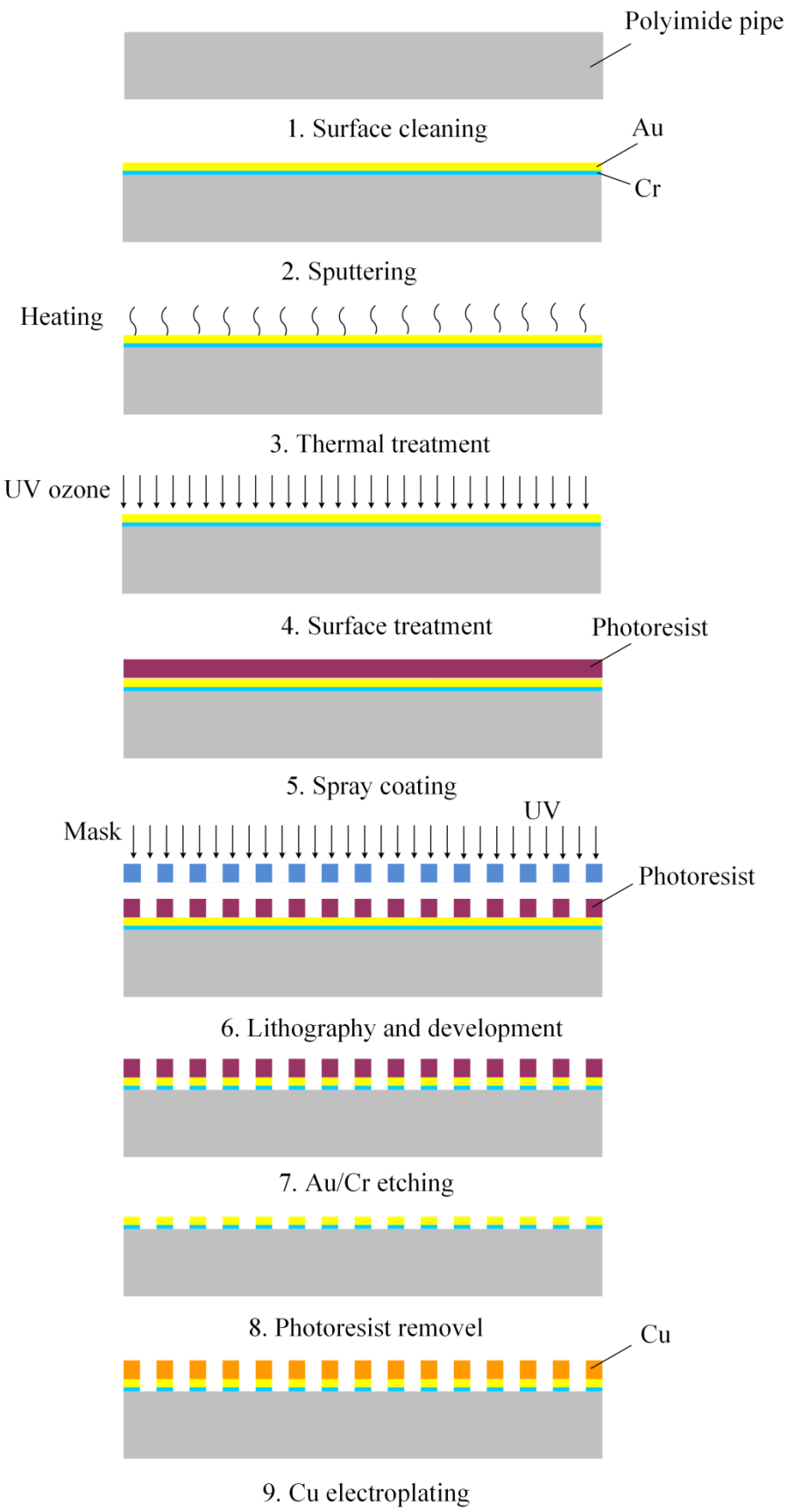

Fig.6-1 Fabrication process of a tilted microcoil.

6.1 Sputtering process

Firstly, a polyimide pipe was handled using supersonic wave cleaning equipment for one minute, and dried by air gun, next, it was fixed in the chamber of sputter, the sputtering process was shown in Fig.6-2, firstly, half of pipe was coated with Cr, and then took it out and turn it over, secondly, the other half of pipe was sputtered with Cr and Au, Cr and Au targets could be rotated clockwise, and finally, half of Cr-coated pipe was coated with Au. The operating conditions were shown in Tab.6-1. Optical image of sputtered polyimide pipe was shown in Fig.6-3.

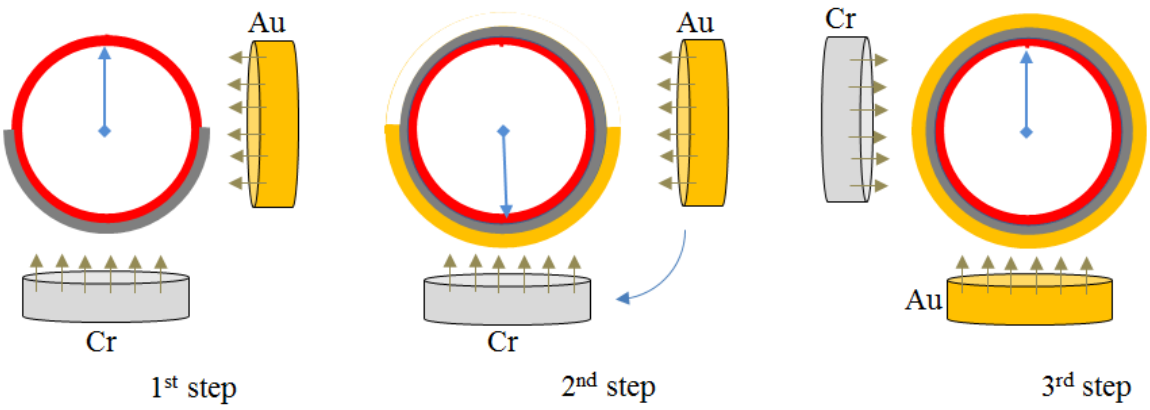

Fig.6-2 schematic of sputtering process

Tab.6-1 The operating conditions of sputtering process

Coating	Thickness	Pre-sputtering	Sputtering	Vacuum	Power
Cr	20nm	18~20min	3min	1.6E-6Torr	100w
Au	120nm	15~18min	6min	1.6E-6Torr	100w

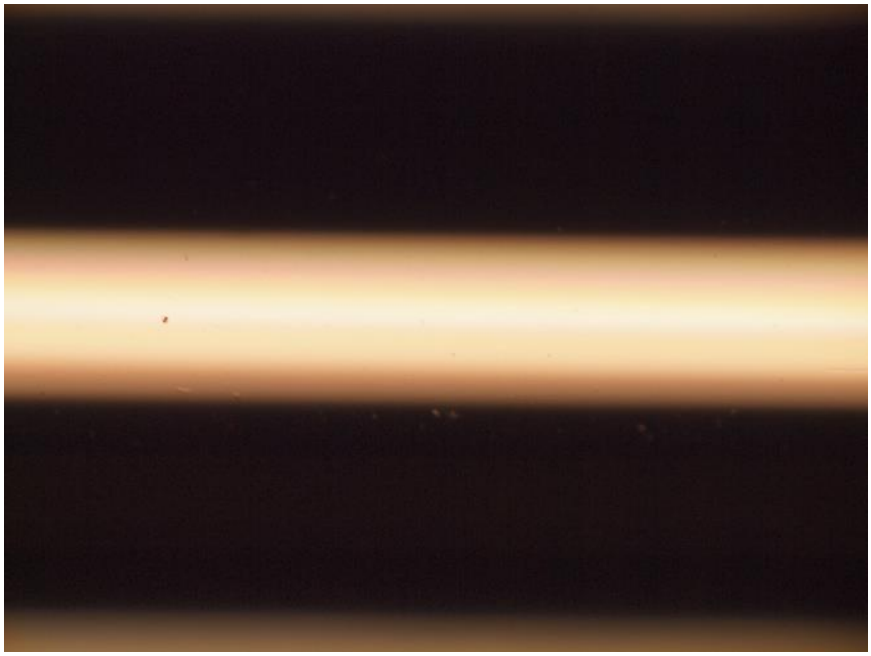

Fig.6-3 Optical image of a sputtered polyimide pipe

6.2 Spray coating process

Pipe substrates like glass pipes and polymer pipes have been extensively used for MEMS device application due to their unique feature compared with conventional plane substrates such as silicon and glass wafer [93-97]. For instance, they are very cheaper and easy to obtain such as fibers and polymer pipes. Recently, some MEMS sensors and actuators used as implanted biomedical devise have been integrated on the surface of flexible polymer pipes, but there are a lot of limitations of piped-based MEMS devices, because the pipe substrates are not compatible with conventional MEMS batch process. Sasaki et al [98] and Abeysingheet al [99] successfully developed a micro transducer integrated onto fiber for communication application, which is fabricated by conventional MEMS process, therefore, it is significantly inventible to develop a special micro fabrication process for pipe substrates.

Recently a special 3D lithography system has been developed using a pipe-based MEMES exposure module. This system has been successfully employed for forming a functional pattern onto pipe substrate. But to improve pattern without distortions and defects, a novel spray coating system has been developed for obtain uniform and thin photoresist coating, as illustrated in Fig.6-4

The custom-made spray coating system consists of two synchronous rotating motors, its rotation speed can be controlled by program, real-time heat treatment system, a spray nozzle combined with heat nozzle, temperature sensor, and programmed control panel and so on.

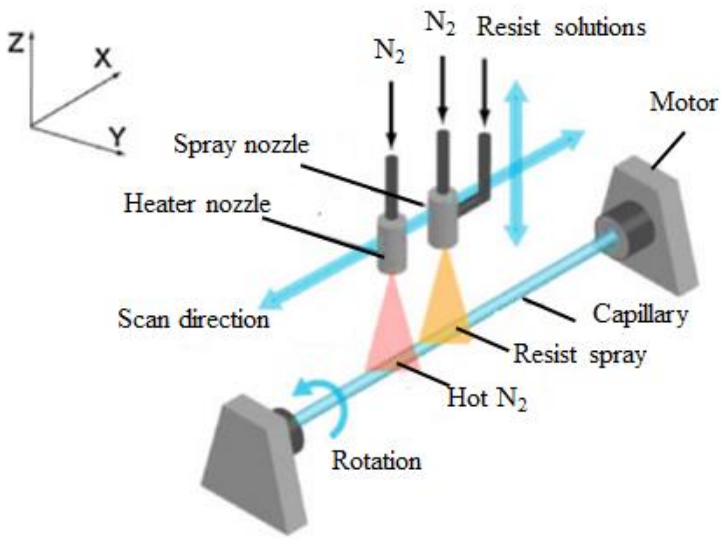

Fig.6-4 Schematic of custom-built spray-coating system.

Pipe substrates (diameter from 125um to 2mm) all can be rotated by two motors at certain speed which is controlled by control panel.

In order to conduct a real-time heat treatment, a heat nozzle is mounted next to spray nozzle at the same height; Nitrogen is lead into the heat nozzle and heated inside, directly spraying on the pipe substrates. The temperature sensors are utilized

for control the temperature of nitrogen. The diameter of the spray jet is approximately 34 mm, which is at a distant 70mm under the spray nozzle. To avoid interference effect, the hearer nozzle is 65 mm away from spray nozzle. The major parameters of this new spray coating system have been investigated as followings:

(1) The real-time heat treatment; (2) The concentration of the thinner (3) Diameter and rotating speed of pipe substrates (4) The distance between nozzle and substrates

Originally, to investigate the quality of resist film on pipe substrates, a series of experiments has been conducted by our group. AZ P4210 positive photoresist (AZ electronic Material) was used. The thinner solvent is AZ 5200 thinner (AZ electronic Material), the major ingredient of which is propylene glycol monomethyl ether acetate (PGMEA), i, e. a common solvent for spray coating process. A 125um diameter quartz fiber and 375um, 500um 1mm and 2mm quartz capillaries were used as substrates. All the substrates called fiber here for easy description. A photoresist coating was prepared on fiber with certain weight ratio 1:2 of AZ P4210/AZ5200 with heat treatment and without heat treatment at different distance between spray nozzle and substrate in previous research [100]. That indicates that at distance of 25 mm and 35 mm, when real-time heat treatment is provided, a smooth surface is obtained. Without heat treatment, there are some pinholes and defects on it. At distance of 50 mm and 70 mm, the surface significantly becomes smooth and uniform.Fig.6-5 shows the measured thickness of resist coating versus rotation speed using weight ratio 1:2 of AZ P4210/AZ5200 with heat treatment at distance 70mm between nozzle and substrates.

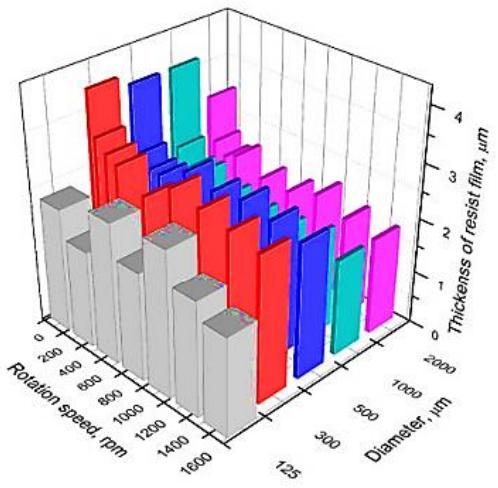

Fig.6-5 Measured thickness of the resist film versus the rotation speed

That indicates that the thickness of resist coating decreased rapidly with increasing rotation speed or fiber diameter, 125 um diameter fiber is exception, in this work, the substrates used for spray coating is 1 mm diameter pipe. So we should concentrate on the resist coating of the 1mm diameter fiber. Obviously, a better and thin resist coating on 1 mm diameter pipe can be obtained at speed of 1500 rmp, weight ratio 1:2 of photoresist/thinner, scan cycles of 3, at distance of 50 mm or 70 mm with heat treatment. Fig.6-6 shows optical image of the prepared thin resist coating on the 1mm diameter pipe at distance 50mm, 56mm, and 70mm respectively. At distance of 50mm, many pinholes are visible in the resist coating, at distance of 56 mm, the photoresist coating became thinner but the number of pinholes obviously became few, at distance of 70mm, some aggregated particles of photoresist were found in the coating, so the distance was fixed at 56mm, the thickness of the photoresist can be adjusted by scan cycles.

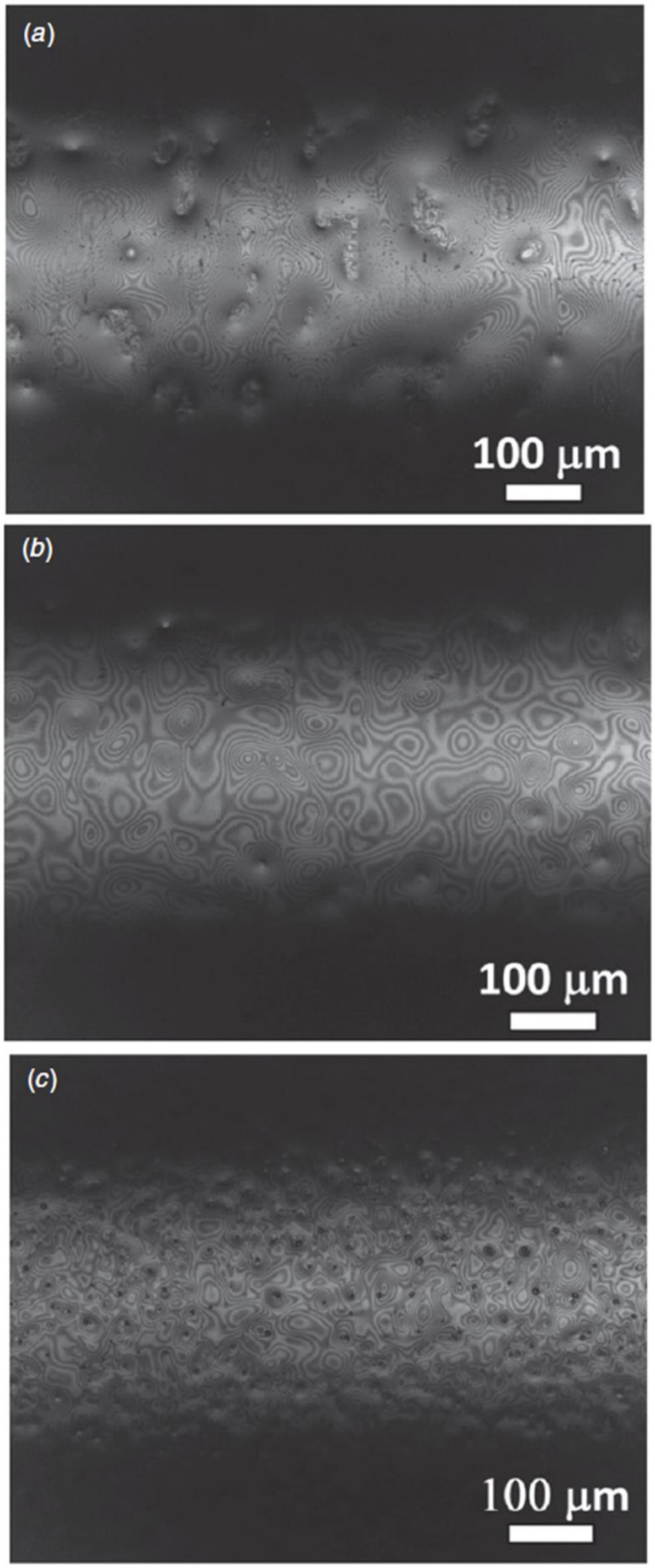

Fig.6-6 Optical photographs of the deposited photoresist films on the 1 mm diameter pipe. The distances between the spray nozzle and the pipe are (a) 50; (b) 56 and (c) 70 mm, respectively.

In this research, the distance between the spray nozzle and substrate is 56 mm. it has been proved that the photoresist coating performs a better surface with few pinholes and particles at this distance. A 4μm thickness of photoresist coating was sprayed on the circumferential surface of the pipe. The optical image of photoresist-coated polyimide pipe is shown in Fig.6-7

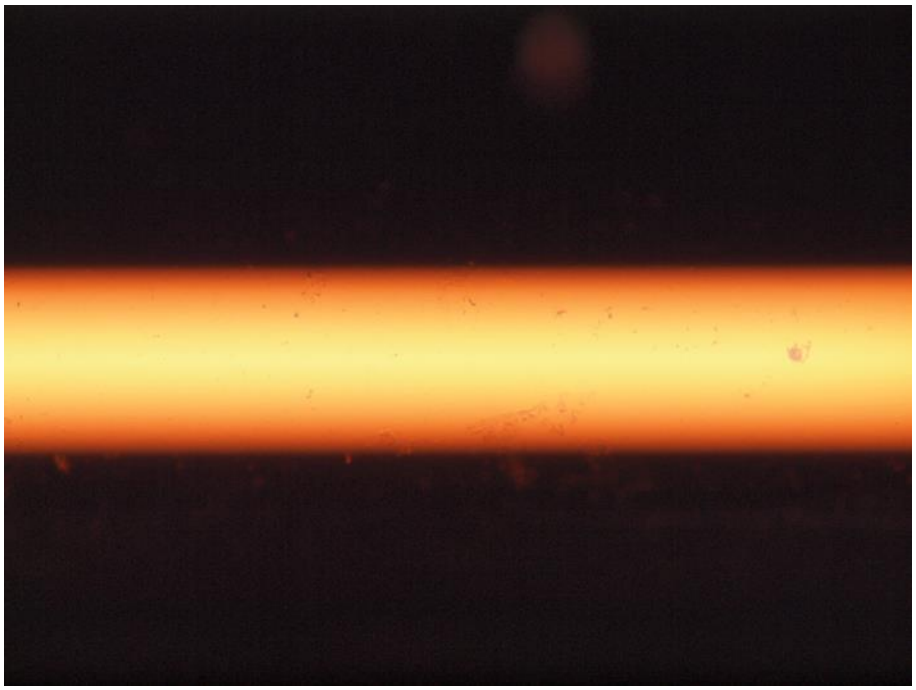

Fig.6-7 Optical image of photoresist-coated polyimide pipe

6.3 3D lithography process

6.3.1 Introduction to 3D lithography system

In the past several years, diverse optical lithography technologies have been developed for not only fabricating 2D pattern with high resolution and large aspect

ratio, but also providing complex 3D structure. Mostly the complex 3D structures were fabricated as functional transducers, recently the pipe substrates integrated with functional transducer have been used as invaluable tools for many aspects due to their unique merits on shapes, especially as medical tools. As the pipe substrate, polymer pipe is cheaper and easy to manufacture in small diameter, if can be integrated with micro transducers around it, it will became invaluable tools used inside human body. So a high-resolution micro patterning technology is required. Several conventional cylindrical lithography methods have been developed for making fine micro pattern round the surface of a cylindrical substrate. For example, two-photon polymerization and rotational projection lithography methods, as shown in Fig.6-8. a method is often used for micro/nano-stereolithography research field due to its high resolution and lithographic flexibility [101-106], but it performs lower lithographic speed than the method b, to realize high resolution and high speed lithography process, a mask pattern projected cylindrical lithography system is considered, especially for patterning a complex-shaped microcoil structure with a large number of coil turns, although a microcoil structure was patterned with high aspect ratio, synchrotron radiation facility is required larger space and high cost., from this viewpoint, A newly projection cylindrical lithography system was developed by us, a UV illumination resource combined with a programmable cylindrical projection lithography (PCLitho) system has been proposed accordingly, as show in Fig.6-9.

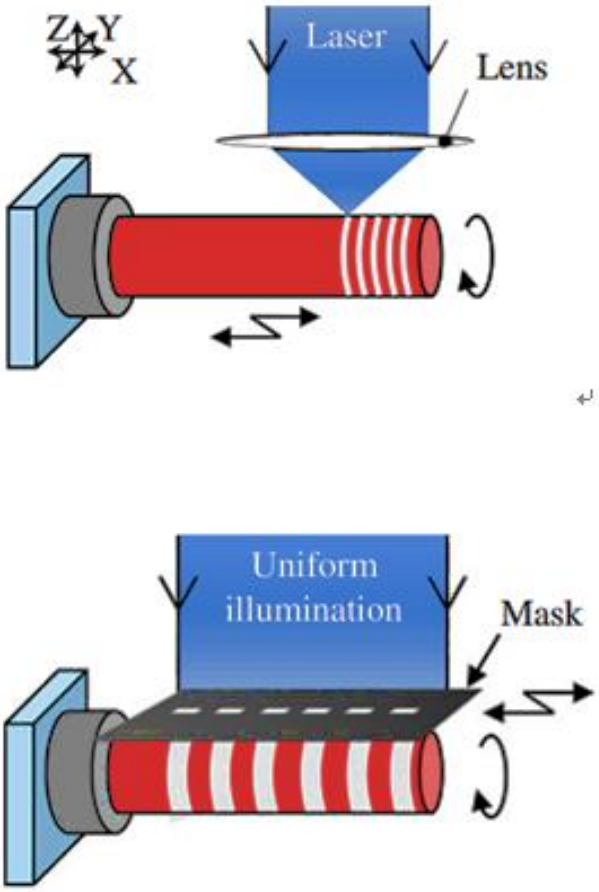

Fig.6-8 The schematic diagram of conventional cylindrical lithography methods: (a) Two-photon polymerization, (b) Rotational projection lithograph

The equipment mainly consists of four parts: (1) A uniform illumination system; (2) A reduced projection lithography system; (3) A synchronized motion stage system ;(4) A CCD multilayer alignment system;

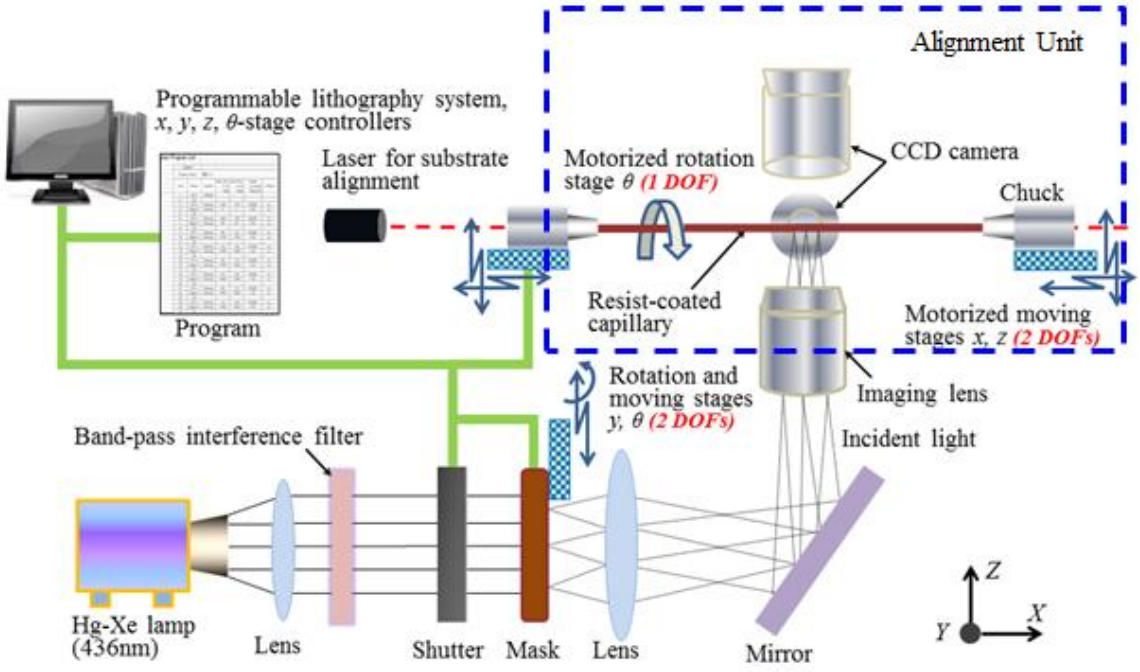

Fig.6-9 The schematic diagram of programmable cylindrical projection lithography (PCLitho) system

A UV illumination source is used for providing uniform incident light, and light intensity can be adjusted as requirements, the incident light from a UV-light source is focused onto a photoresist coated cylindrical substrate with a reduced mask image by passing it through the optical elements of lenses, mask, and mirror. In this present work, the incident UV-light from an Hg–Xe light source (LC8, Hamamatsu Photonics) has a broad wavelength range of 250–600 nm. This broad wavelength of incident light results in chromatic aberration in the focal plane. In order to remove this aberration, a band-pass interference filter with a central wavelength of 436±10 nm was inserted between the light source and the shutter. Furthermore, to obtain a high resolution, a reduced projection lithography system consisting of an imaging lens and a biconvex lens, which is commonly known as an “infinity corrected optical

system (ICOS)," was used to precisely focus and transport the mask patterns. The ICOS consists simply of an objective lens used as an imaging lens, and a biconvex lens. Therefore, the overall magnification of the lithography equipment is directly determined by the magnifying power of the objective lens. Considering the required size and complexity of the microstructures to be developed, the optical magnification of the ICOS was selected as 0.5, an objective lens with magnifying power of two times is applied as an image lens, ±45μm focus length are obtained for projection pattern, two identical chunked are mounted on the motorized rotation stage to fix the substrate (a polymer pipe in this work) for coaxial rotation. At the same time,, the laser path from a He-Ne laser was used as a reference to align all these elements, tune the optical axes and make sure their coaxial rotations. Two CCD cameras are employed for alignment during lithography process as shown in Fig.6-10, horizontal position of pipe can be adjusted and observed from side view CCD camera, the projected pattern of mass can be simultaneously observed by top view CCD camera, a real-time monitoring can be accomplished by these two CCD cameras. There are five degree of freedom (DOFs) existed in the lithography system, the movement and rotation of mask and pipe substrate can be simultaneously controlled by computer along these DOFs, XYZ—θ all the stages are motorized automatically by software and program, and exposure time can be precisely controlled, In the each direction, the accuracy of movement and rotation was set to 0.1 μm and 0.01° respectively, these values were defined as the repeat positioning accuracy of the automatic stages used. The expected micropatterns on the photoresist-coated pipe can be drawn by

executing the programmable sentences in PC lithography controlling window. Finally, the photoresist microstructures will be obtained on the pipe surface after the development.

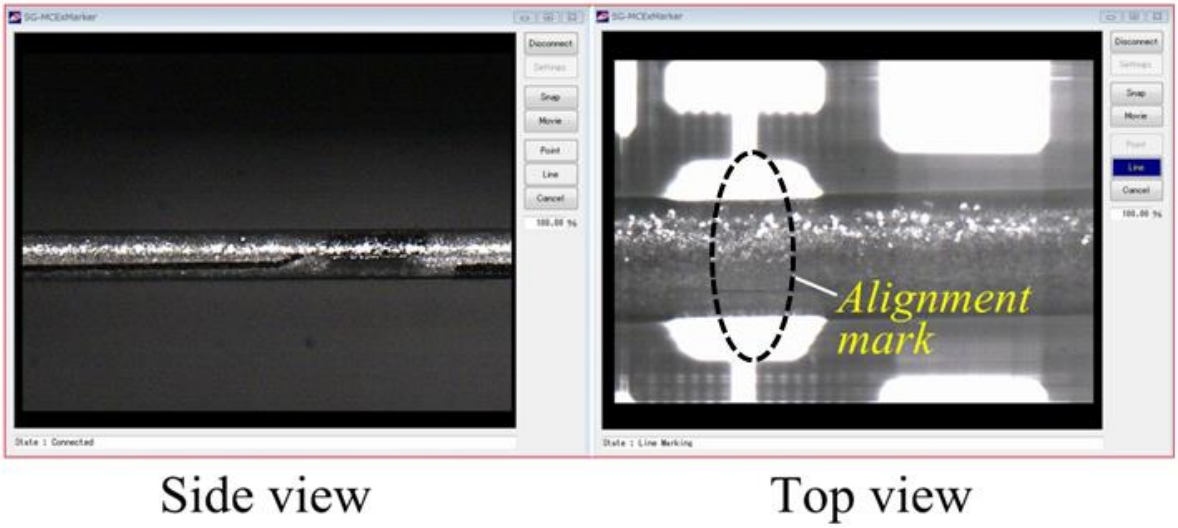

Fig.6-10 Side and top views during the alignment

6.3.2 Mask design and program

Before demonstrating design process of mask pattern and control program, exposure process in detail should be introduced, a schematic of a pipe coated with photoresist as shown in Fig.6-11 (a), it will rotate anticlockwise and exposed from 0° position to 360° position (0° position), UV illumination is fixed and keep exposure vertically, mask is placed between UV illumination and 0° position, the mask could move forward and backward along vertical direction to the paper, thus, when the substrate is rotating and mask is moving at same time, a tilted exposure path will be realized.

To observe easily, we cut and spread substrate as two dimensional surface, as

shown in Fig.6-11 (b) Pink area and blue area are photoresist and exposure area respectively, white windows are mask pattern, at the beginning, the mask pattern is projected at 0° location, when the mask pattern is moving horizontally, meanwhile, substrate is slowly rotating, a exposed path will be performed as blue area, for example, if the mask included five rectangular windows called multi-lines pattern, five turns tilted coil will be fabricated. Firstly, we assume that substrate is rotating slowly, and the mask is controlled by program and moving forward, the distance of forward move is D. so the tilted angle is decided by the distance of forward move D. the mask moves forward form 0° position to 180° position, and moves backward from 180° position to 360° position, in to realize continuous coil line, backward distance is less than forward distance for one spacing.

The rotation speed of substrate and movement speed of mask can be controlled by program and decided by the tilt-angle, forward distance mask, backward distance of mask, exposure time, exposure intensity and diameter of substrate. And the tilt-angle, and coil pitch are mainly decided by parameters of mask pattern, including the length and width of each window, spacing between two windows, the number of the windows, as shown in Fig.6-12.

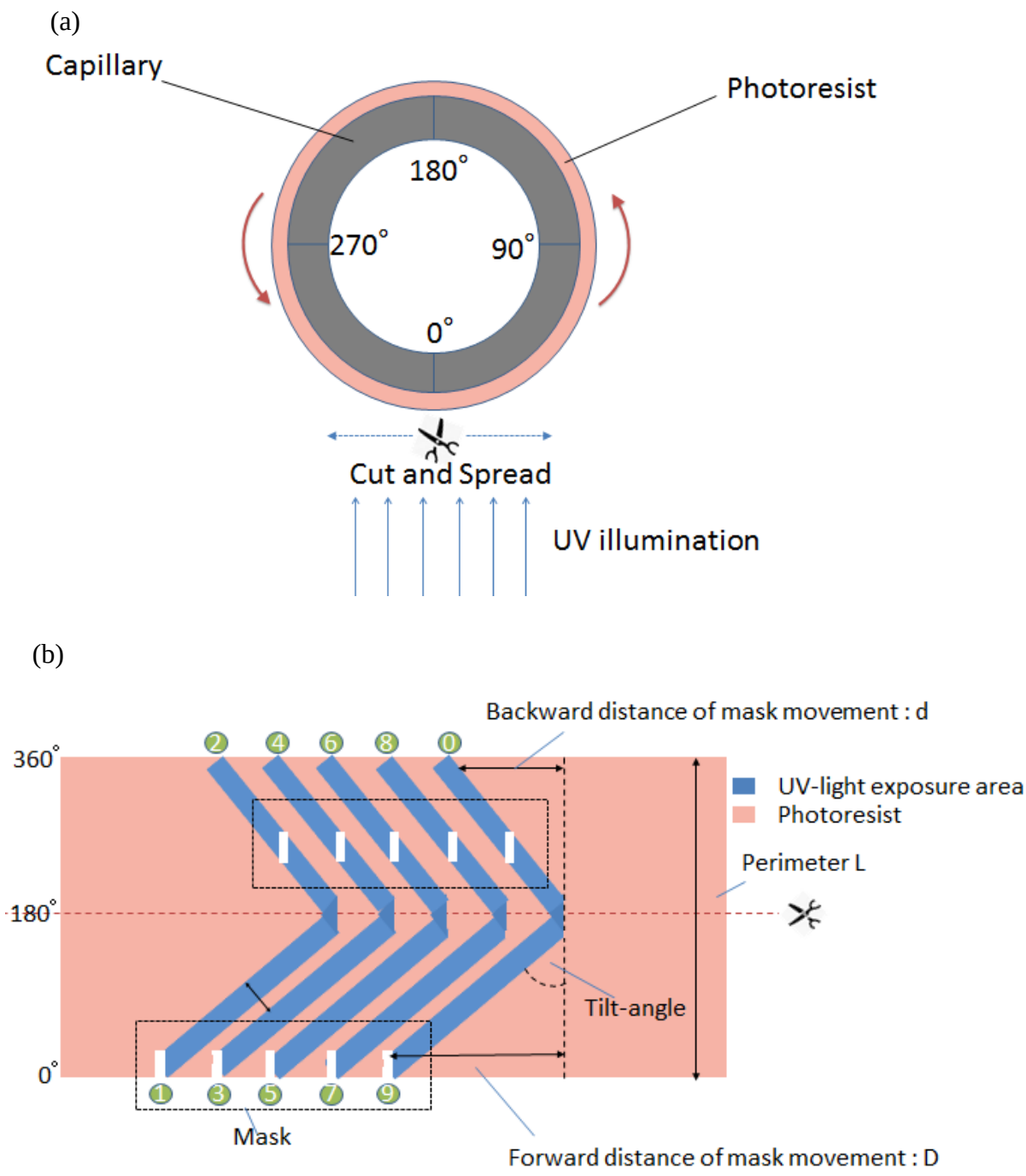

Fig.6-11 Schematic of exposure process in detail (a) Resist-coated cylindrical substrate (b) surface development of resist-coated cylindrical substrate

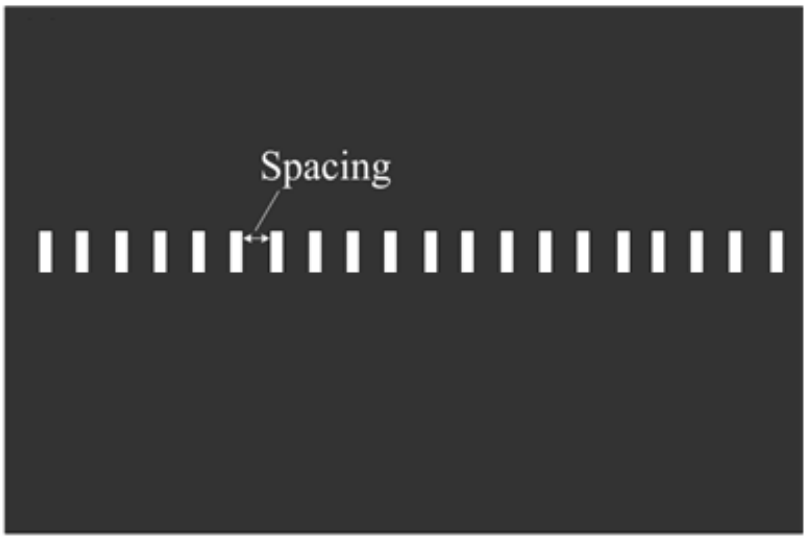

Fig.6-12 Schematic of mask pattern with multi-lines

The length and width of window are 170μm and 40μm respectively, the relationship between the spacing of designed mask pattern and corresponding parameters of prospective tilted coil is shown in Fig.6-13.

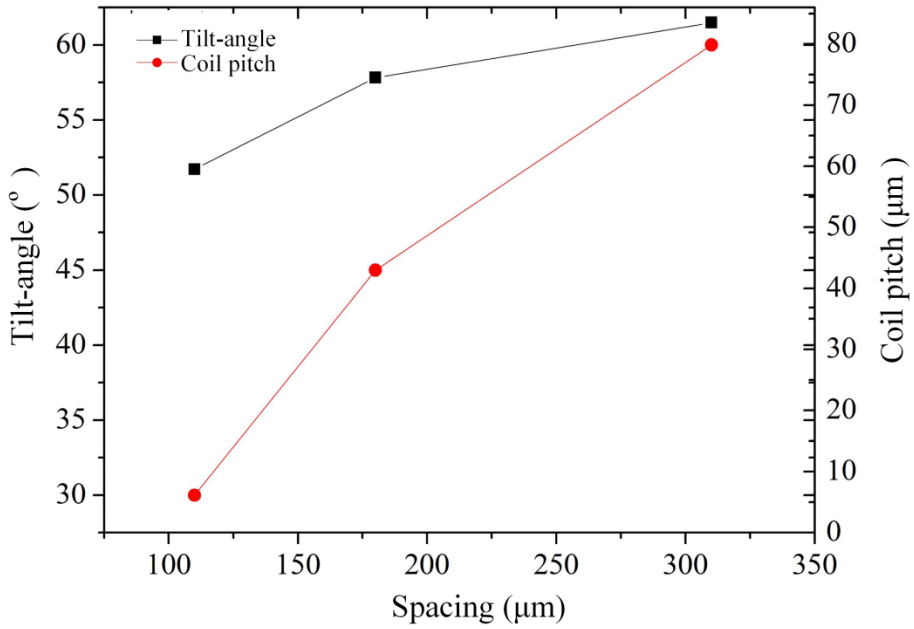

Fig.6-13 Relationship between spacing of mask pattern and prospective tilt-angle and pitch of coil

It indicates that the spacing of mask pattern is decisive factor for tilt-angle and pitch of fabricated coil, large tilt-angle and pitch can be realized by large spacing. After designing the mask, the control program should be written using excel, a tilt microcoil pattern is realized by controlling the rotation speed of substrate and linear movement speed of mask synchronously as aforementioned. Firstly, the distance of linear movement can be decided according to the tilt-angle: 45ºtilt-angles for 3180μm and 60º tilt-angle for 5444μm, then exposure time is selected on the basis of the size of line pattern, 10min, 20min, 30min, 40min and 50min were attempted by us, for the conclusion, 40 min realizing sufficient exposure can be used for 40x170 lines, Rotation speed of substrate and movement speed of mask are closely related with the exposure time, which can be calculated by exposure time. Mask movement is separated into two parts: forward movement for 0º-180º rotation of substrate and backward movement for 180º-360º rotation. The distance for forward movement is 3180 μm for 45 º tilt-angle microcoils and 5444 μm for 60 º tilt-angle microcoils, but the distance for backward movement is 3000 μm for 45 º tilt-angle microcoils and 5134 μm for 60º tilt-angle microcoil. To obtain the continuous coil line, the distance, be equal to spacing, is subtracted during the backward movement. The rotation speed and movement speed are decided as following: forward movement speed, backward movement speed and rotation speed for 45 º tilt-angle microcoils are approximately 2.65μm/sec, 2.50μm/sec and 0.15deg/sec; forward movement speed, backward movement speed and rotation speed for 60º tilt-angle microcoil are approximately 4.54μm/sec, 4.28μm/sec and 0.15deg/sec. The representative optical image of

photoresist pattern of microcoil with 45º tilt-angle fabricated on the polyimide pipe by the cylindrical projection lithography technique is shown in Fig.6-14 (a) and (b). The photoresist pattern of microcoil with tilt-angle of 45º was patterned with 10um±0.2μm coil width, 78.5±0.5μm coil pitch and 20 turns. And the photoresist pattern microcoil with tilt-angle 60º was also successfully patterned with 10um±0.2μm coil width, 81.5±0.5μm coil pitch and 20 turns, as shown in Fig.6-14 (c) and (d).

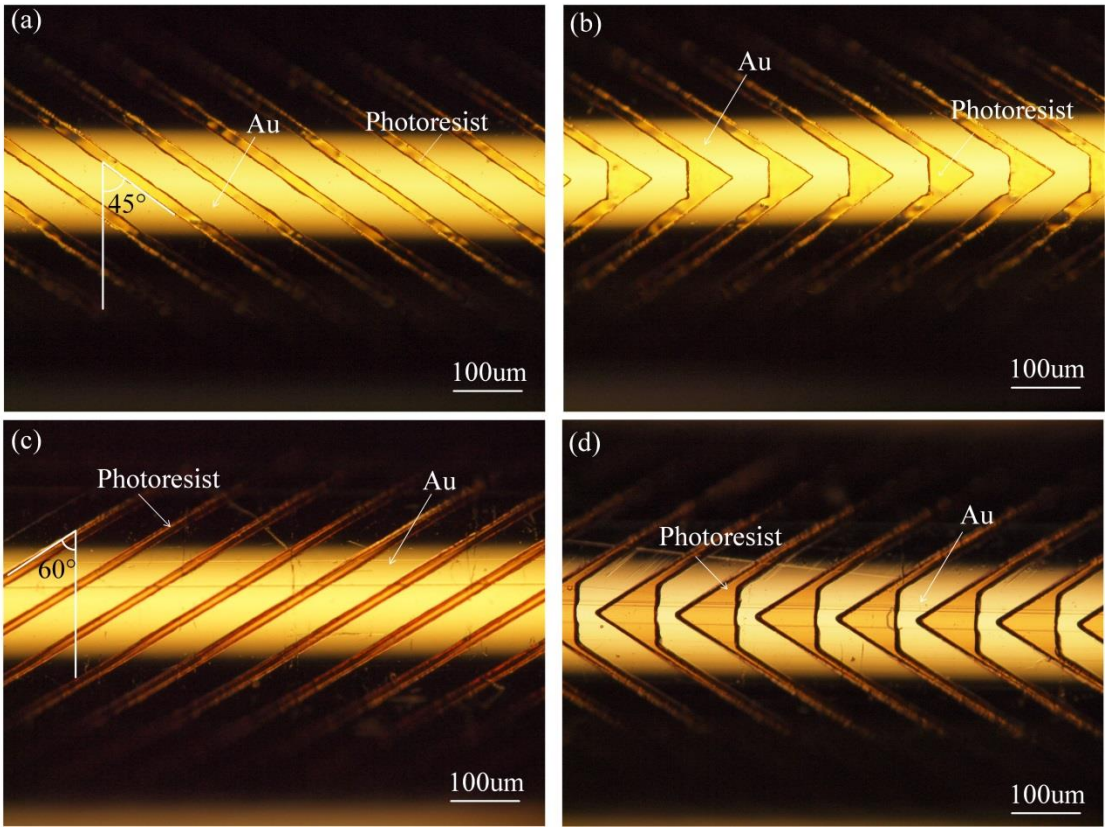

Fig.6-14 Optical image of fabricated tilted microcoil (a) 45º tilt-angle microcoil, (b) junction of 45º tilt-angle microcoil, (c) 60º tilt-angle microcoil, and (d) junction of 60º tilt-angle microcoil

6.4 Etching process

After exposure and development of the photoresist, Cr and Au coating were etched by wet etching process. According to the thickness of coating and etching rates, firstly, the sample was immersed into the Au etching liquor for 25 seconds, and then put it into the Cr etching liquor for 1min, after that the photoresist was removed by the acetone, as shown in Fig.6-15

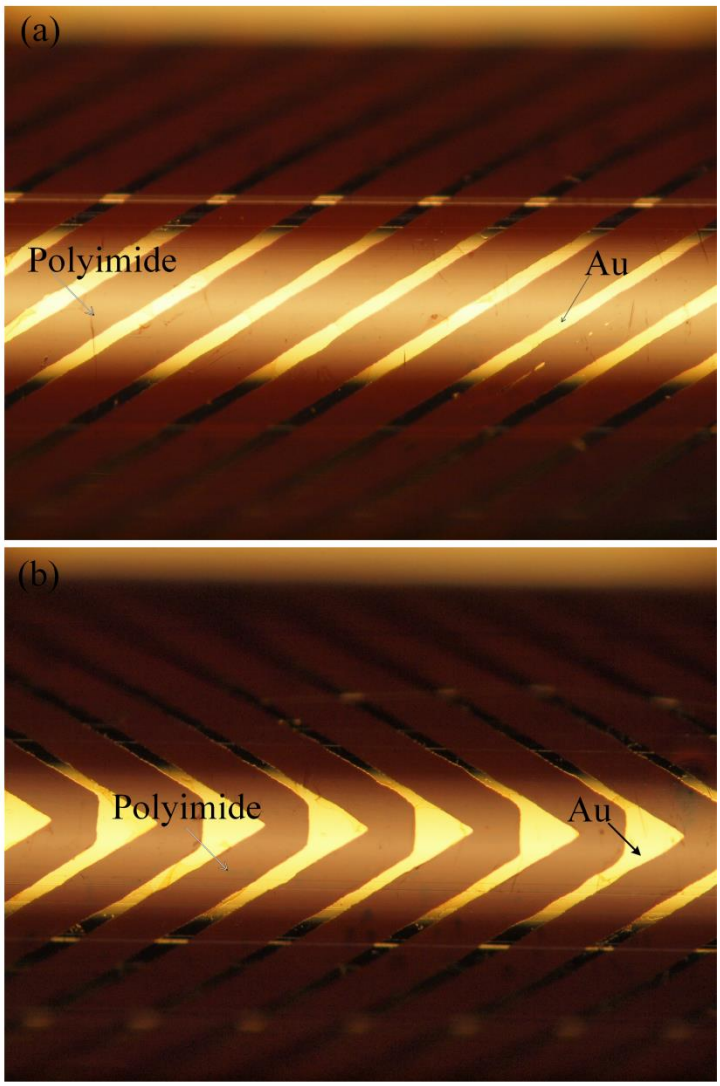

Fig.6-15 Optical image of etched tilted microcoil (a) 60º tilt-angle microcoil, and (b) junction of 60º tilt-angle microcoil

the photography of 20 turns microcoil prepared on the 1mm diameter polyimide pipe with 60º tilt-angle after Au etching, Cr etching and photoresist removal, as is illustrated in Fig.6-16.

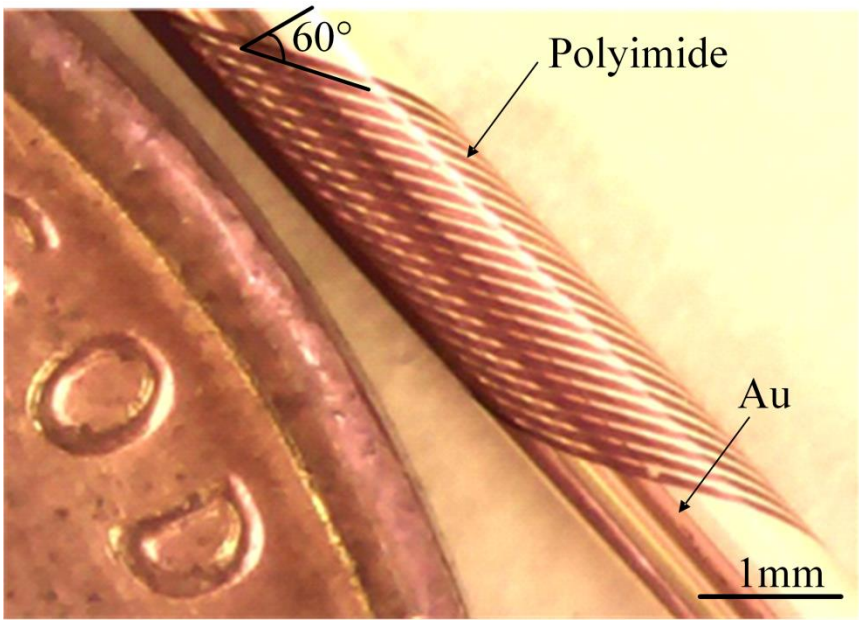

Fig.6-16 Optical image of 60º tilt-angle microcoil

6.5 Electroplating process

The SEMs of the electroplated copper microcoil is shown in Fig.6-17. Copper was electroplated with Au coil line as seed layer without photoresist mask. And the Cu coil line grows along Au coil line vertically and expands both sides. In our case, Cu coil line width increases to 40μm and thickness grows to 15μm based on 10μm Au coil line. The microcoil with tilt-angle of 60º, line width of 40μm, and thickness of 15μm was successfully obtained. And then the driving displacement of the electroplated microcoil is measured by high speed camera, but no fiber tip displacement is demonstrated. And the reasons could be summarized as followings: (1); (2); and (3); to prove the tilted microcoil breakover, inductance has been measured, as shown in Fig.6-18

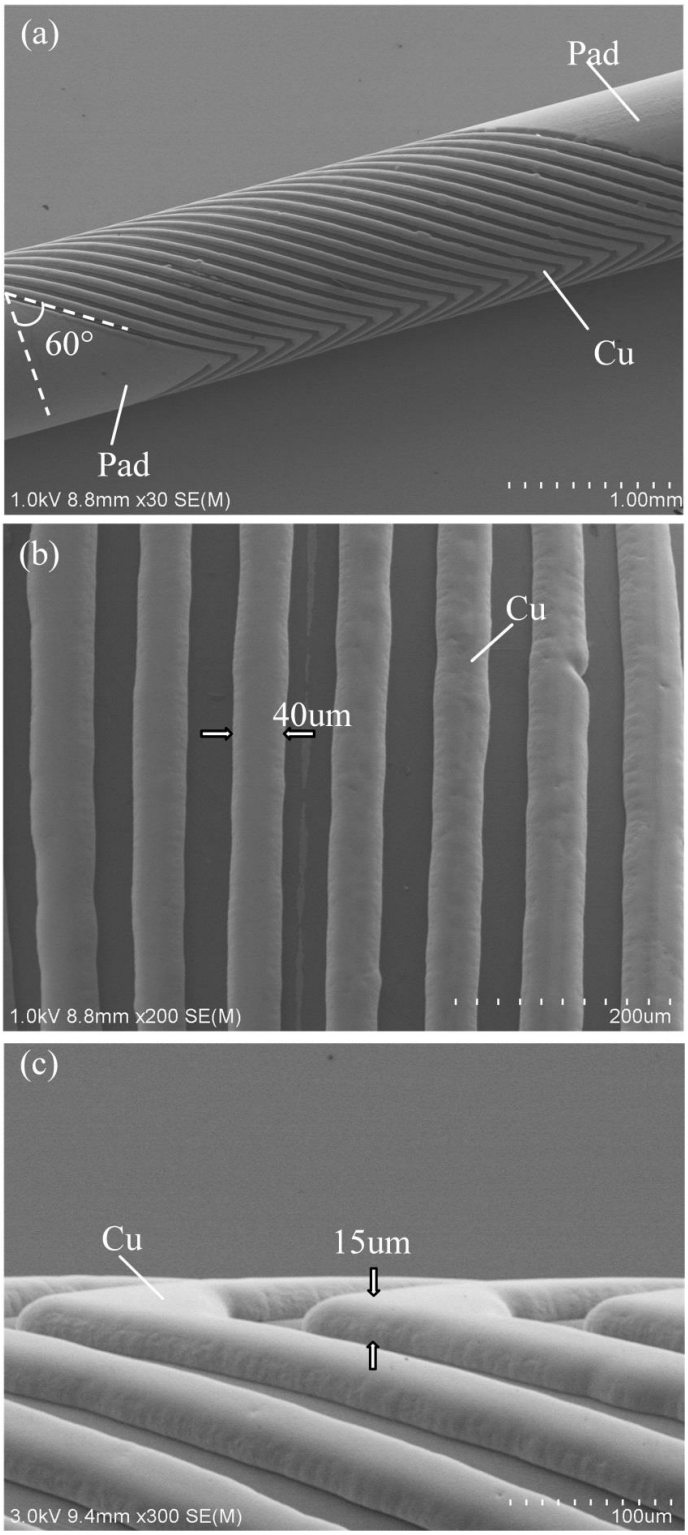

Fig.6-17 SEMs of the electroplated tilt microcoil(a) Intact coil; (b) line width and spacing; (c) thickness of Cu microcoil

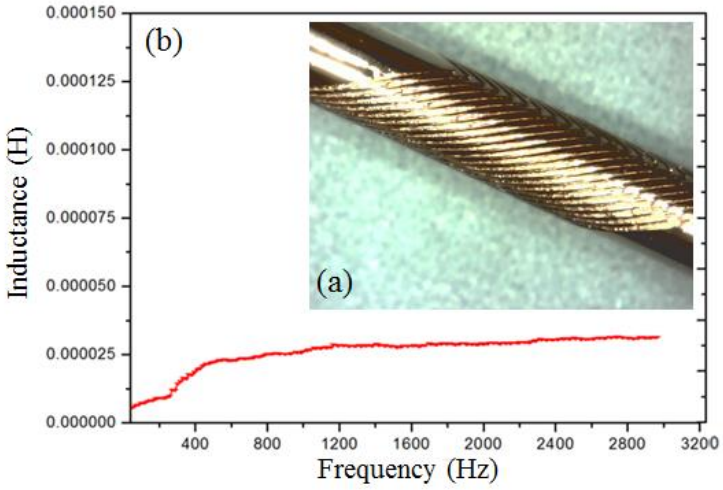

Fig.6-18 (a) Optical image of the electroplated tilted microcoil; (b) Measured inductance of the tilt microcoil.

6.6 Summary

Tilted microcoils have been fabricated on a polyimide pipe by newly developed MEMS-based fabrication process. The process includes spray coating, the cylindrical projection lithography and mask-less electroplating micromachining. In particular, the photoresist pattern of microcoil with high resolution has been obtained successfully using this lithography method. The dimensions of the two fabricated tilted microcoils were as follows; a 45º tilt-angle, 10±0.2 μm line width,78.5±0.5 μm coil pitch and 20 turns as well as a 65º tilt-angle, 10±0.2 um line width, 81.5±0.5 μm coil pitch and 20 turns. Finally, a direct mask-less electroplating process was employed for obtaining 15μm thickness copper microcoil on the surface of Au seed layer, and the width of copper line was expanded to 40 μm.

7. ELECTROMAGNETIC-ACTUATED FIBER SCANNER BASED ON 3D PRINTING PROCESS

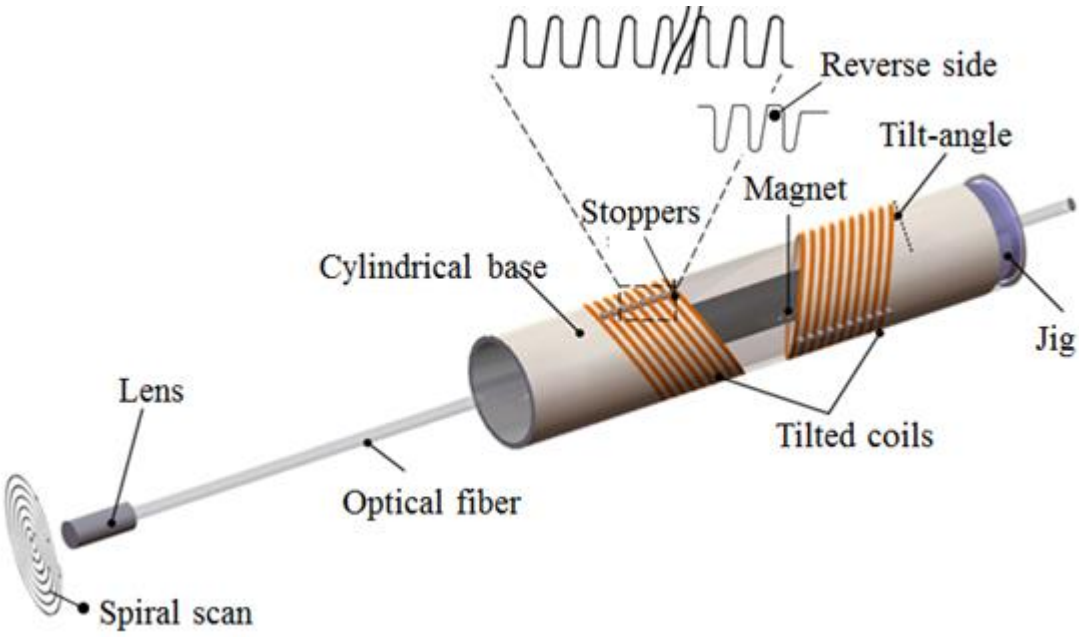

Fig.7-1 Schematic of fiber scanner based 3D printing process

It has been proved that single optical fiber cannot be actuated by the electroplated microcoil. The electroplating coating of it is very thin and uniform, even brittle, and it does not perform good heat effect and electrical characterizes, so scanning displacement is limited. Thus, a novel hybrid process is required for manufacturing ultra-thin tilted coil with decreased pitch, large tilt-angle, and good electrical characteristics, providing a large driving force.

Our goal is to produce a novel ultra-thin electromagnetic actuator with decreased pitch and large tilt-angle for single optical fiber scanner, from this viewpoint, traditional industrial enameled Cu wire meet above requirements, and it can be custom-made with various diameter ranged from 25μm to 75μm. But it could not be

aslant closely winded on the surface of ultra-thin cylindrical substrate like glass and polymer tube, because fixation is challenge for this method. So we proposed a cylindrical substrate with many micro stoppers based on the 3D printing technique to realize fixation of aslant closely winded coil.

7.1 Fundamental structure

So an improved design and a hybrid process have been introduced into this work, the improved design is shown in Fig.7-1. This scanner consists of single optical fiber, a collimator lens, a cylindrical magnet (Cobalt Nickel), a jig and two tilted coils (X-axis driving coil and Y-axis driving coil). A 125 μm diameter optical fiber is positioned at the center of actuator using a jig. A collimator lens is fused at the tip of optical fiber and a magnet is fixed on the fiber. Finally, two tilted coils are manufactured on the surface of 3D printed substrate. The outer and inner diameters of it are 1mm and 0.6 mm respectively.

7.2 Manufacturing method

The hybrid process is combining three-dimensional (3D) printing technology with homemade process. It is selected by this research due to its high precise, effective and fast fabrication ability, and easily used for mass production. The fabrication process based on 3D CAD (Computer Aided Design) model that is converted into “slices” to be physically fabricated layer by layer. A UV-curable resin can be exposed by a light source to cure the material to a solid-layer. In this work, we

use Acculas SI-C1000 and epoxy resin material to fabricate a cylindrical base with micro stoppers at printing temperature of 60º, it can be cured at the super-precision resolution of 1μm by a high-precision digital light exposure mechanism, and minimum lamination pitch can reach to 5μm.Thus, it is very useful for trial production, development and manufacture of micro devices.

7.3 Manufacturing result

A tilted coil prototype has been fabricated using this hybrid process, as shown in Fig.7-2. Although simulation result shows that tilt-angle of 50º coil can provide a larger torque under unsaturated magnetization, in order to claim fabrication ability of hybrid method, a 60º tilt-angle coil was decided for fabricating the prototype,. The outer and inner diameter of this 3D printed cylindrical base is 1.4mm and 800μm respectively, and many micro stoppers occupied at two side of the sleeve, the width and length of stopper are 80μm and 300μm respectively, 75μm diameter copper wire was winded around the cylindrical base with tilt-angle of 60º.

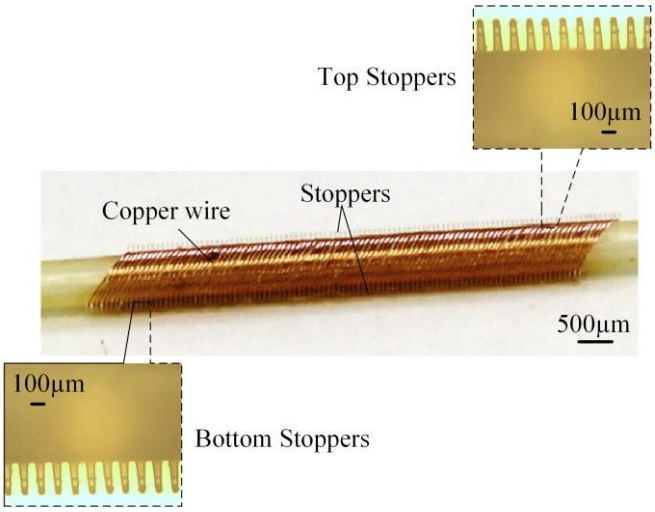

Fig.7-2 The structure of prototyped tilted coil.

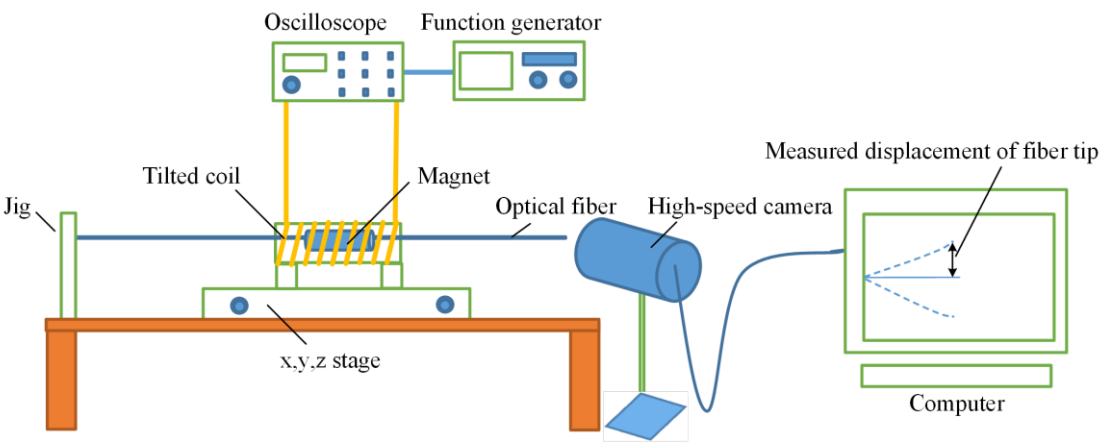

Fig.7-3 The schematic of the measurement setup

7.4 Measurement result

To evaluate driving characteristic of the prototype, measurement setup was assembled with one tiled coil, as shown in Fig.7-3. To observe the motion of fiber tip, high speed camera was employed for recording at the free end of optical fiber. The electrodes of the driving coils were electrically connected to the function generator and oscilloscope to generate the alternating electromagnetic field. The overall length of optical fiber used in measurement is same as the one of simulation, and D the location of magnet is 3mm. We experimentally obtain scanning displacement of fiber tip by sweeping the frequency of 1 voltage drive signal from 1Hz to 1800Hz, resonant frequency of the first two orders vibration of this fiber scanner is 420Hz and 1520Hz respectively, and two peaks of displacement of fiber tip are shown in Fig.7-4. They are 60.5μm and 9.3μm respectively. Obviously, it is three point two times to the one generated by electroplated coil, and it indicates that resonant frequency is consistent with simulated result, but there is large error comparing with simulated result, That is because that the simulation involved with two kinds of software, one

for simulating magnetic force torque, one for simulating displacement, which lead to decrease precise.

The displacement of fiber tip also has been measured at different relative positions between tilted coil and magnet. The magnitude and frequency of applied voltage are 1V and 420Hz respectively. When the half of magnet is placed out of tilted coil, the largest displacement of fiber tip can be obtained, and it is 85.7μm, as shown in Fig.7-5. The trend of change is same as simulated result on relative positions.

To enhance displacement of fiber tip, increasing voltage signal should be applied to the tilted coil ranges from 1V to 10V. And it has been measured with rising voltage at certain frequency of 420Hz, as shown in Fig.7-6. It is obvious that displacement of fiber tip linearly significantly increases with the growing drive voltage. The maximum displacement can reach to 125.3μm. It can provide displacement ranges from 85.7μm to 125.3μm, realizing a spiral scan without excessive current. Compared with other reported ultra-thin fiber scanners, the designed fiber scanner could not obtained larger displacement than PZT actuated fiber scanner [63], but it shows a low cost and effective way for fabrication, on the other hand, it shows 3 times larger than the displacement of fiber tip obtained by electroplated tilted coil [56]. Thus, the hybrid process is the appropriate method for fabricating a tilted coil, and it is an easy and effective way, it shows a promising application for ultra-thin medical endoscopes.

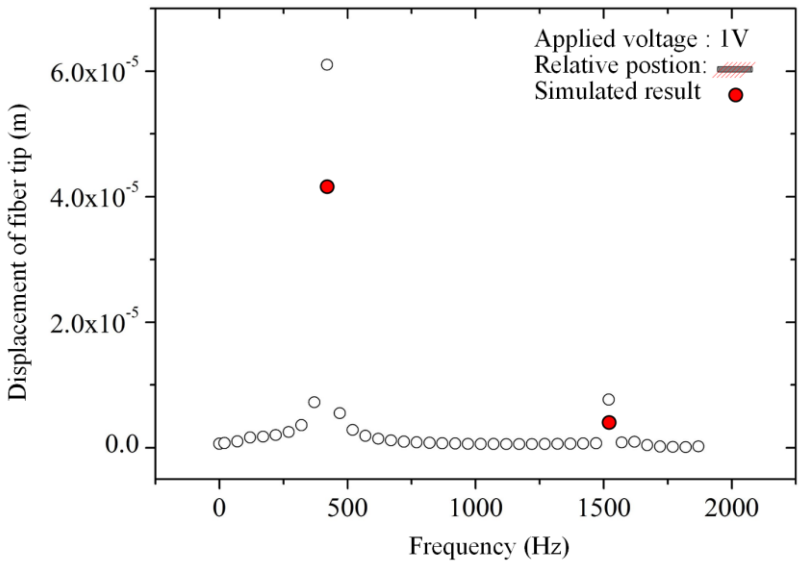

Fig.7-4 Measured displacement of fiber tip by sweeping frequency from 1Hz to 1800Hz

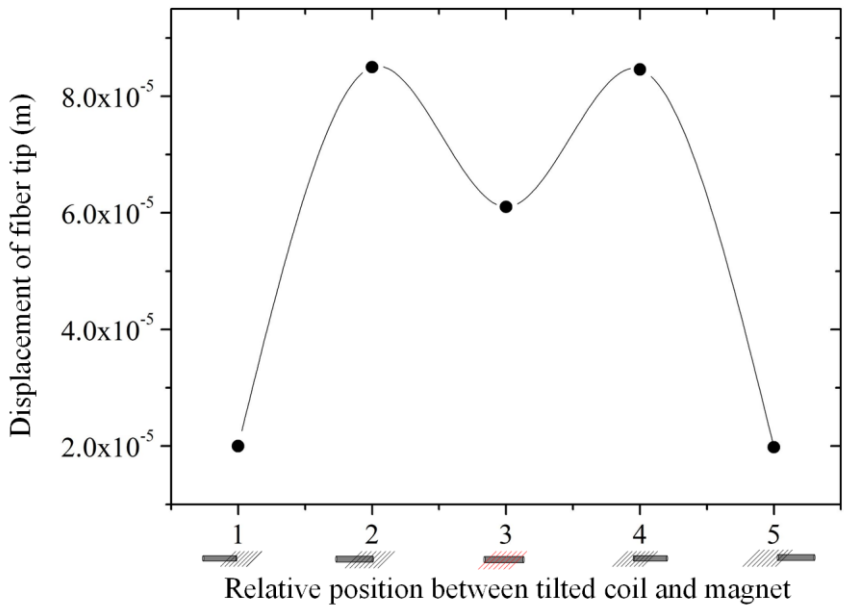

Fig.7-5 Measured displacement of fiber tip at different relative postion between tilted coil and magnet

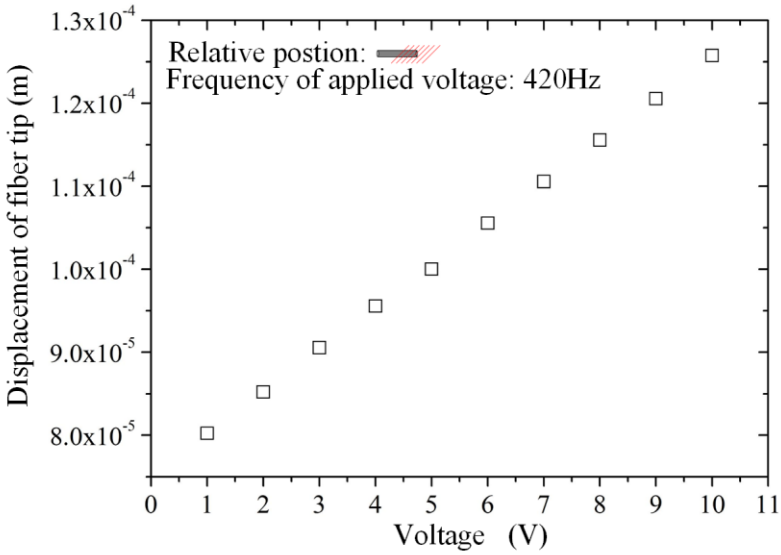

Fig.7-6 Measured displacement of fiber tip with increasing voltage.

7.5 Summary

This chapter proposed a novel tiny actuator for single optical fiber scanner, manufactured by a hybrid process combining 3D printing technology with homemade method at low cost. Our goal is to increase driving force, further extending scanning displacement of fiber tip as well as diminishing overall diameter of fiber scanner. To optimize the design parameters of this fiber scanner, driving force and vibration characteristic have been simulated. Finally, an ultra-thin tilted coil was successfully obtained by 3D printing technology and hybrid process according to optimized parameters. Line pitch, tilt-angle, resistance, and turns of it are 75μm, 60º, 20Ohm, and 100 respectively. Its scanning performance has been proved experimentally. As a result, when the tilted coil is applied with 1 voltage and magnet is placed inside tilted coil, displacement of fiber tip of 60.5μm is demonstrated at first-order resonant frequency of 420Hz; when the half of magnet is

located outside tilted coil, 85.7μm displacement is obtained; when the tilted coil is applied with increasing voltage, displacement grows significantly. It is proved that hybrid process is high efficient, high speed, low cost method for fabricating tiny tilted coil, large displacement of fiber tip can be provided by this coil is due to its decreased pitch and good electrical characteristics. It shows great potential for medical endoscope application.

8. CONCLUSIONS AND FUTURE WORK

8.1 Conclusions

As presented in Chapter 1, this research effort has been following the main objective of the research project -- the development of a new ultra-thin optical scanner for micro-endoscopes for biomedical imaging applications.

Firstly, a novel ultra-thin electromagnetic actuator design is presented. The new design solves the problems of large volume for probes of conventional endoscopes, being able to inspect narrow space inside human body. A tube-shape actuator, a tilted microcoil is designed for actuating single optical fiber with a magnet. The parameters of tilted microcoil have been optimized by the simulation of magnetic force and the analysis of off-axis magnetic field. Thus, it is designed for a 80 μm pitch , 60° tilt-angle microcoil with 20 turns.

Secondly, the dynamic characteristics of the designed fiber scanner have been discussed, conventional mechanical structure of single optical fiber scanners depend on optical fiber cantilever or one degree freedom vibration, they are all providing large scanning displacement and angle at first-order resonant vibration, in this research, a novel mechanical structure has been proposed as two degrees freedom vibration system. A lumped mass is added at fiber tip for forming two degrees freedom vibration. And the simulation result shows that larger scanning angle was obtained at first-order vibration for the one degree freedom vibration, and for the two degrees freedom vibration, the larger scanning angle was obtained at second-order

vibration, and the largest scanning angle was provided by two degrees freedom vibration for 4.0^{o} .

Next, the fabrication process of a tilted microcoil has been designated, including sputtering process, 3D lithography process, spraying coating process and mask-less electroplating process. finally, a tilted microcoil was fabricated with 15 μm thickness, 81.5±0.5 μm coil pitch, 60° tilt-angle and 20 turns. However, no fiber tip displacement could be measured.

Finally, a novel hybrid process is proposed for manufacturing a tiny tilted coil. A 2.0 mm diameter tiny tilted coil is achieved, and line pitch, tilt-angle, resistance, and turns of it are 75 μm, 60º, 20 Ohm, and 100 respectively. The scanning motion of assembled scanner was measured by high speed camera, and maximum 125.3 μm displacement can be measured at first-order vibration. Thus, the hybrid process is the appropriate method for fabricating a tilted coil, and it is an easy and effective way, it shows a promising application for ultra-thin medical endoscopes.

8.2 Future work

The design and fabrication of a novel fiber scanner was introduced into this research, the actuator, a tilted coil has been designed and fabricated by MEMS process and hybrid process. And the hybrid process demonstrated great potentials for fabricating tilted coil. The following research efforts are suggested for future work.

1. A much smaller pitch tilted coil should be manufactured by the hybrid process, providing a large driven force and scanning angle.

2. This fiber scanner is operated at high resonant frequency, and heating issue should be resolved like adding a lumped mass at fiber tip, decreasing frequency and increasing scanning angle.

3. The reliable of clinical usage should be concerned for medical endoscopes, reliability of device such as long-term reliability and repeatability, and sustainability to external shock need to be studied, especially the two masses vibration system.

4. A micro collimator lens should be manufactured for this fiber scanner, being integrated with confocal imaging system.

5. Two across tilted microcoils should be manufactured for realizing a spiral scan with amplitude-modulate.

6. The fiber scanner will be packaged and measured in the actual experimental environment such as blood vessels.

REFERENCE

[1] .J. Hsieh Published, “Computed Tomography, Second Edition: Principles, Design, Artifacts, and Recent Advances,” 2009.

[2] A. G. Farmana, and W. C. Scarfeb, “Development of imaging selection criteria and procedures should precede cephalometric assessment with cone-beam computed tomography,” *Am J Orthod Dentofacial Orthop*, vol. 130, pp. 257–265, 2006.

[3] R. R. Edelman, and S. Warach, “REVIEW ARTICLE Magnetic Resonance Imaging,” *N Engl J Med,* vol. 328, pp. 708-716, 1993.

[4] S. Mori, B. J. Crain, V. P. Chacko, and P. C. M. VanZijl, “Three-dimensional tracking of axonal projections in the brain by magnetic resonance imaging,” *Annals of Neurology,* vol. 45, pp. 265-269, 1999.

[5] E. J. Seibel, “1-mm catheterscope,” *Optical Fibers and Sensors for Medical Diagnostics and Treatment Applications VIII, Proc. SPIE,* vol. 6852, pp. 07-15, 2008.

[6] B. I. Hirschowitz, L. E. Curtiss, C. W. Peters, and H. M. Pollard, “Demonstration of a new gastroscope, the fiberscope,” *Gastroenterology,* vol, 35: 50-3. 13. 1958.

[7] X. Liu, Y. Huang, and J. U. Kang, “Dark-field illuminated reflectance fiber bundle endoscopic microscope”, *J. Biomed. Opt,* 16(4), 046003, April 05, 2011.

[8] R. T. Kester, N. Bedard, L. Gao, and T. S. Tkaczyk, “Real-time snapshot hyperspectral imaging endoscope”, *J. Biomed. Opt.* 16(5), 056005, May 10, 2011.

[9] C. J. Engelbrecht, R. S. Johnston, E. J. Seibel, and F. Helmchen, “-compact fiber-optic two-photon microscope for functional fluorescence imaging in vivo,” *Optics Express,* Vol. 16, pp. 5556-5564, 2008.

[10] R. S. Pillai, D. Lorenser, and D. D. Sampson, “Deep-tissue access with confocal fluorescence microendoscopy through hypodermic needles,” *Optics Express,* Vol. 19, pp. 7213-7221, 2011.

[11]. Sumitomo. 2009. http://www.sumitomoelectricusa.com.

[12] M. A. Funovics, R. Weissleder, and U.Mahmood, “Catheter-based in vivo imaging of enzyme activity and gene expression: feasibility study in mice.” *Radiology,* 231(3):659–66.

2004.

[13] J. A. Udovich, N. D. Kirkpatrick, A. Kano, A. Tanbakuchi, U. Utzinger, and A. F. Gmitro, "Spectral background and transmission characteristics of fiber optic imaging bundles." *Appl. Opt.* 47(25):4560–4568, 2008.

[14] M. Oki, H. Saka, C. Kitagawa, C. Sako, S. Tanaka, Y. Kawada, and K. Mori. "Visceral Pleural Perforation in Two Cases of Ultrathin Bronchoscopy," *Chest.* 127(6):2271–2273, 2005.

[15] J. Baillie, "The endoscope," *Gastrointest Endosc*. 65(6):886–93, 2007.

[16] H. Kamiuchi, K. Kuwana, T. Fukuyo, H. Yamashita, T. Chiba, T. Dohi, and K. Masamune "3-D endoscope using a single CCD camera and pneumatic vibration mechanism," *Surg Endosc* , 27(5):1642-7. May 2013.

[17] A.Catanzaro, A. Faulx, G. A. Isenberg, R. C. K. Wong, G. Cooper, M. V. Sivak, and A. Chak, "Prospective evaluation of 4-mm diameter endoscopes for esophagoscopy in sedated and unsedated patients," *American Society for Gastrointestinal Endoscopy,* , San Francisco, California May 20-23, 2002

[18] L. Wang, Y. Shi, Z. Lu, and H. Duan "Miniaturized CMOS Imaging Module with Real-time DSP Technology for Endoscope and Laryngoscope Applications." *Journal of Signal Processing Systems*, 54:7-13, 01/2009

[19] X. Mu, W. Sun, H. Feng, A. Yua, K. W. S. Chen, C. Y. Fu, and M. Olivo, "MEMS micromirror integrated endoscopic probe for optical coherence tomography bio imaging ," *Sensors and Actuators A: Physical*, Volume 168, 202–212 , July 2011.

[20] Y. Xu, J. Singh, C. S. Premachandran, A. Khairyanto, K. W. S Chen, N. Chen, C. J. R Sheppard and M. Olivo, "Design and development of a 3D scanning MEMS OCT probe using a novel SiOB package assembly," *J. Micromech. Microeng*. 18 125005, 2008.

[21] X.J. Mu, G.Y. Zhou, H. Feng, Y. S. Xu, A. B. Yu, C.W. Tan, K.W.S. Chen, J. Xie, F. and S. Chau, "A 3mm endoscopic probe with integrated MEMS micromirror for optical coherence tomography bioimaging", Proc. Eurosensors, September 5-8, 2010, Linz, Austria.

[22] J. J. Bernstein, T. W. Lee, F. J. Rogomentich, M. G. Bancu, K. H. Kim, G. Maguluri, B. E. Bouma, and J. F. DeBoer, "Scanning OCT endoscope with 2-axis magnetic micromirror", Proceedings of SPIE - The International Society for Optical Engineering, 03/2007.

[23] M.F. Wang, Y. Xu, C. S. Prem, K. W. Chen, J. Xie, X. Mu, C. W. Tan, A. Yu, and H. Feng.

"Microfabricated endoscopic probe integrated MEMS micromirror for optical coherence tomography bioimaging". *Conf Proc IEEE Eng Med Biol Soc*, 57-60, 2010.

[24] U. Izhar, A. B. Izhar, S, and Tatic-Lucic, "A multi-axis electrothermal micromirror for a miniaturized OCT system", S*ensors and Actuators A-physical*, vol. 167, no. 2, pp. 152-161, 2011

[25] F. Hu, Y. Tang and Y. Qian, "Design of a MEMS micromirror actuated by electrostatic repulsive force" *J. Light Electron Opt*, 123 387–90, 2012.

[26] W. Jung, D. T. McCormick, J. Zhang, L. Wang, N. C. Tien, and Z. Chen, "Three-dimensional endoscopic optical coherence tomography by use of a two-axis microelectromechanical scanning mirror", Appl. Phys. Lett. 88, 163901 2006.

[27] J. M. Zara, S. Yazdanfar, K. D. Rao, J. A. Izatt, S. W. Smith, "Electrostatic micromachinescanning mirror for optical coherence tomography", *Opt. Lett.* 28, 2003.

[28] W. Piyawattanametha, P. R. Patterson, D. Hah, H. Toshiyoshi and M. C. Wu "Surface- and bulk- micromachined two-dimensional scanner driven by angular vertical comb actuators," *J. Microelectromech. Syst.* 14 1329–38, 2005.

[29] U. Izhar, A. B. Izhar and S. Tatic-Lucic "A multi-axis electrothermal micromirror for miniaturized OCT system," Sensors Actuators A 167 152–61, 2011.

[30] L. Wu and H. Xie, "Electrothermal micromirror with dual-reflective surfaces for circumferential scanning endoscopic imaging," *Journal of Micro/ Nanolithography, MEMS, and MOEMS*. 8(1).01/2009.

[31] A. Jain and H. Xie, "A single-crystal silicon micromirror for large bi-directional 2D scanning applications," *Sensors Actuators A* 130–1 454–60, 2006

[32] X. J. Mua, , G. Y. Zhou, H. H. Feng, Y. S. Xu, A. B. Yu, C. W. Tan, K.W. S. Chen, J. Xie, F. S. Cha, "A 3mm endoscopic probe with integrated MEMS micromirror for optical coherence tomography bioimaging" , *Proc. Eurosensors XXIV,* September 5-8, 2010, Linz, Austria.

[33] X. Mu, W. Sun, H. Feng, A. Yu, K. W. S. Chen, C. Y. Fu, and M. Olivo, "MEMS micromirror integrated endoscopic probe for optical coherence tomography bioimaging", *Sensors Actuators A* ,Volume 168, Pages 202–212, July 2011

[34] T. L. Tan, C. P. Hsu, W. C. Chen and W. Fang "Design and implementation of a torque-enhancement 2-axis magnetostatic SOI optical scanner", *J. Micromech. Microeng.* Volume 20, 025020, 2010

[35] A. D. Yalcinkaya, H. Urey, D. Brown, T. Montague, and R. Sprague "Two-axis electromagnetic microscanner for high resolution displays", *J. Microelectromech. Syst.*15,786–94, 2006.

[36] K. H. Kim, B. H. Park, G. N. Maguluri, T. W. Lee, F. J. Rogomentich, and M. G. Bancu, "Two-axis magnetically-driven MEMS scanning catheter for endoscopic high-speed optical coherence tomography", *Opt Express*, 15(26):18130-40, 2007 Dec 24.

[37] M. G. Nicholas, Z. Lai and M. Bachman, "Magnetically Actuated Micromirror for Endoscopic Applications", BioMed, 32, pp. 61-62,2010.

[38] N. Weber, D. Hertkorn, H. Zappe, and A. Seifert, "Ultra-compact micromirror with polymeric hard magnet for use in endoscopic imaging", Proceedings of the IEEE International Conference on Micro Electro Mechanical Systems (MEMS) , pp 732 – 735,
2011.

[39] J. J. Bernstein, T. W. Lee, F. J. Rogomentich, M. G. Bancu, K. H. Kim, G. Maguluri, B. E. Bouma, and J. F. DeBoer, "Scanning OCT endoscope with 2-axis magnetic micromirror", *Proc. SPIE, Endoscopic Microscopy II*, 64320L (2007).

[40] T. Bakke, A. Vogl, O. Zero, F. Tyholdt, I. R. Johansen, and D. Wang, "A novel ultra-planar, long-stroke and low-voltage piezoelectric micromirror", *J. Micromech. Microeng*. 20, 064010, 2010

[41] J. G. Smits, K. Fujimoto, and V. F. Kleptsyn, "Microelectromechanical flexure PZT actuated optical scanner: static and resonance behavior", *J. Micromech. Microeng*. 15 1285–93, 2005

[42] K. H. Gilchrist, D. E. Dausch, and Sonia Grego, "Electromechanical performance of piezoelectric scanning mirrors for medical endoscopy", *Sens Actuators A Phys*, 1; 178: 193–201. 2012 May

[43] K. H. Gilchris, R. P. McNabb, J. A. Izatt, and S. Grego, "Piezoelectric scanning mirrors for endoscopic optical coherence tomography", *J. Micromech. Microeng.* 19 095012. 2009.

[44] K. H. Gilchrist, D. E. Dausch, and S. Grego, "Electromechanical performance of piezoelectric scanning mirrors for medical endoscopy", *Sens Actuators A Phys.* Volume 178, Pages 193–201, May 2012.

[45] J. Zara, S. Yazdanfar, K. Rao, J. Izatt, and S. Smith, "Electrostatic micromachine scanning mirror for optical coherence tomography" ,*Opt. Lett*, vol. 28, pp. 628–630, Apr. 2003

[46] L. Wu, and H. Xie, “A large vertical displacement electrothermal bimorph microactuator with very small lateral shift,” *Sens. Actuators, A* ,Volumes 145–146, , Pages 371–379, July–August 2008.

[47] J. J. Sun, S. G. Guo, L. Wu, L. Liu, S. W. Choe, B. S. Sorg, and H. K. Xie, “3D In Vivo optical coherence tomography based on a low-voltage, large-scan-range 2D MEMS mirror,” Opt. Express 18(12), 12065–12075 (2010).

[48] F. Filhol, E. Defaÿ, C. Divoux, C. Zinck, M. T. Delaye, “Resonant micro-mirror excited by a thin-film piezoelectric actuator for fast optical beam scanning”, *Sens. Actuators, A*, Volumes 123–124, Pages 483–48923, September 2005.

[49] J. H. Park, J. Akedo, and H. Sato, “High-speed metal-based opticalmicroscanners using stainless-steel substrate and piezoelectric thick films prepared by aerosol deposition method,” Sens. *Actuators A, Phys.*, vol. 135, pp. 86–91, Mar. 2007.

[50] Y. Yasuda, M. Akamatsu, M. Tani, T. Iijima, and H. “Toshiyoshi, Piezoelectric 2Doptical micro scanners with PZT thick films”, *Integr. Ferroelectr*. 76 (2005).

[51] T. Naono, T. Fujii, M. Esashi and S. Tanaka, “A large-scan-angle piezoelectric MEMS optical scanner actuated by a Nb-doped PZT thin film”, *J.Micromech.Microeng*. 24 015010, 2014.

[52] N. Weber, H. Zappe and A. Seifert, “An all-nickel magnetostatic MEMS scanner”, *J.Micromech.Microeng.* 22 125008, 2012.

[53] P. Niederer, J. Hafliger, P. Blessing, Y. Lehareinger, D. Doswald, and N. Felber, “Image quality of endoscopes”, *Proc. SPIE Biomonitoring and Endoscopy Technologies*. 4158:1-10. (2001)

[54] M. T. Myaing, D. J. MacDonald, and X. Li, “Fiber-optic scanning two-photon fluorescence endoscope”, *Optics Letters*, Vol. 31, pp. 1076-1078, 2006.

[55] W. Liang, K. Murari, Y. Zhang, Y. Chen, M. J. Li, and X. Li, “Increased illumination uniformity and reduced photodamage offered by the Lissajous scanning in fiber-optic two-photon endomicroscopy”, *J. Biomed. Opt*, 17(2):021108, 2012.

[56] T. Matsunaga, R. Hino, W. Makishi, and M. Esashi, “Electromagnetically driven ulutra-miniature single fiber scanner for high-resolution endoscopy fabricated on cylindrical substrates using mems process”, *Micro Electro Mechanical Systems (MEMS), 2010 IEEE 23rd*

International Conference on, 999 – 1002, 24-28 Jan. 2010.

[57] T. Chen, N. Zhang, T. Huo, C. Wang, J. Zheng, T. Zhou, and P. Xue, "Tiny endoscopic optical coherence tomography probe driven by a miniaturized hollow ultrasonic motor", *J. Biomed. Opt.* 18(8), 086011 (Aug 16, 2013).

[58] J. Knittela, L. Schniedera, G. Buessa, B. Messerschmidtb, and T. Possnerb, "Endoscope-compatible confocal microscope using a gradient index-lens system", *Optics Communications*, Volume 188, Pages 267–273, 15 February 2001.

[59] C.-S. Rim, P. Kim, and S.-H. Yun, "Design of an Endoscope Objective Lens with a High Numerical Aperture and a Minimally-Invasive Outer Diameter", Journal of the Korean Physical Society, Vol. 51, pp. 5264, July 2007.

[60] C. M. Lee, C. J. Engelbrecht, T. D. Soper, F. Helmchen,and E. J. Seibel, "Scanning fiber endoscopy with highly flexible, 1-mm catheterscopes for wide-field, full-color imaging", *J Biophotonics*, 3(5-6): 385–407, 2010 Jun.

[61] E. J. Seibel, Q. Y. J. Smithwick, C. M. Brown, P. G. Reinhall, "Single-fiber flexible endoscope: general design for small size, high resolution, and wide field of view", *Proc. SPIE Biomonitoring and Endoscopy Technologies*, 4158, 29 (January 19, 2001)

[62] Y. Wu, Y. Leng, J. Xi, and X. Li, "Scanning all-fiber-optic endomicroscopy system for 3D nonlinear optical imaging of biological tissues", *Opt Express*. 11; 17(10): 7907–7915. 2009 May

[63] E. J. Seibel, M. Fauver, J. C.-Bosworth, Q. Y. J. Smithwick, and C. M. Brown. "Microfabricated optical fiber with a microlens that produces large field-of-view video-rate optical beam scanning for microendoscopy applications", *Optical Fibers and Sensors for Medical Applications III*, pp. 46-55, 1 July 2003.

[64] R. L. D. Miranda, C. Zamponi, and E. Quandt, "Rotational UV lithography device for cylindrical substrate exp

osure", *Rev Sci Instrum*., 80(1):015103. 2009 Jan.

[65] P. H. Tran, D. S. Mukai, M. Brenner, and Z. Chen, "In vivo endoscopic optical coherence tomography by use of a rotational microelectromechanical system probe", *Opt Lett.*, 1;29(11):1236-8, 2004 Jun.

[66] L. Giniunas, R. Laser, R. Juskaitis, S. V. Shatalin, "Scanning fibre-optic microscope", *Electron.Lett.*, 27 (9) 724–726,1991.

[67] N. Weber, T. Meinert, H. Zappe, and A. Seifert, “TUNABLE MEMS FIBER SCANNER FOR CONFOCAL MICROSCOPY”, *MEMS 2014 San Francisco, CA, USA*, pp 881-884, January 26 - 30, 2014.

[68] D. Yelin, B. E. Bouma, S. H. Yun, and G. J. Tearney, “Double-clad fiber for endoscopy”, *Opt. Lett.* 29 (20), 2408–2410, 2004.

[69] D. R. Rivera, C. M. Brown, D. G. Ouzounov, I. Pavlova, D. Kobat, W. W. Webb, and C. Xu, “Compact and flexible raster scanning multiphoton endoscope capable of imaging unstained tissue”, *Proceedings of the National Academy of Sciences*.,108(43):17598-603. 2011

[70] Y. Choi, C. Yoon, M. Kim, T. D. Yang, C. Fang-Yen, R. R. Dasari, K. J. Lee, and W. Choi, “Scanner-Free and Wide-Field Endoscopic Imaging by Using a Single Multimode Optical Fiber”, *Phys. Rev. Lett*.,109, 203901, 2012.

[71] C. D. Saunter, S. Semprini, C. Buckley, J. Mullins, and J. M. Girkin, “Micro-endoscope for in vivo widefield high spatial resolution fluorescent imaging”, *Biomed. Opt.Express*, 3 (6), 1274–1278, 2012.

[72] E. J. Seibel, “1-mm catheterscope”, *Proc. SPIE, Optical Fibers and Sensors for Medical Diagnostics and Treatment Applications VIII*, 685207, 7 February 2008.

[73] O. Ferhanoglu, M. Yildirim, K. Subramanian, and A. Ben-Yakar, “A 5-mm piezo-scanning fiber device for high speed ultrafast laser microsurgery”, *Biomed Opt Express.*, 5(7): 2023–2036, 2014.

[74] L. Huo, J. Xi, Y. Wu, and X. Li, “Forward-viewing resonant fiber-optic scanning endoscope of appropriate scanning speed for 3D OCT imaging”, *Opt Express.* , 18(14): 14375–14384, 2010.

[75] D. Huang, E. A. Swanson, C. P. Lin, J. S. Schuman, W. G. Stinson, W. Chang, M. R. Hee, T. Flotte, K. Gregory, and C. A. Puliafito, “Optical coherence tomography” *Science*, 254, p.1178, 1991.

[76] E. A. Swanson, J. A. Izatt, M. R. Hee, D. Huang, C. P. Lin, J. S. Schuman, C. A. Puliafito, and J. G. Fujimoto, “In vivo retinal imaging by optical coherence tomography”, *Opt. Lett.*, 18:1864, 1993.

[77] W. Drexler, U. Morgner, F. X. Kärtner, C. Pitris, S. A. Boppart, X. D. Li, E. P. Ippen, J. G. Fujimoto, “In vivo ultrahigh-resolution optical coherence tomography”, *Opt. Lett.*, 24, p. 122,

1999.

[78] A. F. Fercher, C. K. Hitzenberger, G. Kamp, and S. Y. EI-Zaiat, “Measurement of intraocular distances by backscattering spectral interferometry”, *Opt. Commun.*, 117, p. 43, 1995.

[79] G. Häusler, M. W. Lindner, “Coherence radar and spectral radar-new tools for dermatological diagnosis”, *J. Biomed. Opt.*, 3, p. 21, 1998.

[80] S. Yun, G. J. Tearney, B. E. Bouma, B. Park, and J. F. deBoer “High-speedspectral-domain optical coherence tomography at 1.3 μm wavelength”, *Opt. Express.*, 11, p. 3598, 2003.

[81] T. S. Kirtane, and M. S. Wagh, “Endoscopic Optical Coherence Tomography (OCT)”, Advances *in Gastrointestinal Imaging*, Volume 2014, 376367, 7 pages, 2014.

[82] X. D. Li, S. A. Boppart, J. V. Dam, H. Mashimo, M. Mutinga, W. Drexler, M. Klein, C. Pitris, M. L. Krinsky, M.E. Brezinski, and J. G. Fujimoto, “Optical coherence tomography”, *advanced technology for the endoscopic imaging of Barrett's esophagus. Endoscopy.*, 32(12):921-30, 2000.

[83] T. Xie, H. Xie, G. K. Fedder, and Y. Pan, “Endoscopic optical coherence tomography with new MEMS mirror”, *Electronics Letters.*, Volume:39, 1535 – 1536, 2003.

[84] L. Liu, L. Wu, J. Sun, E. Lin, and H. Xie, “Miniature endoscopic optical coherence tomography probe employing a two-axis microelectromechanical scanning mirror with through-silicon vias”, *J. Biomed. Opt.*,16(2), 026006, 2011.

[85] K. H. Gilchrist, R. P. McNabb, J. A. Izatt, and S. Grego, “Piezoelectric scanning mirrors for endoscopic optical coherence tomography”. *Journal of Micromechanics and Microengineering.*, 19 (9), 095012, 2009.

[86] A. R. Rouse, A. Kano, J. A. Udovich, S. M. Kroto, and A. F. “GmitroDesign and demonstration of a miniature catheter for a confocal microendoscope” *Applied Optics*, Vol. 43, pp. 5763-5771, 2004.

[87] J. Knittel, L. Schnieder, G. Buess, B. Messerschmidt, and T. Possner, “Endoscope-compatible confocal microscope using a gradient index-lens system”, *Opt. Commun.*, 188, 267–273, 2001.

[88] K. B. Sung, C. Liang, M. Descour, T. Collier, M. Follen, and R. Richards-Kortum, “Fiber-optic confocal reflectance microscope with miniature objective for in vivo imaging of human Biomedical Engineering, *IEEE Transactions*., Vol.49, pp. 1168-1172, 2002.

[90] J. W. Judy and R. S. Muller, “Magnetically actuated, addressable microstructures J. Microelectromech. Syst”, 6 249–56,1997.

[91] C. Siewert, F. Loffler, “Photolithographic structuring of a thin metal film coil on a Zerodur cylinder”, Surface & Coatings Technology., 200, 1061 – 1064, 2005.

[92] Y. Matsumoto, M. Setomoto, D. Noda, and T. Hattori, “Cylindrical coils created with 3D X-ray lithography and metallization”, *Microsyst. Technol.*, 14, pp. 1373–1379, 2008.

[93] S. Desai, A. N. Netravali, and M. O. Thompson, “Carbon fibers as a novel material for high-performance microelectromechanical systems (MEMS)”, J. Micromech. Microeng. 16 (2006) 1403

[94] W. Xu, S. Choi, M. G. Allen, "Hairlike carbon-fiber-based solar cell," 23rd IEEE International Conference on Micro Electro Mechanical Systems (MEMS 2010), p 1187 - 1190, Jan. 2010.

[95] B. O'Connor, K. P. Pipe, and M. Shtein, "Fiber based organic photovoltaic devices", Appl. Phys. Lett. 92, 193306 (2008).

[96] Toivola, M.; Ferenets, M.; Lund, P.; Harlin, A. Photovoltaic fiber. Thin Solid Films 2009, 517, 2799–2802.

[97] Web [http://www.beanspj.org/index.html]

[98] M. Sasaki, T. Ando, S. Nogawa, and K. Hane:Jpn. “Direct photolithography on optical fiber end”, J. Appl. Phys. 41 (2002) 4350

[99] D. C. Abeysinghe, S. Dasgupta, H. E. Jackson, and J. T. Boyd, “Novel MEMS pressure and temperature sensors fabricated on optical fibers,” J. Micromech. Microeng. 12(3), 229–235 (2002)

[100] S. Uchiyama1, M. Hayase, H. Takagi, T. Itoh, and Y. Zhang “Spray Coating Deposition of Thin Resist Film on Fiber Substrates” Jpn. J. Appl. Phys. 51 116502

[101] K.S. Lee, R.H. Hee, P. Prabhakaran, D.Y. Yang, L.T. Woo, S.H. Park, “TWO-PHOTON STEREOLITHOGRAPHY”, J. Nonlinear Opt. Phys. Mater. (16) (2007) 59–73

[102] S.H. Park, D.Y. Yang, and K.S. Lee, "Two-photon stereolithography for realizing ultraprecise three-dimensional nano/microdevices", Laser Photonics Rev. (3 1-) (2009) 1–11.

[103] J. W. Perry, B. H. Cumpston, S. P. Ananthavel, S. Barlow, D. L. Dyer, J. E. Ehrlich, L. L. Erskine, A. A. Heikal, S. M. Kuebler, I.-Y. S. Lee, D. McCord-Maughon, J. Qin, H. Röckel, M.

Rumi, X.-L. Wu, and S. R. Marder, “Two-photon polymerization initiators for three-dimensional optical data storage and microfabrication,” Nature 398(6722), 51–54 (1999)

[104] C. Sun, N. Fang, D.M. Wu, and X. Zhang, “Projection micro-stereolithography using digital micro-mirror dynamic mask” Sens. Actuators A 121 (2005) 113–120.

[105] Vijay K. Varadan, Xiaoning Jiang, V.V. Varadan, Microstereolithography and Other Fabrication techniques for 3D MEMS, Wiley, 2001.

[106] D. Lee, T. Miyoshi, Y. Takaya, T. Ha, “3D microfabrication of photosensitive resin reinforced with ceramic nanoparticles using LCD microstereolithography” J. Laser Micro/Nanoeng. 1 (2) (2006) 142–148.